DEVELOPMENT OF NITROGEN-15- AND CARBON-13-LABELED BIOCHEMICAL PROBES FOR HYPERPOLARIZED METABOLIC IMAGING

APPROVED BY SUPERVISORY COMMITTEE

A.Dean Sherry, Ph.D.

Craig Malloy, M.D.

Ralph DeBerardinis, M.D.,Ph.D.

Zoltan Kovacs, Ph.D.

Leonidas Bleris, Ph.D.

Jae Mo Park, Ph.D.

With love and gratitude

To Jiyong and Chloe

DEVELOPMENT OF NITROGEN-15- AND CARBON-13-LABELED BIOCHEMICAL PROBES FOR HYPERPOLARIZED METABOLIC IMAGING

by

EUL HYUN SUH

DISSERTATION

Presented to the Faculty of the Graduate School of Biomedical Sciences

The University of Texas Southwestern Medical Center at Dallas

In Partial Fulfillment of the Requirements

For the Degree of

DOCTOR OF PHILOSOPHY

The University of Texas Southwestern Medical Center at Dallas

Dallas, Texas

May, 2019

ACKNOWLEDGEMENTS

Most of all, I thank God for all the grace and gift he has given me throughout my life. My dissertation would not have been possible without the support and guidance of my supervisor, Prof. A. Dean Sherry. As my mentor and teacher, he has encouraged me with grateful mentorship to accomplish this dissertation research. I would like to express my deepest appreciation to my committee, Dr. Craig Malloy, Dr. Ralph DeBerardinis, Dr. Zoltan Kovacs, Dr. Jae Mo Park, and Dr. Leonidas Bleris. Each of the members of the dissertation committee has provided me professional guidance and insightful comments. Particularly persuading the project with Dr. Zoltan Kovacs provided me numerous discussions on how everything works in DNP and in chemistry. Dr. Jae Mo Park offered me a good opportunity to expand my knowledge of hyperpolarized NMR imaging as well as scientific skills.

I am thankful to Prof. Mankil Jung at Yonsei University for inspiring me on the path to a doctorate. Thanks should also go to Dr. Jeffery Kelly at Scripps Institute that I was able to pursue an academic career based on his guide. I am grateful to all of those with whom I have had the pleasure to work during this and other related projects. I would like to extend my sincere thanks to Edward Hackett, Dr. R. Max Wynn, Dr. David T. Chuang, Dr. Bo Zhang, and Dr.Weibo Luo who performed experiments in collaboration with me regarding branched chain amino acid metabolism. Also, I would like to thank the laboratory of Dr. Ralph Deberardinis with the helping of Bookyung Ko for glyoxylate metabolism study of the cells. I was able to perform the glyoxylate metabolism study on Yeast thanks to the hospitality of Dr. Benjamin.Tu with the helping of Jun Chen. Thanks should also go to Dr. Shawn Burgess for access to essential instrumentation and Dr. Stanislaw Deja for helping me a hyperpolarization experiments. I wish to thank Dr. Ian Corbin who taught me a great deal about sampling of brain tissue and

gave many discussions for cancer model. I am also grateful to Dr. Alexander Funk, Dr. Charlie Khemtong, and Dr. Lloyd Lumata for advice and training for NMR and hyperpolarized experiment. Many thanks to chemistry lab members who also helped me greatly including Christian Preihs, Gaurav Sharma, Xiaoiging Wang, Nesmine Maptue, Xiaodong Wen, and Min Hee Lee. I am very grateful to the laboratory members, James Ratnakar, Quyen Do, Sara Chirayil, and Jaspal Singh who have been great colleagues and shared the tons of moments that make me refreshed. Gratefully recognize funding from the National Institutes of Health (R37 HL034557, S10 OD018468, R00 CA168746, R01 DK62306) and a portion of research also supported by National Center for *in vivo* Metabolism (P41 EB015908) at Advanced Research Imaging Center at UT southwestern Medical Center without which, this research would not be possible.

Finally, nobody has ever been more important to me in the pursuit of this journey than the members of my family. I would like to thank my parents and sister, whose love and prays are with me in whatever I achieve. Most importantly, I wish to thank my loving and supportive husband, Jiyong, and my daughter, Chloe, who provide unending inspiration. I would not have made it this far without them.

February 2019

DEVELOPMENT OF NITROGEN-15- AND CARBON-13-LABELED BIOCHEMICAL PROBES FOR HYPERPOLARIZED METABOLIC IMAGING

Publication No._____

Eul Hyun Suh, Ph.D.

The University of Texas Southwestern Medical Center at Dallas, 2019

Supervising Professor: A. Dean Sherry, Ph.D.

^{13}C and ^{15}N dynamic nuclear polarization coupled with nuclear magnetic resonance study provides an opportunity to non-invasively monitor metabolic fluxes *in vivo* using appropriately designed ^{13}C or ^{15}N enriched metabolic probes. However, hyperpolarized spin states have a short lifetime because the hyperpolarized magnetization decays by T_1 relaxation. This restricts the biological applications of hyperpolarized probes. Therefore, the goal of this dissertation work is to develop ^{13}C and ^{15}N enriched probes with long T_1 values that quickly enter cells and actively metabolize or act as reporters of important biological metal ions involved in metabolism. The first project focuses on cell permeable ^{15}N labeled hyperpolarized probes designed to report zinc

levels, which play a crucial role in the onset and progression of prostate cancer. Deuterated ^{15}N-tris(pyridylmethyl)amine designed and synthesized for this purpose was found to have extremely long T_1 values and an altered ^{15}N chemical shift upon Zn^{2+} binding. Its applicability for zinc mapping was demonstrated in hyperpolarized ^{15}N MRI experiments in phantoms. The second project was to demonstrate the feasibility of using hyperpolarized [1-^{13}C]ketoisocaproic acid as an imaging agent to detect altered branched-chain amino acid metabolism in glioma. This probe was successfully used to monitor both branched-chain aminotransferase and alpha-keto acid dehydrogenase activity in glioma by hyperpolarized ^{13}C imaging *in vivo.* Both ^{13}C-ketoisocaproic acid *in vivo* imaging and ^{13}C-leucine infusion study provided strong evidence for increased catabolism of ketoisocaproic acid in tumor compared to the contralateral normal appearing brain tissue. The third project involved the design and synthesis of ^{13}C labeled glyoxylate in an attempt to image the glyoxylate shunt pathways. [1-^{13}C]Glyoxylate hydrate was successfully synthesized and was evaluated as a metabolic probe for the glyoxylate cycle in cells. However, the incorporation of [1-^{13}C]glyoxylate *via* the glyoxylate cycle was not observed in the mouse embryonic fibroblasts and yeast cells. This is likely due to the high chemical reactivity of glyoxylate toward free amino groups of proteins. In summary, in these projects, ^{15}N and ^{13}C labeled hyperpolarized probes have been investigated for noninvasive monitoring of physiochemical sensing and metabolic processes, which could provide a key to detect abnormality of cancer metabolism.

TABLE OF CONTENTS

PRIOR PUBLICATIONS & PRESENTATIONS

PUBLICATIONS:

1. **Suh, E. H.**; Hackett, E.P.; Wynn R. M.; Chuang D. T.; Zhang B.; Luo W.; Sherry, A. D; Park, J.M.; "In vivo assessment of increased oxidation of branched-chain amino acids in glioblastoma." *Scientific reports* 9, 340 (2019)

2. Singh, J.; **Suh, E. H.**; Sharma, G.; Khemtong, C.; Sherry, A. D.; Kovacs, Z.; "Probing carbohydrate metabolism using hyperpolarized (13) C-labeled molecules". *NMR in biomedicine* (2018), doi: 10.1002/nbm.4018

3. Pérez-Malo M.; Szabó G.; Eppard E.; Vagner A.; Brücher E.; Tóth I.; Maiocchi A.; **Suh, E.H.**; Kovács Z.; Baranyai Z.; Rösch F.; "Improved Efficacy of Synthesizing *M(III)-Labeled DOTA Complexes in Binary Mixtures of Water and Organic Solvents. A Combined Radio- and Physicochemical Study." *Inorganic chemistry* 57, 6107-6117 (2018).

4. Sirusi, A.A., **Suh, E.H.**, Kovacs, Z. & Merritt, M.E. "The effect of Ho(3+) doping on (13)C dynamic nuclear polarization at 5 T." *Physical chemistry chemical physics : PCCP 20,* 728-731 (2018).

PRESENTATIONS AND POSTERS:

1. **Suh, E. H.**; Hackett, E.P.; Wynn R. M.; Chuang D. T.; Zhang B.; Luo W.; Sherry, A. D; Park, J.M. "In vivo assessment of increased oxidation of branched-chain amino acids in glioblastoma" The World Molecular Imaging Congress (**WMIC**) **2018**, September 12-15, Seattle, WA
2. **Suh, E.H**.; Ou,W.; Corbin, IR.; Sherry, A. D.; Park, J.M. "Imaging branched-chain amino acid metabolism in glioma using hyperpolarized [1-^{13}C] α-ketoisocaproate" Proc. Intl. Soc. Mag. Reson. Med. 25 (**ISRMR**) **2017** # 3604
3. **Suh, E. H**.; Lumata, L.; Sherry, A. D.; Kovács, Z. "Hyperpolarized ^{15}N Tris(2-pyridylmethyl)amine (TPA) derivetives as Hyperpolarized ^{15}N Magnetic Resonance Probe for Zn^{2+}" The international chemical congress of pacific basin societies (**Pacifichem**) **2015**, Honolulu, HI
4. **Suh, E. H**.; Lumata, L.; Sherry, A. D.; Kovács, Z. "Hyperpolarized ^{15}N Tris(2-pyridylmethyl)amin(TPA) as ^{15}N MR Zn^{2+} sensor" 26th International Council on Magnetic Resonance in Biological Systems (**ICMRBS**) **2014**, Dallas, TX

LIST OF FIGURES

LIST OF TABLES

LIST OF SCHEMES

LIST OF ABBREVIATIONS

[1-^{13}C]KIC	[1-^{13}C] α-ketoisocaproic acid
[^{15}N]BP	^{15}N-Benzyl-1-(pyridine-2-yl)-N-(pyridine-2ylmethyl)methanamine
[^{15}N]TPA	^{15}N-tris(2-pyridylmethyl)amine
[^{15}N]TPA-d_6	^{15}N labeled tris(2-pyridylmethyl-$_{d2}$)amine
α-KG	α-ketoglutarate
ALT	Alanine Transaminase
BBB	Blood-Brain Barrier
BCAA	Branched Chain Amino Acid
BCAT	Branched Chain Amino Acid Transferase
BCKDH	Branched Bhain α-ketoacid Dehydrogenase Comple
BDPA	α,γ-bisdiphenylene-β-phenylallyl
CA	Carbonic Anhydrase
CAC	Citric Acid Cycle
CAT	Carnitine AcetylTransferase
$CDCl_3$	Deuterated cholroform
CLYBL	Citrate Lyase Subunit Beta-Like Protein
CS	Citric Synthase
CSA	Chemical Shift Anisotropy
CSI	Chemical Ahift Imaging
d-DNP	Dissolution Dynamic Nuclear Polarization
DCA	Dihlorocetic acid
DHAP	Dihyhroxyacetone phosphate
DMEM	Dulbecco's Modified Eagle Medium
DMSO	Dimethyl Sulfoxide
DNP	Dynamic Nuclear Polarization
DTT	Dithiothreitol
Dy^{3+}	Dysprosium
EDS	Electron Dipolar System
EDTA	Ethylene Diaminetetraacetic Acid
EGFR	Epidermal growth factor receptor
EPR	Electron Paramagnetic Resonance
ESR	Electron Spin Resonance
ESSI	Electron Spin-Spin Interaction
EZS	Electron Zeeman system
FA	Flip Angle

FBS	Fetal Bovine Serum
FH	Fumarate Hydratase
G3P	Glycerylaldehyde-3-phosphate
GBM	Glioblastomas
GdDO3A	Gadolinium (III) gadolinium 1,4,7-triscarboxymethyl-1,4,7,10-tetraazacyclododecane
GLDH	Glutamate dehydrogenase
H&E	Staining hematoxylin and eosin (H&E) stain
HAS	Human Serum Albumin
HEPES	4-(2-hydroxyethyl)-1-piperazineethanesulfonic acid
Ho^{3+}	Holmium ion
HSA	Human Serum Albumin
ICL	Isocitrate lyase
IDH	Isocitrate dehydrogenase
IPA	Iophenoxic acid
LAT1	L–amino acid transporter-1
LDH	Lactate dehydrogenase
MCTs	monocarboxylate transporters
MDH	Malate dehydrogenase
MEF	Embryo fibroblasts
MRI	Magnetic Resonance Imaging
MRS	Magnetic Resonance Spectroscopy
MS	Malate synthase
NAB	Normal Appearing Brain
NAD/NADH	Nicotinamide adenine dinucleotide
NaF	Sodium fluoride
NMR	Nuclear Magnetic Resonance
NOE	Nuclear Overhauser Effect
NZS	Nuclear Zeeman System
OAA	Oxaloacetate
OGDC	Oxoglutarate dehydrogenase complex
OX063	Tris (8-carboxyl-2,2,6,6-tetra[2-(1-hydroxymethyl)]-benzo(1,2-d:4,5-d')bis(1,3)dithiole-4-yl) methyl sodium salt
PBS	Phosphate Buffered Saline
PHIP	Parahydrogen Induced Polarization
PC	Pyruvate carboxylate
PCA	Perchloric acid
PCa	Prostate cancer (PCa)

PCA3	Prostate cancer antigen 3
PDH	Pyruvate dehydrogenase complex
PDH-KO MEF	Pyruvate Dehydrogenase E1 Alpha 1 Subunit knockout MEF
PEP	Phosphoenolpyruvate
PET	Positron Emission Tomography
Phi	Prostate health index
PSA	Prostate-specific antigen
RF	Radio Frequency
S-CPP	(S)-2-Chloro-3-phenylpropanoic acid sodium salt
SCS	Succinyl Coenzyme A synthetase
SNR	Signal to Noise Ratio
SQR	Succinate dehydrogenase
Tb^{3+}	Terbium ion
TEMPO	(2,2,6,6-Tetramethylpiperidin-1-yl)oxyl
TEMPOL	4-hydroxy-2,2,6,6-tetramethylpiperidin-1-oxyl
TFA	Trifluoroacetate
TMSCl	Trimethylchlorosilane
TOTAPOL	1-(TEMPO-4-oxy)-3-(TEMPO-4-amino)propan-2-ol
TRE	TRE,1-o-α-D-glucopyranosyl-α-D-glucopyranoside
Tri-Sil HTP	Trimethylsilylation
ZnAF-2F	6-{2-[Bis(2-pyridylmethyl)amino]ethylamino}-2′,7′-difluorofluorescein
$ZnSO_4$	Zinc sulfat

Chapter 1

BACKGROUND

1.1 Nuclear magnetic resonance (NMR) spectroscopy

The phenomenon of nuclear magnetic resonance (NMR) was demonstrated for the first time in 1945 by Purcell and Bloch[1,2] who were awarded the Nobel Prize in physics (1952). NMR spectroscopy can provide chemical structure information *via* chemical shifts through the magnetic property of the nuclei. NMR active nuclei with a spin quantum number of I ≥ ½ (e.g., ^{1}H, ^{13}C, or ^{15}N) absorb radiofrequency energy in a B_0 external magnetic field at a specific frequency called the Larmor frequency. This frequency is dependent on the strength of the B_0 magnetic field, type of nuclei, and its chemical environment. Because of the shielding by electrons in chemical bonds, the same type of nucleus (e.g. ^{13}C) in different chemical environment absorbs at slightly different frequencies to produce a wide chemical shift range. In addition, the nuclear spins interact with adjacent nuclei through covalent bonds *via* scalar couplings or through space by dipolar coupling. Other NMR parameters such as longitudinal relaxation time (T_1) and transverse relaxation time (T_2) also provide insights into molecular structure and dynamics.

1.1.1 Nuclear spin interaction with magnetic field

According to classical physics, magnetic moments of nuclei are random in the absence of an external magnetic field. However, in the presence of a magnetic field (B_0), nuclear spins align along (B_0) (Figure 1.1.a) precess around B_0 at a specific Larmor frequency. The potential energy

E of a magnetic moment can be described in Equation 1.1.[3]

$$\mathrm{E} = -\mu \cdot B = -\mu_z \cdot B_0 \tag{1.1}$$

In quantum mechanical terms, the nuclear spin can be described by quantized angular momentum and the magnetic moment along the longitudinal Z axis (μ_z) is given by the Equation 1.2

$$\mu_z = \gamma \left(\frac{h}{2\pi}\right) I \tag{1.2}$$

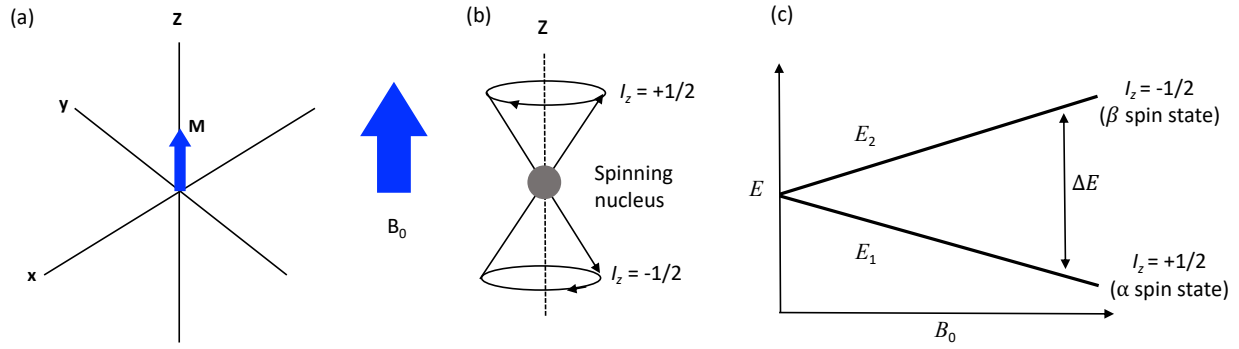

Figure 1.1 (a) Magnetization (M) *via* applied B_0 field along Z direction (b) Interaction between a spinning nucleus and external field, and (c) spin-up (α) and spin-down (β) are different energy levels linearly dependent on external magnetic field

The magnitude of magnetic momentum μ is proportional to the gyromagnetic ratio γ and spin quantum number I, which is determined by the number of protons and neutrons that make up the nucleus. This spin quantum number defines the overall magnetic property of the nucleus. Nuclei such as carbon (^{12}C) and oxygen (^{16}O) have spin quantum number $\mathrm{I} = 0$ and are not detectable by NMR. Nuclei with spin quantum number $\mathrm{I} \neq 0$ such as ^{1}H, ^{13}C, ^{15}N, ^{19}F, ^{29}Si, ^{31}P, ^{2}H and ^{23}Na are NMR active.[4] A list of common NMR active nuclei and gyromagnetic ratios is provided in Table 1.1.

Nucleus	n (spin)	Natural abundance (%)	$\gamma_n/2\pi$ (MHz/T)	Chemical shift ($\Delta\delta$)
^{1}H	1/2	99.98	42.677	13
^{2}H	1	0.02	6.536	13
^{13}C	1/2	1.11	10.708	200
^{15}N	1/2	0.37	-4.136	900
^{89}Y	1/2	100	-2.806	1300
^{19}F	1/2	100.00	40.052	700
^{23}Na	3/2	100.00	11.262	72
^{31}P	1/2	100.00	17.235	430
^{29}Si	1/2	4.68	-8.465	519

Table 1.1 Gyromagnetic ratios of some NMR active nuclei

From quantum mechanics, spin angular momentum of the spin ½ nuclei is quantized to $I_z = \pm 1/2$, and the energy difference of the two energy state is shown in Equation 1.3.

$$\Delta E = \gamma \hbar B_0 = h\left(\frac{\gamma}{2\pi}\right) B_0 \tag{1.3}$$

where, $\hbar$ is Plank's constant (= h /2π, 6.63 x 10^{-27}erg sec). Under the external magnetic field (B_0) along the Z-axis, the nuclear spins are aligned in the +Z/-Z direction in two different energy levels. The parallel (+Z) or anti-parallel (-Z) to the applied magnetic field are often referred to as the α and β states, respectively (Figure 1.1.b). The energy difference between two spins states are called the nuclear Zeeman effect, which was initially described by Pieter Zeeman in 1896, who had observed optical spectral splitting by a magnetic field. The population of spin ratio in the presence of B_0 can be calculated using by Boltzmann's law (Equation 1.4)[4].

$$\frac{n_\alpha}{n_\beta} = e^{\frac{\Delta E}{kT}} = e^{\frac{h\upsilon}{\mathrm{kT}}} \tag{1.4}$$

where, n_α is the number of spin in α states, n_β is the number of spins in the β states, k is Boltzmann constant, T is the absolute temperature in K, and ΔE is the energy difference between the α and β state. The ΔE determines the intensity of NMR which is directly proportional to the B_0 and gyromagnetic ratio (γ) (Equation 1.3). Therefore, larger γ nuclei such as ^{1}H or ^{13}C have stronger NMR signal compared to low gyromagnetic ratio nuclei such as ^{15}N (Figure 1.2)[4]

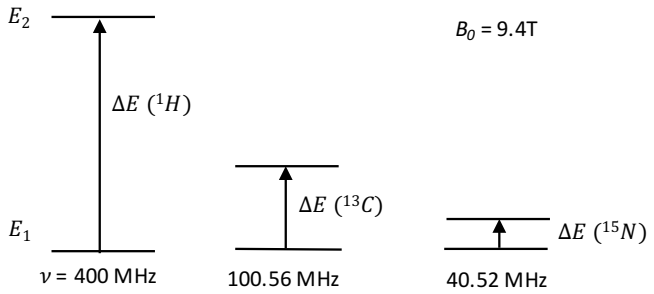

Figure 1.2 The energy difference between spin states for ^{1}H, ^{13}C, and ^{15}N under B_0 = 9.4T, which determines the intensity of the absorption

1.1.2 Magnetization

Resonance is a phenomenon of interconversion of nuclei spin states from α to β and vice versa when a second weaker filed (B_1) is applied perpendicular to B_0 that matches the Larmor frequency of the precessing nuclei (Equation 1.5).

$$\omega_0 = \gamma B_0 \text{ (rad s}^{-1}\text{)} \quad (1.5)$$

This weak applied B_1 field is generated by use of radio frequency (rf) pulse transmitted through a coil that surrounds the sample perpendicular to B_0. Once the rf pulse of angle θ is applied to nuclear spins, the M_z magnetization vector tilts toward the x-y plane. M_{xy} magnetization and longitudinal magnetization (M_z) are equal to $M_0 \sin\theta$ and $M_0 \cos\theta$, respectively (Figure 1.3). The

flip angle (θ) is determined by the duration of the pulse and applied field strength, B_1, which can be described by the Equation $\theta = 2\pi\gamma\tau B_1$. For instance, when a rf pulse is applied with 90° flip angle, M_0 magnetization spins will be flipped entirely into M_{xy} plane. After the rf pulse is turned off, the magnetization, M_{xy} returns to its equilibrium state along the z- direction (M_Z) followed by relaxation processes[3].

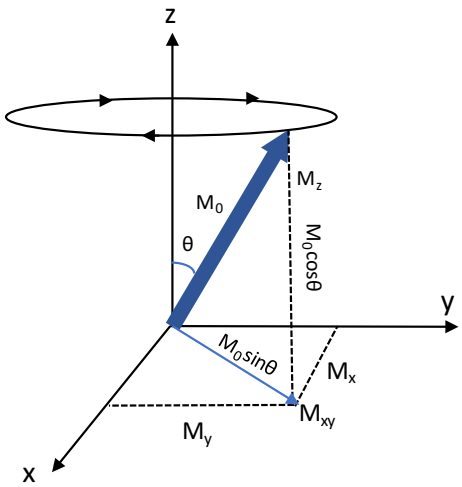

Figure 1.3 Net Magnetization Vector

1.1.3 Relaxation

1.1.3.1 Longitudinal relaxation

The longitudinal component of the magnetization is described by Equation 1.6 and the solution of it is the Equation 1.7 (after 90° excitation, $M_z(0) = 0$). Longitudinal relaxation is the exponential recovery of longitudinal magnetization along the z-axis. This recovery rate is defined by the time constant T_1 that describes the time required for M_z to recover 63% of spin

magnetization (Figure 1.4).[5]

$$\frac{dM_Z}{dt} = -\frac{M_Z - M_0}{T_1} \tag{1.6}$$

$$M_z(t) = M_0(1 - e^{-t/T_1}) \tag{1.7}$$

T_1 relaxation relies on energy exchange between the nuclear spin system and its lattice (environment). The major source of longitudinal relaxation in liquid state is the isotropic tumbling of molecules in solution which generates fluctuating local magnetic fields. In general, small molecules and macromolecules have longer T_1 than medium size molecules since their molecular rotation frequency are most likely in similar range as the Larmor frequency. It is also predominantly affected by dipole-dipole interaction of heteronuclear or homonuclear pairs of nuclear spins. This dipolar relaxation transfers energy from one nucleus to another adjacently coupled nucleus, and the relaxation rate depends on the number of attached nuclei and bond length. For example, T_1 values of ^{13}C are affected by the number of attached protons. In general, non-proton bearing carbon have longer T_1 and follows the order $^{13}C > {}^{13}CH > {}^{13}CH_2 > {}^{13}CH_3$.

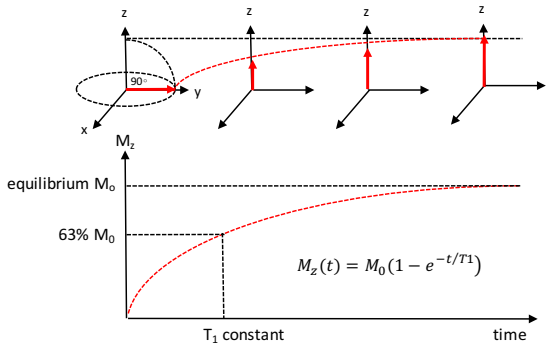

Figure 1.4 Longitudinal relaxation (T_1) process

1.1.3.2 Transverse relaxation

Transverse relaxation is the exponential signal decay or dephasing resulting from temporary and random spin-spin interaction in transverse plane because of a discrepancy among Larmor frequency of the spins in an asymmetric statistical clustering of spins. This will cause slightly different angular velocity in the transverse plane among the precessing individual spins and loss of their phase coherency over time. This spin-spin relaxation is the transverse component of magnetization (M_{xy}) progressive decay or dephasing, which is considered to follow first order kinetics. The transverse component of the magnetization behaves according to Equation 1.8 and the solution is given by Equation 1.9 (after 90° excitation, $M_{xy}(0) = M_0$).

$$\frac{dM_{xy}}{dt} = -\frac{M_{xy}}{T_2} \tag{1.8}$$

$$M_{xy}(t) = M_0 e^{-t/T_2} \tag{1.9}$$

This decay rate is defined by the time constant T_2 that is the time required for M_x or M_y to decay to 1/e (~37%) of its initial maximum value (Figure 1.5).[5] The transverse relaxation time decays faster than predicted by the molecular mechanism due to magnetic inhomogeneity in B_0 caused by magnetic susceptibility, which induces a field distortion toward the materials placed within the field. Overall, this magnetic inhomogeneity causes the transverse magnetization to decay faster, which is characterized by effective spin-spin relaxation time constant (T_2*).

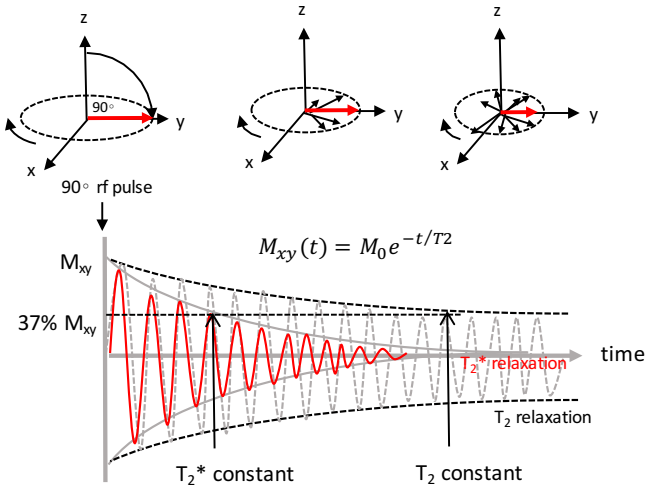

Figure 1.5 Transverse relaxation (T_2) process

1.1.4 Chemical shift

The chemical shift is a unique property of NMR spectrum since it contains chemical structural information. When a nucleus of interest is placed in magnetic field (B_0) the electrons around a nucleus generate a small magnetic field that the opposes the applied B_0. This reduction is called shielding so actual magnetic field by the nucleus will be slightly reduced. The extent of this shielding effect depends upon the electronic environment around the nucleus. Thus, the local effective field experienced by the nucleus is

$$B_{eff} = B_0 - B_{0\sigma} = B_0(1-\sigma) \tag{1.10}$$

Where σ is a non-dimensional shielding constant. This induced shielding effect is about a million times smaller than the applied field. For instance, if the proton Larmor resonance frequency is in the order of megahertz, the difference in resonance frequencies for different proton nuclei will be on the order of a few hertz. This relatively small radiofrequency difference ($\sim Hz$) is hard to

distinguish, thus only the relative position of NMR signals can be determined compared to reference signal. Tetramethylsilane (TMS) or 4,4-dimethyl-4-silapentance-1-sulfonic acid (DSS) is used in ^{1}H and ^{13}C NMR spectroscopy as a reference. The chemical shift (δ) is commonly expressed as a unitless value of parts per million (ppm), where the frequency difference in Hz is divided by spectrometer frequency (Equation 1.11). The typical ranges in chemical shifts of important biochemical samples are shown in Table 1.1.[6-9]

$$\delta = \frac{\sigma_R - \sigma_S}{1 - \sigma_R} \times 10^6 = (\sigma_R - \sigma_s) \times 10^6,\ \sigma_R \ll 1 \tag{1.11}$$

1.1.5 Free Induction Decay

After an applied pulse, the net magnetization vector begins to return to equilibrium. The M_{xy} magnetization induces a current in the receiver coil and the signal is a sine wave oscillating at the Larmor frequency (ω_0), which is detected by free induction decay (FID). This oscillating signal can be detected by NMR spectrometer and these resonant frequencies of the nuclei can be separated and measured. This FID contains the chemical shift information *via* the different frequency components. A typical FID is illustrated in figure 1.6. The time-dependent FID can be converted into a frequency-dependent spectrum *via* Fourier transform (Equation 1.12 and 1.13). The $\cos \omega t$ describes real part (peak absorption) and $i \sin \omega t$ describes the imaginary part (peak dispersion).

$$g\ (\omega) = \int_{-\infty}^{\infty} f(t) e^{i\omega t} dt \tag{1.12}$$

$$e^{-i\omega t} = \cos \omega t + i \sin \omega t \tag{1.13}$$

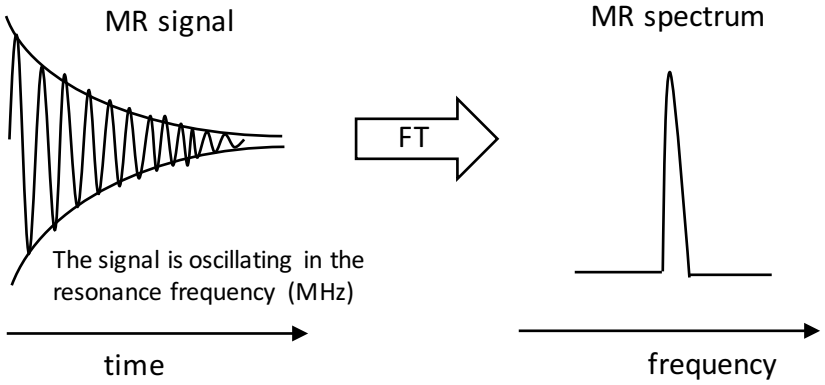

Figure 1.6 Free induction decay and Fourier Transformation

1.1.6 Signal to noise

The signal intensity of conventional NMR is directly proportional to spin polarization (p), the difference in energy of a nuclear moment between two magnetic spin states at Boltzmann equilibrium. The spin polarization is defined by equation 1.14. It is proportional to magnetic field (B_0), gyromagnetic ratio (γ), and inversely proportional to temperature ($P = \frac{B_0}{T}$). However, the Boltzmann distribution near room temperature and conventional magnetic field strength is almost equally populated, and thereby the signal to noise is lower.[10]

$$P = \frac{n_\alpha - n_\beta}{n_\alpha + n_\beta} = \tanh\left(\frac{\gamma \cdot \hbar \cdot B_0}{2 \cdot k \cdot T}\right) \quad (1.14)$$

Where, n_α, n_β is nuclear population of two states.

The signal to noise ratio (SNR) can be considered as the amount of signal per unit time under

fully relaxed pulse-acquired experiment. SNR can be improved by repeating acquisition. The SNR is proportional to $\sqrt{n}$ (n is the number of acquisition), since noise is increased by $\sqrt{n}$ while the signal is increased by n *via* accumulating the spectra. In addition, the SNR at thermal equilibrium can be enhanced by increasing the external magnetic field or decreasing the temperature. However, this effect is not very significant at feasible magnetic fields and temperatures. For instance, the ^{13}C spin polarization at 37 °C is about 1.2 x 10^{-6} and 8.4 x 10^{-6} at 1.5 T and 7 T, respectively. To obtain the maximum signal for a given pulse, repeated acquisitions are needed after the magnetization returns to the equilibrium. The repetition time (TR) in the NMR experiment is determined by T_1 and is usually five times longer the T_1. When signal is acquired repeatedly, the Ernst angle can be employed to minimize the scan time. (Equation 1.15). The Ernst angle is the ideal flip angle for excitation of a spin's maximal signal.

$$\theta_{ernst} = \arccos(e^{-\frac{TR}{T_1}}) \tag{1.15}$$

1.2 Dynamic Nuclear Polarization

1.2.1 Limitations of *in vivo* NMR spectroscopy

In vivo spectroscopy facilitates *in situ* molecular analysis by taking advantage of the fact that the chemical shift of the injected chemical probe can be observed separately from its biochemical products in tissue. However, the intrinsic low sensitivity of conventional NMR methods require high substrate concentrations and is limited to nuclei with high gyromagnetic ratios such as proton, fluorine, or phosphorous. For this reason, ^{31}P NMR and ^{1}H NMR have been most widely applied to various *in vivo* NMR studies. However, practical application of ^{31}P NMR for

biochemical pathway studies is limited as there are only a few phosphorous-containing metabolites in biological systems while ^{1}H NMR is impeded by its limited chemical shift range (~10 ppm). In contrast, ^{13}C NMR is characterized by a large spectral range of over 200 ppm and narrow linewidths, which allows ^{13}C NMR spectroscopy to identify carbon atoms in a particular chemical group of biomolecules. Moreover, most biochemical reactions involve carbon or nitrogen containing molecules so ^{13}C and ^{15}N NMR can detect many different metabolites. However, a major limitation of ^{13}C or ^{15}N NMR spectroscopy is its relatively low sensitivity due to low natural abundance (1.1% of ^{13}C and 0.4% of ^{15}N) and gyromagnetic ratio ($(\gamma_{13C}/\gamma_{1H})$=0.251, $(\gamma_{15N}/\gamma_{1H})$=0.097). These problems result in an extremely weak NMR signal in ^{13}C and ^{15}N in conventional NMR experiments. One strategy is to overcome the low sensitivity by increasing SNR. However, increasing number of acquisition leads to long acquisition time in some ^{13}C or ^{15}N NMR experiments due to their long T_1 values. Increasing sensitivity and decreasing noise can also be achieved by improving RF coil design, but this does not solve the principal problem of low spin polarization. Increasing magnetic field strength or lowering the experimental temperature can enhance the spin-polarization but the gain is not dramatically increased. The SNR enhancement using cryogenic probes[11] is accomplished by reducing the thermal noise in the receiver coil.

The strategy adopted in this dissertation to overcome the low SNR was the increase of spin polarization with dissolution dynamic nuclear polarization (d-DNP) methods. Non-equilibrium spin populations (also known as hyperpolarized spin distribution) can be achieved artificially by various hyperpolarization techniques such as dissolution dynamic nuclear polarization, spin-exchange optical pumping, and para-hydrogen induced polarization (PHIP).[12-21] Among these

methods, d-DNP has been extensively used to polarize a wide range of nuclei including ^{13}C, ^{15}N, ^{1}H, ^{31}P, ^{29}Si, ^{19}F, ^{6}Li,^{133}Cs ^{89}Y and $^{107,109}Ag$, and it is currently the preferred technique to polarize ^{13}C labeled compounds for metabolic studies[6,22-33]. ^{13}C or ^{15}N NMR in combination with dissolution DNP provides opportunities to non-invasively monitor metabolic pathways of interest using hyperpolarized substrates with high sensitivity and contrast against a weak background signal.[34] Metabolic fluxes can be selectively detected by administering the hyperpolarized labeled substrates and observing the signals of downstream metabolites.[35]

1.2.2 Enhancing the MR signal by dynamic nuclear polarization (DNP)

In this section, the principles of DNP are discussed. A more thorough review of DNP can be found in many references.[6,12,13,18,23,25,36] DNP is a technique that significantly increases the signal-to-noise ratio of NMR signals by enhancing the polarization of nuclear spins in samples containing a paramagnetic component.[37,38] This technology overcomes the issue of inherently low sensitivity of conventional NMR by efficiently producing non-equilibrium spin distribution on the Zeeman levels. At the same magnetic field and temperature, the polarization of the electron spin is much higher than proton nuclear spin due to the higher magnetic moment of the electron spin. For instance, at 90K, the polarization of electron spin is 10.541% while the polarization of the proton nuclear spin is 0.016%. At a 1.4K, the electron polarization is 96% while the carbon polarization is 1.96% (Figure 1.7).

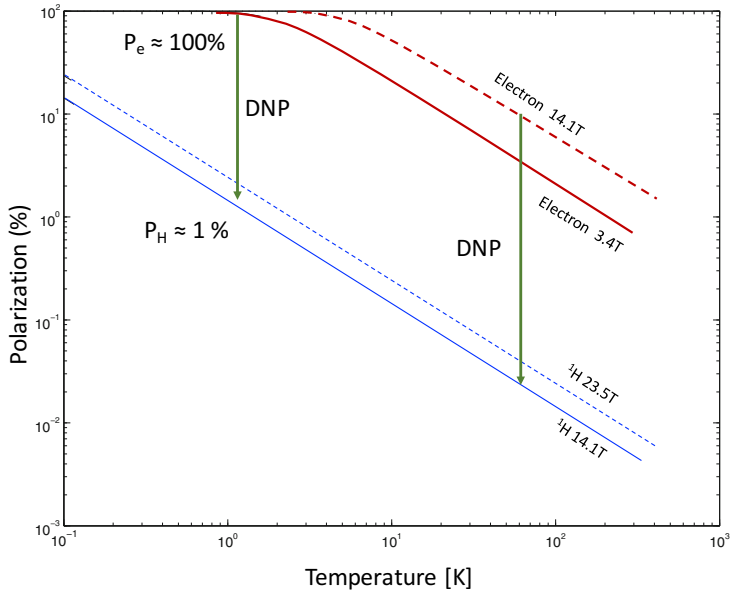

Figure 1.7 Temperature dependence of the polarization level of electron and ^{1}H, Polarization levels are calculated based on Equation 1.14. Adapted from reference[39]

The theoretical framework of DNP was initially proposed by Albert Overhauser[40] and experimentally demonstrated by Carver and Slichter[41] in 1953. During the DNP process, the maximum enhancement of nuclear spin polarization is governed by the gyromagnetic ratio between electron and nuclear spins (γ_e/γ_n), which corresponds to the factor of ~660 for ^{1}H and ~2600 for ^{13}C nuclei. These signal enhancements can be significantly affected by several DNP parameters, such as magnetic field, temperature, microwave irradiation, electron polarization agent, polarized agent, and matrix. By translating the physical theory of DNP into practical application *via* d-DNP, many biological studies have been achieved.

1.2.3 DNP mechanisms

DNP can be achieved by several mechanisms including the Overhauser effect, the solid effect,

the cross effect, and thermal mixing.[36] However, none of these mechanisms are exclusive and polarization occurs by combination of one or more mechanisms. The most effective DNP mechanism depends on the experimental condition such as EPR linewidth and experimental temperature in samples. In particular, the frozen solution or solid system follows the solid effect and thermal mixing mechanism as their DNP process.[36,38] Under the current dissertation study, dominant mechanisms include the solid effect and thermal mixing. These are discussed briefly below.

1.2.3.1 Solid effect

In 1958, Abragam and Proctor proposed that the enhancement of nuclear polarization could be accomplished by forbidden transitions of W_2 and W_0 *via* microwave irradiation[42,43] if the frequency corresponds to the energy difference $(\nu_s \pm \nu_I)$ (Solid effect).[44,45]

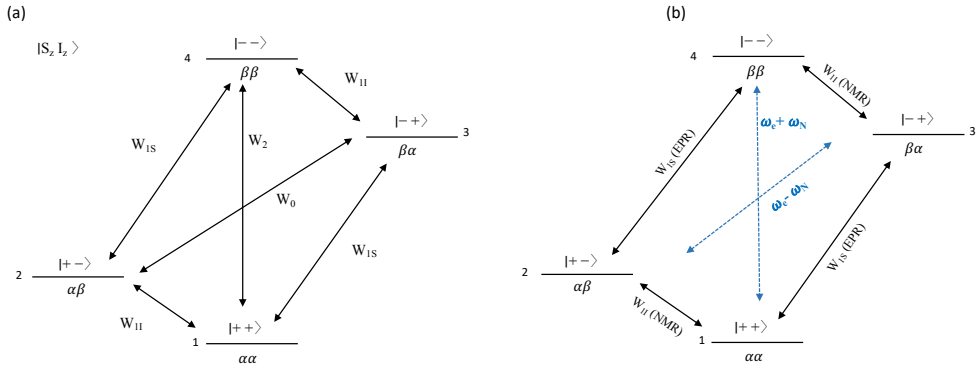

Figure 1.8 Energy level diagram to illustrate the solid effect. (a) The energy level diagram for electron spins coupled to a nuclear spins (I=1/2). W_{1s} and W_{1I} are the transition probabilities for EPR and NMR. (b) Transition frequencies for positive and negative enhancements are presented by blue lines, respectively

This process is easy to understand by considering the four possible spin states, which are generated by hyperfine interaction of an electron spin (S =1/2) coupled to proton (I =1/2) (Figure 1.8.a).[39] W_{1s} and W_{1I} are transition probabilities that flip only one electron (S) or the nuclear quantum number (I). W_0 (flip-flop) and W_2 (flip-flip) are zero and double quantum transition probability involving no or two changes of spin states and the forbidden transitions. The enhancement of nuclei polarization is occurred by hyperfine coupling, a mixing of spin state *via* coupling of electron-nuclear spin under the influence of microwave irradiation. This coupled electron-nuclear spin states allow the forbidden transitions. The enhancement becomes maximal when the irradiation frequency equals to the sum of electron Larmor frequency and nuclear Larmor frequency ($\omega = \omega_e + \omega_n$), while it becomes the most negative when the frequency equals to the difference ($\omega = \omega_e - \omega_n$) (Figure 1.8.b).[46] The solid effect DNP mechanism is efficient under the condition where the electron spin concentration is low, resulting in the negligible electron-electron interaction.[47] The EPR linewidth of free radical in the sample needs to be much less than the nuclear Larmor frequency, which is termed as "well-resolved solid effect". If it is not much less than the nuclear Larmor frequency, the enhancement is reduced, which is termed as "differential solid effect". For this reason, low concentration of narrow-linewidth radicals such as OX063 and BDPA are desired in solid effect DNP.[48]

1.2.3.2 Thermal mixing

Thermal mixing is a phenomenon of energy exchange between electron spin and nuclear spin ensemble. This effect occurs under the high concentration of unpaired electrons, which results in homogeneously broadening of ESR linewidth (δ) caused by the multiple dipolar

coupled electrons under the condition of $\delta > \omega_N$.[49] Since high radical concentration is used in thermal mixing process, electron spin ensemble presents strong inter-electron interaction as a group and not as an individual spin. For this reason, it is better to understand the mechanism with spin temperature model and thermodynamic ensembles rather than with individual energy states. In DNP *via* thermal mixing mechanism, the polarization transfer is due to the interaction of three thermodynamic system associated with spin temperature: nuclear Zeeman system (NZS), electron Zeeman system (EZS), and electron dipolar system (EDS). These strong interactions cause a homogeneously broadened EPR line of implicated paramagnetic species in sample. Thermal mixing mechanism proceeds driven by irradiation of allowed EPR transition. Initially, the microwave irradiating adds energy to the electron spin system. The mutual interaction H_{SS} between the electron spins distributes this energy, so that the spin temperature of EZS heats up and EDS cools down. Subsequently, the coupling H_{SI} between EDS and NZS combines with H_{SS} to cool the NZS, and the transition energy between EDS and NZS are effectively decreased (Figure1.9). As a result, the polarization is transferred from electrons to nuclei through mutually flips coupled three spins, electron-electron-nucleus. This mechanism is only effective when the EPR linewidth is more than or equal to the nuclear Larmor frequency and electron spin system is locally equilibrium.

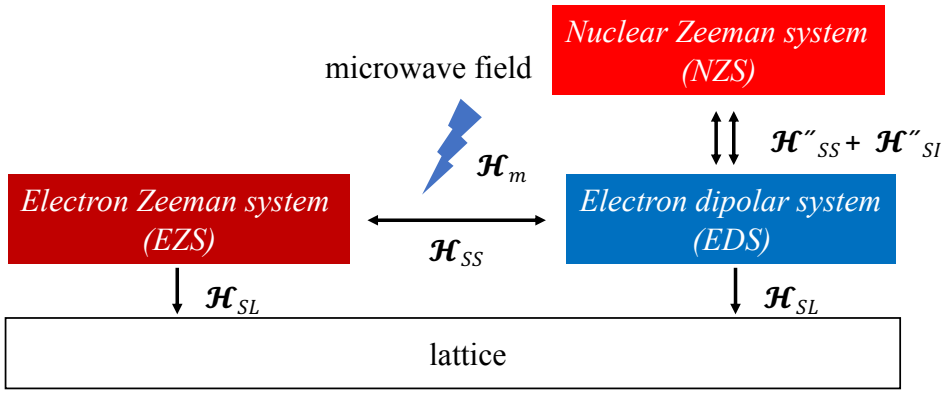

Figure 1.9 Schematic diagram of the energy flow in three spin system (adapted and modified from reference[50])

Thermal mixing is considered the primary mechanism for d-DNP and more suitable to the low-γ nuclei like ^{13}C and ^{15}N. The narrow linewidth of free radical such as trityl and BDPA are optimal for the polarization. This effect become dominant when $\omega_n = \omega_{e1} - \omega_{e2}$ is comparable to the EPR linewidth $\omega_{1/2}$ and maximal under the condition of $\omega \approx \omega_e \pm \omega_{1/2}$.

1.2.4 Experimental approach for dissolution DNP

Griffin and co-workers were the first to apply dynamic nuclear polarization to solid state NMR for structural biology applications.[51-54] In 2003, Ardenkjaer-Larsen and co-workers developed a fast dissolution technique that allows frozen samples in the solid state to be brought into the liquid state at room temperature while retaining ~10,000-fold NMR signal enhancement compared to the same concentration of unpolarized sample (Figure 1.10).[35] In that study, ^{13}C-urea was polarized in a glycerol-glassing matrix doped with a trityl as free radical. The electron spin polarization was transferred to ^{13}C nuclei by optimal microwave irradiation (93.952 GHz, 100mW) low temperature (~1.1K) and high magnetic field (3.35T).

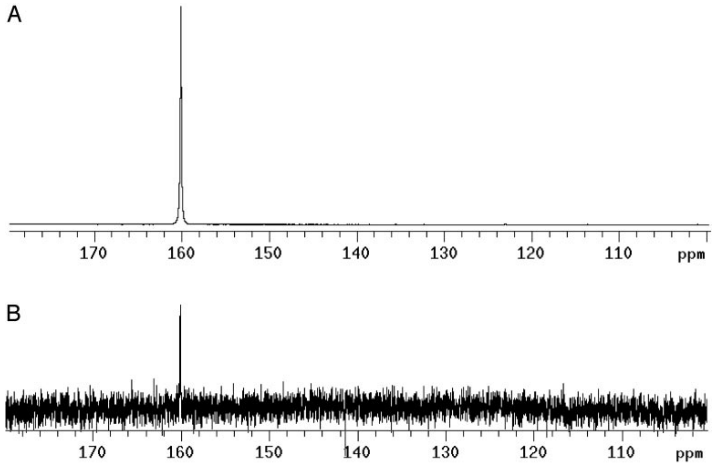

Figure 1.10 (A) ^{13}C spectrum of urea (natural abundance ^{13}C) hyperpolarized by the DNP-NMR method. The concentration of urea was 59.6 mM, and the polarization was 20%. (B) Thermal equilibrium spectrum of the same sample at 9.4 T and room temperature. This spectrum was acquired under Ernst-angle conditions (pulse angle of 13.5° and repetition time of 1 s based on a T_1 of 60 s) with full ^{1}H decoupling. The signal is averaged during 65 h (232,128 transients). Reproduced with permission from reference[35]

The d-DNP sample consists of a ^{13}C or ^{15}N labeled compound of interest, an organic free radical as free electron source, and a glassing matrix for homogeneous distribution of the labeled compound and the radical in the sample. If desired, a paramagnetic lanthanide complex can be used to speed up the polarization time. Gd^{3+}, Ho^{3+}, Dy^{3+}, and Tb^{3+} complexes have been all used.[55] For instance, adding an optimized concentration of Gd^{3+} and Ho^{3+} into hyperpolarized sample of [1-^{13}C] pyruvate or [1-^{13}C] sodium acetate not only increases the achievable polarization level but also accelerates the polarization build-up time.[55,56] At the same time, these lanthanide ions also play the role of a relaxation agent in the liquid state and slightly shorten the T_1 values of hyperpolarized probes. The selection of glassing matrix is typically based on the solubility of labeled substrate and free radicals. In general, mixture of glycerol and water, DMSO, ethylene glycol, methanol, or ethanol can be used as glassing matrix. As previously discussed, the free

radical can be chosen based on EPR linewidth and solubility in the matrix. The chemical structures of a few stable organic free radicals used in d-DNP are shown in Figure 1.11.[6] The trityl radical (OX063) is most often used for d-DNP since it has favorable solubility for aqueous dissolution medium. The polarization transfer is achieved by microwave irradiation near the EPR frequency of the free radical (94GHz, at 3.35 T) at a cryogenic temperature (~1K). The solid-state polarization reaches a plateau around ~ 2 to 4 hrs for a typical ^{13}C sample. The frozen sample is dissolved by the addition of superheated dissolution medium and the resulting solution is ready for *in vivo* and *in vitro* studies.[35,57] In general, aqueous buffers are used as dissolution media for biological experiments. EDTA (ethylenediaminetetraacetic acid), a chelating agent, is often used to remove paramagnetic ion impurities in the dissolution media or hyperpolarized sample.

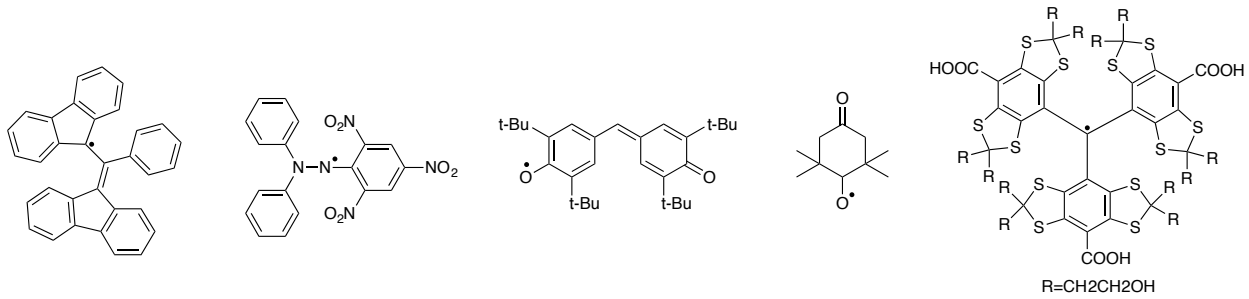

Figure 1.11 Chemical structures of stable organic free radicals used as polarizing agents in dissolution DNP.

The dissolved hyperpolarized sample usually needs to be used for NMR studies within a minute following dissolution to minimize T_1-dependent loss of HP signal.[6] The hyperpolarized probes are introduced into biological systems to detect biological events with high sensitivity and

contrast against background signals. The schematic diagram of the dissolution DNP experiment is shown in Figure 1.12. The d-DNP technique has been used successfully to generate hyperpolarized ^{13}C and ^{15}N nuclei for ^{13}C and ^{15}N applications *in vivo* or *in vitro* system.[58-69] A commercial dissolution DNP polarizer[58] such as the HyperSense (Oxford Instruments) or SPINlab (GE Healthcare) were used in this study. T_1 dependent HP signal decay after dissolution is a major limitation which motivates the development of long T_1 agents.

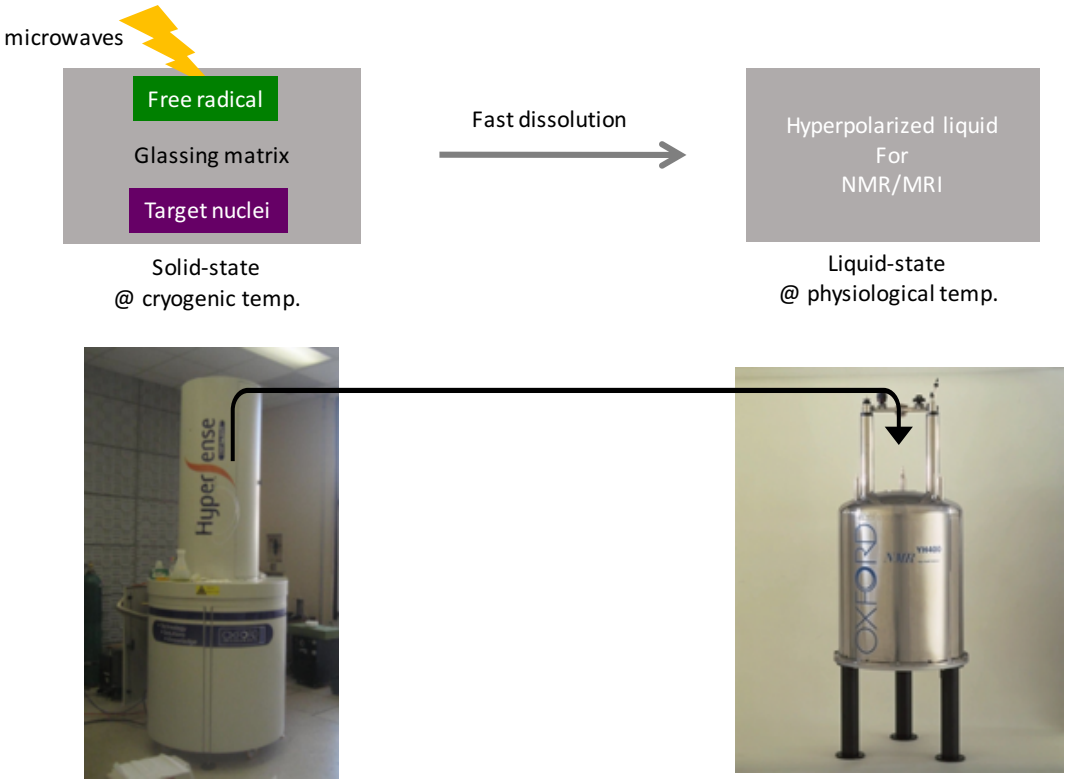

Figure 1.12 Schematic diagram of the dissolution DNP experiment

1.2.4.1 Liquid-State NMR enhancement

As the NMR signal intensity corresponds to spin temperature (T_S) of the nuclear spin system[45,70], the d-DNP-enhanced polarized NMR signal (P_{hp}) also corresponds to a spin temperature T_S expressed as $P_{hp} = \tan(h\upsilon_n/2\kappa_B T_S)$. Here P_{th} is the thermal polarization at a given lattice temperature T_L. Overall, the NMR signal enhancement of DNP-enhanced polarization can be defined by

$$\varepsilon = \frac{P_{hp}}{P_{th}} = \frac{\tan(h\upsilon_n/2K_B T_S)}{\tan(h\upsilon_n/2K_B T_L)} \tag{1.16}$$

Experimentally, the NMR signal enhancement (ε) is determined by the relative ratio of integrated area: T_1-corrected hyperpolarized (HP) signal A_{hp} over the thermal equilibrium NMR signal A_{th}. Since the NMR signal is proportional to rf flip angle, the ratio ($\sin\theta_{th}/\sin\theta_{hp}$) reflect the rf flip angle correction factor, while the sample concentration correction factor (c_{th}/c_{hp}) should be counted so that the ratio of the signal intensity in hyperpolarized and thermal equilibrium state are equally attributed to spin count.[32]

$$\varepsilon = \left\{\left(\frac{A_{hp}}{A_{th}}\right)\left(\frac{\sin\theta_{th}}{\sin\theta_{hp}}\right)\left(\frac{c_{th}}{c_{hp}}\right)\exp\left(\frac{t}{T_1}\right)\right\} \times \ number\ of\ scan_{th} \tag{1.17}$$

where the subscripts hp and th represent the values measured in the hyperpolarized and thermal equilibrium states, respectively. The NMR signal intensity is also proportional to the number of acquisition so it needs to be normalized based on number of scans. Typically, only the number of acquisitions of thermal signal is counted since hyperpolarized signal is acquired in 1 scan.

1.2.4.2. Liquid-State hyperpolarized magnetization decays by T_1 relaxation

After dissolution of a hyperpolarized sample, the Z-magnetization returns to thermal equilibrium due to T_1 relaxation. For example, Figure 1.13 shows the decay of hyperpolarized magnetization of ^{15}N TPA in water. The T_1 value of the polarized sample can be determined from the decay of hyperpolarized signal by fitting of hyperpolarized NMR signal decay to Equation 1.18[57], which takes into account the effect of rf pulse with given flip angle[71].

$$I(t) = I_0 \sin\theta \, (\cos\theta)^{t/TR} exp^{-t/T_1} \tag{1.18}$$

In this equation, $I(t)$ is the intensity of the ^{13}C MR at time t, I_0 is the initial magnetization, TR is repetition time, and θ is the flip angle of rf pulse used to monitor the hyperpolarization signal. The $\sin\theta$ refers transversal (xy) component of magnetization, $(\cos\theta)^{t/TR}$ refers to destroyed magnetization by pulsing, and exp^{-t/T_1} denote the effect of loss of magnetization due to T_1 decay.

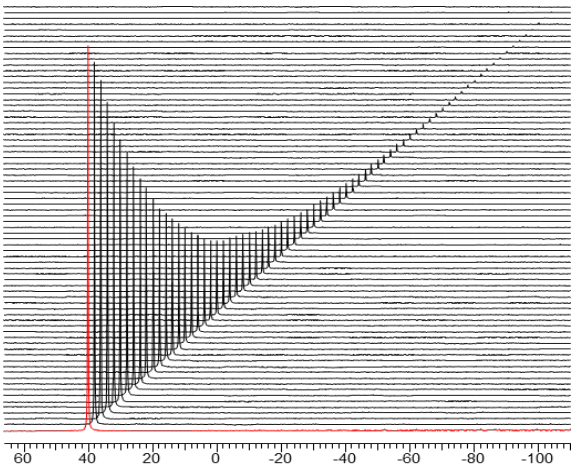

Figure 1.13 Sequential ^{15}N NMR spectra of hyperpolarized sample of TPA showing polarization decay. Spectra were collected every 5sec using a 5 degree pulse.

There are several mechanisms that contribute to the longitudinal relaxation rate R_1 ($R_1 = 1/T_1$) of hyperpolarized nucleus: dipole-dipole (R_d), paramagnetic relaxation (R_{para}), chemical shift anisotropy (R_{cas}), scalar coupling relaxation (R_{sc}), and spin-rotation (R_{sr}). Each mechanism can be defined by a time-dependent Hamiltonian operator that denotes the probability of spin transition caused by specific mechanism (Equation 1.19).[72] If the paramagnetic relaxation mechanism is excluded[73], relaxation of hyperpolarized signal is predominantly driven by a dipole-dipole interaction and chemical shift anisotropy (CSA).[74]

$$R_1 = \frac{1}{T_1} = \sum_i R_i = R_d + R_{para} + R_{csa} + R_{sr} + R_{Sc} \quad (1.19)$$

The dipole-dipole coupling is the magnetic interaction between two coupled nuclear spins. The dipolar relaxation of a nucleus in a molecule depends on the nature and the distance between the nucleus and nearby nuclear spins as described by Equation 1.20. The dipolar relaxation is due to local oscillating magnetic fields generated by nuclear spins as the molecule tumbles in solution.

$$1/T_{1,dipolar} = \tau_c \gamma_i^2 \gamma_j^2 \hbar^2 / r^6 \quad (1.20)$$

where $\tau_c$is the correlation time for rotational motion, and r is the distance between molecular probe nuclei (i) and adjacent dipolar coupled nuclei (j). T_1 and T_2 relaxation times as a function of τ_c correlation time for spin-1/2 nuclei by dipole-dipole mechanism is given in Figure 1.14.[70] Specially, ^{1}H nuclei are strongly dipolar coupling to directly bonded ^{13}C and^{15}N nuclei[75]. For this reason, quaternary ^{13}C and ^{15}N atoms have longer T_1 values on protonated C-H or N-H atoms.

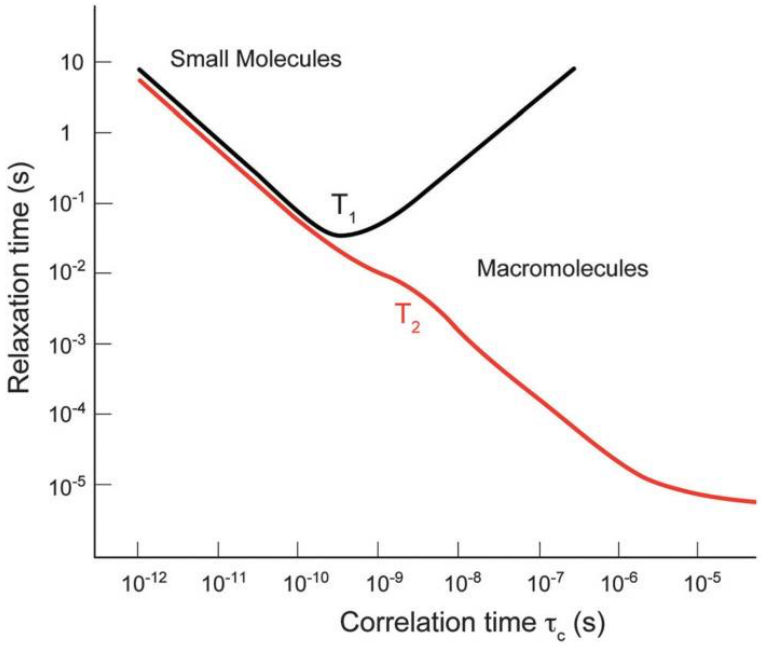

Figure 1.14 Behavior of T_1 and T_2 as a function of correlation time for spin 1/2 nuclei relaxing by the dipole-dipole mechanism (Reproduced with permission from reference[6])

Another major mechanism of relaxation is the chemical shift anisotropy (CSA) within the external magnetic field. The chemical shift is a tensor quantity and random molecular motions lead to fluctuation in local magnetic fields caused by anisotropic electron distribution. This effect is more dominant for nuclei with low gyromagnetic ratio and wide chemical shift ranges. CSA

contributes to longitudinal relaxation in proportion to the magnetic field (B) and chemical shift anisotropy ($\Delta\sigma$)[76] (Equation 1.21). To minimize the CSA effect on longitudinal relaxation, the hyperpolarized probes need to have a more symmetrical structure at the atom of interest since symmetrical structures have lower contributions from CSA.

$$1/T_{1,CSA} = 2\tau_c\gamma_i^2 B_0^2(\Delta\sigma)^2/15 \quad (1.21)$$

$$\Delta\sigma = \left[2\sigma_{zz} - \left(\sigma_{xx} + \sigma_{yy}\right)\right]/3 \quad (1.22)$$

1.3. Dissolution DNP in studies of cancer metabolism

One of the recently added cancer hallmarks is reprogramming of cellular energy metabolism. Cancer promotes reprogramming of cell metabolism for sustained cancer cell growth and proliferation.[77] As the first concept of metabolic reprogramming in cancer, Otto Warburg proposed the "Warburg effect" which describes how tumor metabolism differs from the surrounding tissue by increased glycolytic activity and reduction of oxidative phosphorylation in mitochondria compared with normal tissue even under aerobic conditions.[78] Theses metabolic alterations were thought to be caused by mitochondrial dysfunction associated with mitochondrial DNA mutations, mitochondrial enzyme defects, or altered tumor suppressors.[79-82] Therefore, cancer metabolism can be understood to be a collective representation of independent biochemical pathways, each pathway providing a specific function in metabolic reprogramming.[83,84] The biochemical pathways altered in cancer metabolism includes glycolysis, the pentose phosphate pathway, the tricarboxylic acid cycle, oxidative phosphorylation, and the synthesis of nucleotides and lipids.[85] In addition, another notable alternation in tumor tissue is

the reduction of glutamine metabolism and an increase in glutamine uptake into cell. These metabolic demands in cancer drive altered utilization of metabolic substrates such as glucose,[78] glutamine,[86] acetate,[87,88] and branched-chain amino acids.[89] Therefore, *in vivo* molecular imaging using isotope tracers of specific enzyme-catalyzed biological reaction that are altered in cancer compared to surrounding normal appearing tissue would be a key to detect abnormality of cancer metabolism. These characteristics can be detected by hyperpolarized MR imaging techniques using ^{13}C and ^{15}N labeled hyperpolarized molecular probes. Figure 1.15 shows a schematic presentation of metabolic pathways with a various ^{13}C and ^{15}N labeled TCA cycle intermediates that have been used as HP imaging probes in cancer metabolism.

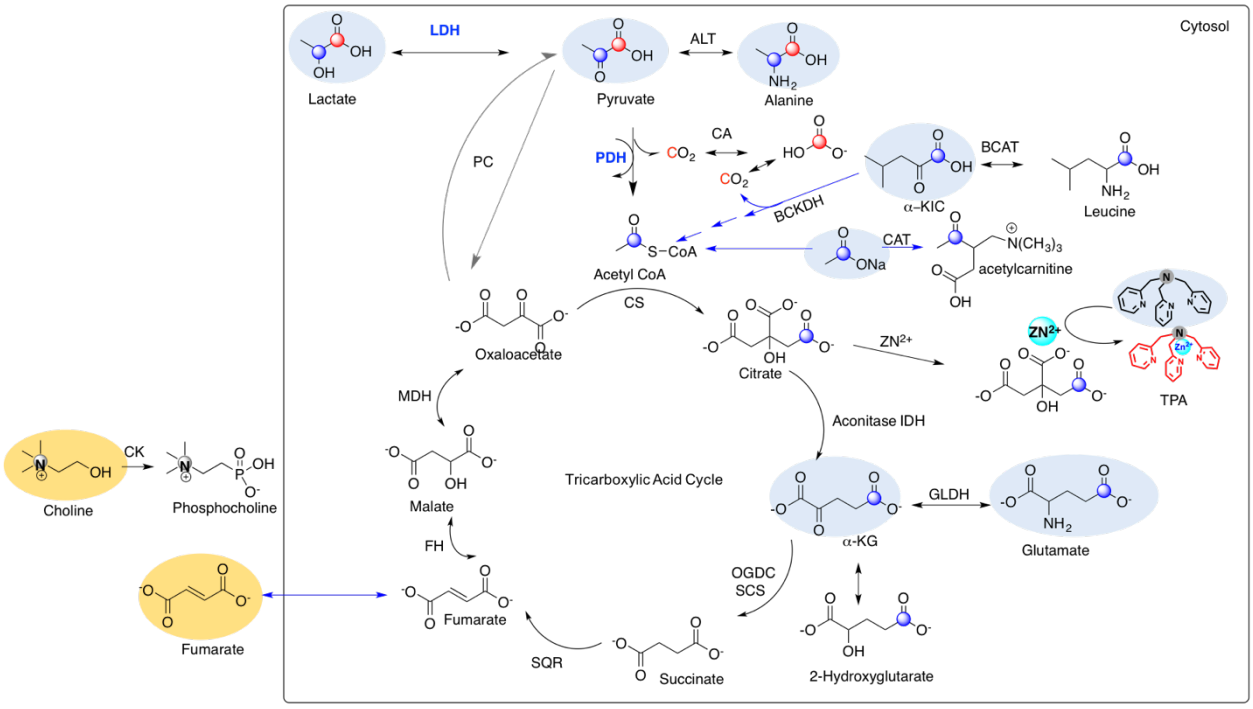

Figure 1.15 Biochemical scheme that summarizes the labeled products that are generated from various widely used ^{13}C metabolic probes. Hyperpolarized substrates that have been used in HP experiments are presented as blue and orange circles. Red and blue dots represent a ^{13}C label that either exchanges with other existing pools (i.e., alanine and lactate) or passes into the TCA cycle and enters downstream products. Grey dots reflect ^{15}N labeled substrates LDH-Lactate dehydrogenase, ALT-alanine transaminase, CA-carbonic anhydrase, PC-pyruvate carboxylate, CAT-carnitine acetyltransferase, PDH-pyruvate dehydrogenase complex, PC-pyruvate carboxylase, CS-citric synthase, IDH-isocitrate dehydrogenase, OGDC-oxoglutarate dehydrogenase complex, SCS-succinyl coenzyme A synthetase, SQR-succinate dehydrogenase, FH-fumarate hydratase, MDH-malate dehydrogenase, GLDH-glutamate dehydrogenase, BCAT-branched chain amino acid transferase, BCKDH-branched chain *α*-ketoacid dehydrogenase complex (adapted and modified from reference[6])

Over the decades, various molecular imaging techniques have been developed to non-invasively detect cancer-specific metabolic changes for cancer diagnosis or therapeutic intervention. Hyperpolarized ^{13}C MR *in vivo* imaging can easily be compared to positron emission

tomography (PET) which has been extensively used for *in vivo* molecular imaging in preclinical and clinical settings. PET tracers typically display high specificity in molecular targeting, and utilize biologically active substances without alternating the biological processes. High sensitivity can be achieved by administering picomolar quantities PET tracers which is negligible to their endogenous levels of metabolites accounting for physiological function. This condition conserves endogenous metabolic substrate behavior.[90] Although the use of PET tracers can provide sensitivity in the nano - picomolar range, the lack of spectral information limits the biological information obtained compared to hyperpolarized NMR. PET only reports uptake of the injected radiolabeled tracer rather than downstream metabolites. Another disadvantage of PET is the use of ionizing radiation.^{13}C DNP coupled with NMR spectroscopy is a robust method for simultaneously detecting multiple hyperpolarized ^{13}C labeled metabolic products derived from an injected hyperpolarized ^{13}C molecule based upon differences in their chemical shifts. This allows simultaneous observation of multiple metabolic pathways in real-time. This dissertation work focuses on the application of ^{13}C and ^{15}N labeled hyperpolarized molecular probes for potential imaging of cancer metabolism. To aid discussion of this topic, a brief overview of biological applications of hyperpolarized MR probes is given in the following section.

1.4 Hyperpolarized NMR probes

The stable isotope-labeled HP probes can be classified into three categories. First is an endogenous molecular probe that minimally modifies natural compounds by ^{13}C, ^{15}N, or ^{2}H enrichment, enhancing NMR properties without altering the chemical properties. This type of probe is inherently biocompatible when used in near-physiological concentrations. Most isotope

labeled metabolite substrates belong to this category.[91] Second is non-endogenous molecular probes designed as biochemical sensors to monitor biologically important chemical species.[31,32,34,92,93] The design of these probe included a long T_1 nucleus for detection of reactions of interest based upon NMR chemical shift changes. Non-endogenous probes should have biocompatible properties. The third category of probes is derivatives of endogenous molecular probes modified to improve biocompatibility or hyperpolarization lifetimes. Examples include esters,[94,95] anhydrides,[96] and pre-methylated amino acid modifications[75] that improve the cellular uptake and polarization lifetimes. Optimized hyperpolarized HP probe provide molecular information, spectral resolution with low background interference, and minimal invasiveness for the biological study. To apply DNP technology *in vivo*, it is necessary to develop HP probes enriched with ^{13}C or ^{15}N, a long polarization half-life and rapid incorporation into biological pathway of interest.

1.5 Biological applications of d-DNP

Hyperpolarized probes can be used to study *in vitro*, in cell-based systems, and *in vivo* to perform biological assays that are detectable by NMR with high sensitivity and high contrast against a background signal.[91] The use of NMR spectroscopy with hyperpolarized probes enables variety of biological studies such as metabolic conversion, kinetic profiling of cellular reactions,[97-100] monitoring changes in pH,[31,101-103] examining redox state,[104-106] detecting reactive oxygen species,[107] measuring ion concentrations,[108,109] and evaluating drug efficacy.[29,110-112] Figure 1.16 illustrates applications of the probes described in this dissertation.

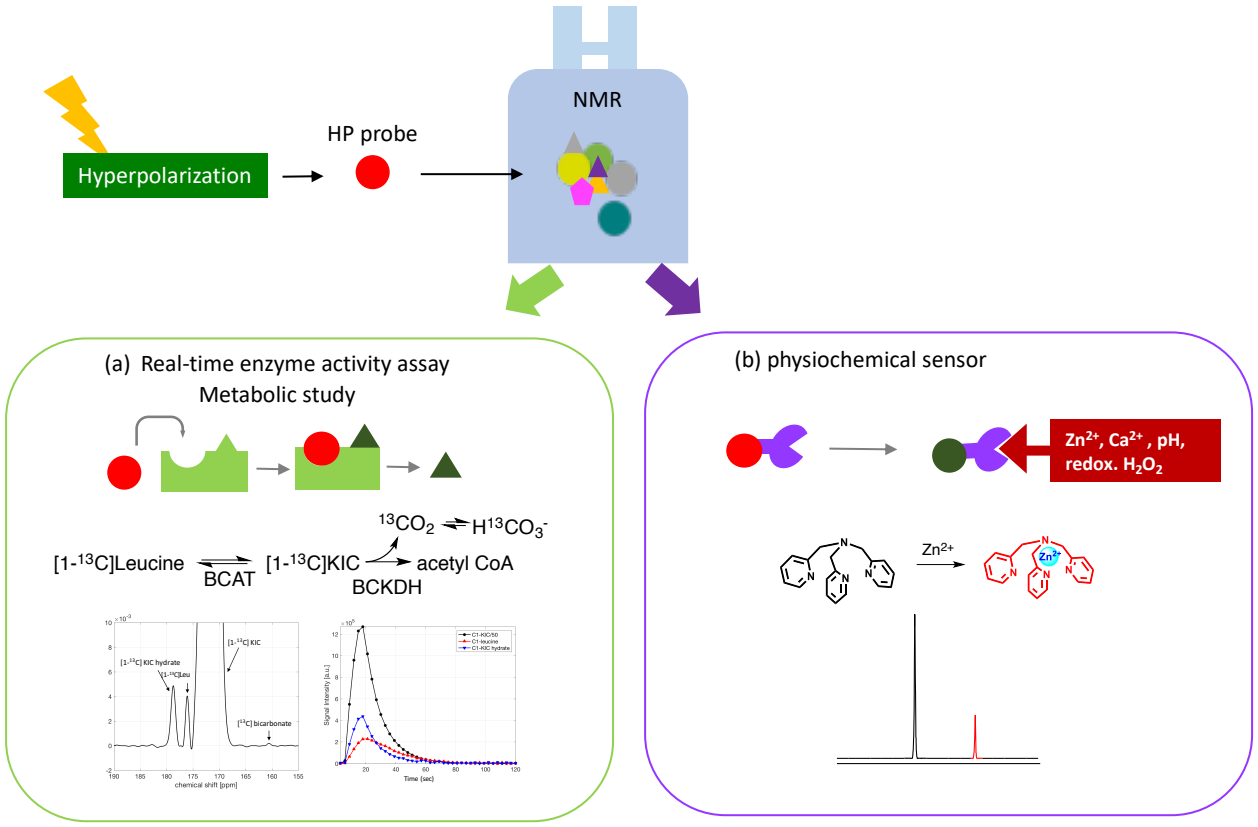

Figure 1.16 Schematics of biological application of dissolution DNP (a) Metabolism of [1-^{13}C]KIC in reaction catalyzed by the enzymes BCAT and BCKDH (b) Hyperpolarized MR probe targeting Zn^{2+}

1.5.1 Real time *in vivo* study of enzymatic reactions

The chemical shift dispersion offered by high-resolution NMR allows hyperpolarized NMR probes to simultaneously detect multiple sequential and parallel biochemical reactions. A metabolic conversion of hyperpolarized metabolic molecule can be monitored over time for sequential metabolic conversion, which yields real-time reaction monitoring.[113] Applications of hyperpolarized molecule that have been studied in real-time to probe enzymatic metabolic reactions are presented in Figure 1.16.a. It shows the metabolic profiling of [1-^{13}C]leucine and ^{13}C bicarbonate by BCAT and BCKDH enzyme activity using hyperpolarized [1-^{13}C]KIC in the

murine glioma brain.[114] The *in vivo* metabolic probe shows the flux of the hyperpolarized signal with dynamics and high resolution. Among the many of enzyme substrates, ^{13}C labeled pyruvate is the most commonly used substrate as *in vivo* metabolic imaging probe since pyruvate is a central metabolite for important metabolic pathway.[115,116] Pyruvate is easily transported into intercellular space and is converted into lactate, bicarbonate, and further downstream to different metabolites. Due to its relatively long T_1 and biocompatibility,[113] hyperpolarized pyruvate has been investigated in isolated cells,[98,117] isolated perfused hearts,[118] and even in clinical studies of human prostate[119] and human heart[120]. It has been demonstrated that hyperpolarized [1-^{13}C] pyruvate can detect the real time metabolism of a single enzyme-catalyzed reaction in perfused heart.[118] The experiments showed metabolic conversion of [1-^{13}C]pyruvate into [1-^{13}C]lactate catalyzed by LDH, [1-^{13}C]alanine by catalyzed by ALT, and $^{13}CO_2$ by catalyzed by carbonic anhydrase (CA) in parallel through a single acquisition. In addition, measurements of metabolic flux can be calculated based on the kinetic information with a 1-second temporal resolution[121] due to the hyperpolarized NMR sensitivity.

1.5.2 *In vivo* sensors

^{13}C or ^{15}N labeled hyperpolarized probes with capacity of sensing physiological parameters have been used to measure pH,[31,101-103] redox state,[104-106] and reactive oxygen species[107] by detecting chemical shift changes. The ratio of signal between HP probes and reacted products can be used for quantitative and qualitative analysis. One of the application of HP sensors is the use of hyperpolarized probe to detect molecular interactions with biologically important metal ions such as Zn^{2+} and Ca^{2+}.[34,108,109] For instance, it has been shown that HP ^{15}N TPA used to detect

the Zn^{2+} by monitoring its chemical shift change (Figure 1.16.b). Upon binding to Zn^{2+}, the molecular environment of HP ^{15}N TPA is changed and resulted in alternation of the chemical shift. If the binding is reversible, the exchange rate between metal-bound ligand and free ligand also affects the NMR signal. These hyperpolarized chemical probe sensors have been designed as a combination of sensing and signaling moieties. The signaling part is composed of enriched stable isotope for MR sensitivity. The sensing part ensures selectivity for the analyte of interest. This coupled sensing and signaling moieties should induce definite changes in the NMR detectable signal. This change includes not only in chemical shift but also in spectrum linewidth, or in hyperpolarization signal decay. Furthermore, hyperpolarized probes have various applications such as probing drug binding,[29,110,122] monitoring drug mechanism,[112] and covalent chemical labeling of amino acid.[123,124] DNP application can be found more in the reference.[6,91,125]

1.6 References

1. Bloch F, H.W., Packard M. . The nuclear induction experiment. *Phys Rev* 70, 474-485 (1946).

2. Bloch F, H.W., Packard M. Nuclear Induction. *Phys Rev* 69, 127 (1946).

3. Nishimura, D.G. Principles of magnetic resonance imaging. (1996).

4. Lambert, J.B., Mazzola, E.P. & Ridge, C. Nuclear magnetic resonance spectroscopy : an introduction to principles, applications, and experimental methods. (2019).

5. Ridgway, J.P. Cardiovascular magnetic resonance physics for clinicians: part I. *Journal of cardiovascular magnetic resonance : official journal of the Society for Cardiovascular Magnetic Resonance* 12, 71 (2010).

6. Keshari, K.R. & Wilson, D.M. Chemistry and biochemistry of 13C hyperpolarized magnetic resonance using dynamic nuclear polarization. *Chemical Society Reviews* 43, 1627-1659 (2014).

7. White, R.E. & Hanusa, T.P. Prediction of 89Y NMR Chemical Shifts in Organometallic Complexes with Density Functional Theory. *Organometallics* 25, 5621-5630 (2006).

8. APPENDIX II - Table of constants and conversion factors. in *Handbook of MRI Pulse Sequences* (eds. Bernstein, M.A., King, K.F. & Zhou, X.J.) 960-962 (Academic Press, Burlington, 2004).

9. Weast, R.C. & Astle, M.J. *CRC handbook of chemistry and physics : a ready-reference book of chemical and physical data*, (The CRC Press, Boca Raton, Fla., 1982).

10. Jeffries, C.D. Dynamic Orientation of Nuclei. 14, 101-134 (1964).

11. Frossati, G. Polarization of 3He, D2 (and possibly 129Xe) using cryogenic techniques. *Nuclear Instruments and Methods in Physics Research Section A: Accelerators, Spectrometers, Detectors and Associated Equipment* 402, 479-483 (1998).

12. Kuhn, L.T. Topics in Current Chemistry 338. Hyperpolarization Methods in NMR Spectroscopy. (Springer, Berlin, Heidelberg, 2013).

13. Viale, A. & Aime, S. Current concepts on hyperpolarized molecules in MRI. *Curr Opin Chem Biol* 14, 90-96 (2010).

14. Canet, D*., et al.* Para-hydrogen enrichment and hyperpolarization. *Concepts Magn Reson A* 28A, 321-330 (2006).

15. Lee, J.H., Okuno, Y. & Cavagnero, S. Sensitivity enhancement in solution NMR: Emerging ideas and new frontiers. *Journal of magnetic resonance (San Diego, Calif. : 1997)* 241, 18-31 (2014).

16. Nikolaou, P., Goodson, B.M. & Chekmenev, E.Y. NMR hyperpolarization techniques for biomedicine. *Chem - Eur J* 21, 3156-3166 (2015).

17. Glöggler, S., Colell, J. & Appelt, S. Para-hydrogen perspectives in hyperpolarized NMR. *Journal of magnetic resonance (San Diego, Calif. : 1997)* 235, 130-142 (2013).

18. Siddiqui, S.*, et al.* The use of hyperpolarized carbon-13 magnetic resonance for molecular imaging. *Adv Drug Deliv Rev* 113, 3-23 (2017).

19. Adams, R.W.*, et al.* Reversible Interactions with para-Hydrogen Enhance NMR Sensitivity by Polarization Transfer. *Science* 323, 1708 (2009).

20. Halse, M.E. Perspectives for hyperpolarisation in compact NMR. *TrAC Trends in Analytical Chemistry* 83, 76-83 (2016).

21. Roos, J.E., McAdams, H.P., Kaushik, S.S. & Driehuys, B. Hyperpolarized Gas MR Imaging: Technique and Applications. *Magnetic Resonance Imaging Clinics of North America* 23, 217-229 (2015).

22. Ardenkjaer-Larsen, J.H., Johannesson, H., Petersson, J.S. & Wolber, J. Hyperpolarized molecules in solution. *Methods Mol. Biol. (New York, NY, U. S.)* 771, 205-226 (2011).

23. Kockenberger, W. Dissolution dynamic nuclear polarization. *eMagRes* 3, 161-170 (2014).

24. Guenther, U.L. Dynamic nuclear hyperpolarization in liquids. *Top. Curr. Chem.* 335, 23-70 (2013).

25. Dutta, P., Martinez, G.V. & Gillies, R.J. A new horizon of DNP technology: application to in-vivo 13C magnetic resonance spectroscopy and imaging. *Biophysical Reviews* 5, 271-281 (2013).

26. Yen, Y.-F., Nagasawa, K. & Nakada, T. Promising application of dynamic nuclear polarization for in vivo 13C MR imaging. *Magn Reson Med Sci* 10, 211-217 (2011).

27. van Heeswijk Ruud, B.*, et al.* Hyperpolarized lithium-6 as a sensor of nanomolar contrast agents. *Magnetic Resonance in Medicine* 61, 1489-1493 (2009).

28. Karlsson, M., Ardenkjær-Larsen, J.H. & Lerche, M.H. Hyperpolarized 133Cs is a sensitive probe for real-time monitoring of biophysical environments. *Chemical Communications* 53, 6625-6628 (2017).

29. Lee, Y., Zeng, H., Ruedisser, S., Gossert, A.D. & Hilty, C. Nuclear magnetic resonance of hyperpolarized fluorine for characterization of protein-ligand interactions. *J Am Chem Soc* 134, 17448-17451 (2012).

30. Nardi-Schreiber, A.*, et al.* Biochemical phosphates observed using hyperpolarized 31P in physiological aqueous solutions. *Nature Communications* 8, 341 (2017).

31. Jindal, A.K.*, et al.* Hyperpolarized 89Y complexes as pH sensitive NMR probes. *J Am Chem Soc* 132, 1784-1785 (2010).

32. Lumata, L.*, et al.* DNP by thermal mixing under optimized conditions yields >60,000-fold enhancement of 89Y NMR signal. *J Am Chem Soc* 133, 8673-8680 (2011).

33. Lumata, L., Merritt Matthew, E., Hashami, Z., Ratnakar, S.J. & Kovacs, Z. Production and NMR Characterization of Hyperpolarized 107,109Ag Complexes. *Angewandte Chemie International Edition* 51, 525-527 (2011).

34. Nonaka, H.*, et al.* A platform for designing hyperpolarized magnetic resonance chemical probes. *Nature Communications* 4, 2411 (2013).

35. Ardenkjær-Larsen, J.H.*, et al.* Increase in signal-to-noise ratio of > 10,000 times in liquid-state NMR. *Proceedings of the National Academy of Sciences* 100, 10158-10163 (2003).

36. Wind, R.A., Duijvestijn, M.J., van der Lugt, C., Manenschijn, A. & Vriend, J. Applications of dynamic nuclear polarization in 13C NMR in solids. *Progress in Nuclear Magnetic Resonance Spectroscopy* 17, 33-67 (1985).

37. Goldman, A.A.a.M. *Nuclear Magnetism: Order and Disorder*, (Clarendon Press, Oxford, U.K., 1982).

38. Slichter, C.P. *Principles of Magnetic Resonance*, (Springer-Verlag, New-York, 1990).

39. Gunther, U.L. Dynamic nuclear hyperpolarization in liquids. *Topics in current chemistry* 335, 23-69 (2013).

40. Overhauser, A.W. Polarization of Nuclei in Metals. *Phys Rev* 91, 476-476 (1953).

41. Carver, T.R. & Slichter, C.P. Polarization of Nuclear Spins in Metals. *Physical Review* 92, 212-213 (1953).

42. Jeffries, C.D. *Dynamic nuclear orientation*, (Interscience Publishers, New York, 1963).

43. Jeffries, C.D. Dynamic Orientation of Nuclei by Forbidden Transitions in Paramagnetic Resonance. *Phys Rev* 117, 1056-1069 (1960).

44. Abragam, A. *The Principles of Nuclear Magnetism. [With plates.]*, (Oxford, Pp. xvi. 599. Clarendon Press, 1961).

45. Abragam A. and Proctor W. G., C.R.H. *Seances Acad. Sci.* 15, 2253–2256 (1958).

46. Atsarkin, V. *Dynamic nuclear polarization: Yesterday, today, and tomorrow*, (2011).

47. Wenckebach, W.T. The solid effect. *Appl Magn Reson* 34, 227-235 (2008).

48. Maly, T.*, et al.* Dynamic nuclear polarization at high magnetic fields. *The Journal of chemical physics* 128, 052211 (2008).

49. Borghini, M. Spin-Temperature Model of Nuclear Dynamic Polarization Using Free Radicals. *Physical Review Letters* 20, 419-421 (1968).

50. Wenckebach, W.T. Dynamic nuclear polarization via thermal mixing: Beyond the high temperature approximation. *Journal of Magnetic Resonance* 277, 68-78 (2017).

51. Farrar, C.T., Hall, D.A., Gerfen, G.J., Inati, S.J. & Griffin, R.G. Mechanism of dynamic nuclear polarization in high magnetic fields. *The Journal of chemical physics* 114, 4922-4933 (2001).

52. J. Gerfen, G.*, et al. High frequency (140 GHz) dynamic nuclear polarization: Polarization transfer to a solute in frozen aqueous solution*, (1995).

53. Rosay, M.*, et al.* High-Frequency Dynamic Nuclear Polarization in MAS Spectra of Membrane and Soluble Proteins. *Journal of the American Chemical Society* 125, 13626-13627 (2003).

54. Weis, V., Bennati, M., Rosay, M., Bryant, J.A. & Griffin, R.G. High-field DNP and ENDOR with a novel multiple-frequency resonance structure. *Journal of magnetic resonance (San Diego, Calif. : 1997)* 140, 293-299 (1999).

55. Sirusi, A.A., Suh, E.H., Kovacs, Z. & Merritt, M.E. The effect of Ho(3+) doping on (13)C dynamic nuclear polarization at 5 T. *Phys Chem Chem Phys* 20, 728-731 (2018).

56. Gordon, J., Fain, S.B. & Rowland, I.J. Effect of Lanthanide Ions on Dynamic Nuclear Polarization Enhancement and Liquid State T(1) Relaxation. *Magnetic resonance in medicine : official journal of the Society of Magnetic Resonance in Medicine / Society of Magnetic Resonance in Medicine* 68, 1949-1954 (2012).

57. Lumata, L.*, et al.* BDPA: an efficient polarizing agent for fast dissolution dynamic nuclear polarization NMR spectroscopy. *Chemistry (Weinheim an der Bergstrasse, Germany)* 17, 10825-10827 (2011).

58. Chaumeil, M.M., Najac, C. & Ronen, S.M. Studies of Metabolism Using (13)C MRS of Hyperpolarized Probes. *Methods Enzymol* 561, 1-71 (2015).

59. Mansson, S.*, et al.* 13C imaging—a new diagnostic platform. *Eur Radiol* 16, 57-67 (2006).

60. Golman, K., in't Zandt, R. & Thaning, M. Real-time metabolic imaging. *Proceedings of the National Academy of Sciences of the United States of America* 103, 11270-11275 (2006).

61. Gallagher, F.A., Kettunen, M.I. & Brindle, K.M. Biomedical applications of hyperpolarized 13C magnetic resonance imaging. *Prog. Nucl. Magn. Reson. Spectrosc.* 55, 285-295 (2009).

62. Brindle, K.M. Imaging metabolism with hyperpolarized 13C-labeled cell substrates. *J Am Chem Soc* 137, 6418-6427 (2015).

63. Lumata, L.*, et al.* Chapter Two - Hyperpolarized 13C magnetic resonance and its use in metabolic assessment of cultured cells and perfused organs. in *Methods in Enzymology*, Vol. 561 (ed. Metallo, C.M.) 73-106 (Academic Press, 2015).

64. Brindle, K.M., Bohndiek, S.E., Gallagher, F.A. & Kettunen, M.I. Tumor imaging using hyperpolarized 13C magnetic resonance spectroscopy. *Magn Reson Med* 66, 505-519 (2011).

65. Cho, A., Lau, J.Y.C., Geraghty, B.J., Cunningham, C.H. & Keshari, K.R. Noninvasive interrogation of cancer metabolism with hyperpolarized 13C MRI. *Journal of nuclear medicine : official publication, Society of Nuclear Medicine* 58, 1201-1206 (2017).

66. Comment, A. & Merritt, M.E. Hyperpolarized magnetic resonance as a sensitive detector of metabolic function. *Biochemistry* 53, 7333-7357 (2014).

67. Mishkovsky, M. & Comment, A. Hyperpolarized MRS: New tool to study real-time brain function and metabolism. *Anal Biochem* 529, 270-277 (2017).

68. Mishkovsky, M.*, et al.* Measuring glucose cerebral metabolism in the healthy mouse using hyperpolarized 13C magnetic resonance. *Scientific reports* 7, 11719 (2017).

69. Niedbalski, P.*, et al.* NMR Spectroscopy Unchained: Attaining the Highest Signal Enhancements in Dissolution Dynamic Nuclear Polarization. *The Journal of Physical Chemistry Letters* 9, 5481-5489 (2018).

70. Bloembergen, N., Purcell, E.M. & Pound, R.V. Relaxation Effects in Nuclear Magnetic Resonance Absorption. *Phys Rev* 73, 679-712 (1948).

71. Patyal, B.R.*, et al.* Longitudinal relaxation and diffusion measurements using magnetic resonance signals from laser-hyperpolarized 129Xe nuclei. *J Magn Reson* 126, 58-65 (1997).

72. Becker Edwin, D. & Shoup, R.R. 13C nmr spectroscopy: relaxation times of 13C and methods for sensitivity enhancement. in *Pure and Applied Chemistry*, Vol. 32 51 (1972).

73. Jensen, P.R., Karlsson, M., Meier, S., Duus, J.Ø. & Lerche, M.H. Hyperpolarized Amino Acids for In Vivo Assays of Transaminase Activity. *Chemistry – A European Journal* 15, 10010-10012 (2009).

74. Morris, G.A. Spin dynamics: Basics of nuclear magnetic resonance, second edition. Malcolm H. Levitt. Wiley Chichester. 2008. ISBN 978-0-470-51118-3(hbk) 978-0-470-51117-6 (pbk). *NMR in biomedicine* 22, 240 (2009).

75. Chiavazza, E., Viale, A., Karlsson, M. & Aime, S. 15N-permethylated amino acids as efficient probes for MRI-DNP applications. *Contrast media & molecular imaging* 8, 417-421 (2013).

76. Penner, G.H., Bernard, G.M., Wasylishen, R.E., Barrett, A. & Curtis, R.D. A solid-state nitrogen-15 NMR and ab initio study of nitrobenzenes. *J Org Chem* 68, 4258-4264 (2003).

77. Hanahan, D. & Weinberg, Robert A. Hallmarks of Cancer: The Next Generation. *Cell* 144, 646-674 (2011).

78. Warburg, O. über den Stoffwechsel der Carcinomzelle. *Klinische Wochenschrift* 4, 534-536 (1925).

79. Cairns, R.A., Harris, I.S. & Mak, T.W. Regulation of cancer cell metabolism. *Nat Rev Cancer* 11, 85-95 (2011).

80. Wallace, D.C. Mitochondria and cancer. *Nat Rev Cancer* 12, 685-698 (2012).

81. Upadhyay, M., Samal, J., Kandpal, M., Singh, O.V. & Vivekanandan, P. The Warburg effect: insights from the past decade. *Pharmacology & therapeutics* 137, 318-330 (2013).

82. Cairns, R.A., Harris, I., McCracken, S. & Mak, T.W. Cancer cell metabolism. *Cold Spring Harbor symposia on quantitative biology* 76, 299-311 (2011).

83. Deberardinis, R.J., Sayed, N., Ditsworth, D. & Thompson, C.B. Brick by brick: metabolism and tumor cell growth. *Current opinion in genetics & development* 18, 54-61 (2008).

84. Kaelin, W.G., Jr. & Thompson, C.B. Q&A: Cancer: clues from cell metabolism. *Nature* 465, 562-564 (2010).

85. Kurhanewicz, J.*, et al.* Analysis of cancer metabolism by imaging hyperpolarized nuclei: prospects for translation to clinical research. *Neoplasia* 13, 81-97 (2011).

86. Hosios, A.M.*, et al.* Amino Acids Rather than Glucose Account for the Majority of Cell Mass in Proliferating Mammalian Cells. *Developmental cell* 36, 540-549 (2016).

87. Mashimo, T.*, et al.* Acetate Is a Bioenergetic Substrate for Human Glioblastoma and Brain Metastases. *Cell* 159, 1603-1614 (2014).

88. Comerford, S.A.*, et al.* Acetate dependence of tumors. *Cell* 159, 1591-1602 (2014).

89. Tonjes, M.*, et al.* BCAT1 promotes cell proliferation through amino acid catabolism in gliomas carrying wild-type IDH1. *Nat Med* 19, 901-908 (2013).

90. Ziegler, S.I. Positron Emission Tomography: Principles, Technology, and Recent Developments. *Nuclear Physics A* 752, 679-687 (2005).

91. Meier, S., Jensen, P.R., Karlsson, M. & Lerche, M.H. Hyperpolarized NMR probes for biological assays. *Sensors (Basel, Switzerland)* 14, 1576-1597 (2014).

92. Doura, T., Hata, R., Nonaka, H., Ichikawa, K. & Sando, S. Design of a 13C magnetic resonance probe using a deuterated methoxy group as a long-lived hyperpolarization unit. *Angew Chem Int Ed Engl* 51, 10114-10117 (2012).

93. Nishihara, T., Nonaka, H., Naganuma, T., Ichikawa, K. & Sando, S. Mouse lactate dehydrogenase X: A promising magnetic resonance reporter protein using hyperpolarized pyruvic acid derivative Y. *Chemical Science* 3, 800-806 (2012).

94. Hurd Ralph, E.*, et al.* Metabolic imaging in the anesthetized rat brain using hyperpolarized [1-13C] pyruvate and [1-13C] ethyl pyruvate. *Magnetic Resonance in Medicine* 63, 1137-1143 (2010).

95. Zacharias, N.M., Chan, H.R., Sailasuta, N., Ross, B.D. & Bhattacharya, P. Real-time molecular imaging of tricarboxylic acid cycle metabolism in vivo by hyperpolarized 1-(13)C diethyl succinate. *J Am Chem Soc* 134, 934-943 (2012).

96. Colombo Serra, S.*, et al.* Hyperpolarized (13) C-labelled anhydrides as DNP precursors of metabolic MRI agents. *Contrast media & molecular imaging* 7, 469-477 (2012).

97. Harris, T., Eliyahu, G., Frydman, L. & Degani, H. Kinetics of hyperpolarized 13C1-pyruvate transport and metabolism in living human breast cancer cells. *Proceedings of*

the National Academy of Sciences of the United States of America 106, 18131-18136 (2009).

98. Keshari, K.R.*, et al.* Hyperpolarized (13)C spectroscopy and an NMR-compatible bioreactor system for the investigation of real-time cellular metabolism. *Magn Reson Med* 63, 322-329 (2010).

99. Meier, S., Jensen, P.R. & Duus, J.O. Real-time detection of central carbon metabolism in living Escherichia coli and its response to perturbations. *FEBS Lett* 585, 3133-3138 (2011).

100. Rodrigues, T.B.*, et al.* Magnetic resonance imaging of tumor glycolysis using hyperpolarized 13C-labeled glucose. *Nat Med* 20, 93-97 (2014).

101. Gallagher, F.A.*, et al.* Magnetic resonance imaging of pH in vivo using hyperpolarized 13C-labelled bicarbonate. *Nature* 453, 940-943 (2008).

102. Düwel, S.*, et al.* Imaging of pH in vivo using hyperpolarized 13C-labelled zymonic acid. *Nature Communications* 8, 15126 (2017).

103. Flavell, R.R.*, et al.* Application of Good's buffers to pH imaging using hyperpolarized (13)C MRI. *Chemical communications (Cambridge, England)* 51, 14119-14122 (2015).

104. Bohndiek, S.E.*, et al.* Hyperpolarized [1-13C]-ascorbic and dehydroascorbic acid: vitamin C as a probe for imaging redox status in vivo. *J Am Chem Soc* 133, 11795-11801 (2011).

105. Keshari, K.R.*, et al.* Hyperpolarized 13C dehydroascorbate as an endogenous redox sensor for in vivo metabolic imaging. *Proceedings of the National Academy of Sciences of the United States of America* 108, 18606-18611 (2011).

106. Keshari, K.R.*, et al.* Noninvasive in vivo imaging of diabetes-induced renal oxidative stress and response to therapy using hyperpolarized 13C dehydroascorbate magnetic resonance. *Diabetes* 64, 344-352 (2015).

107. Lippert, A.R., Keshari, K.R., Kurhanewicz, J. & Chang, C.J. A hydrogen peroxide-responsive hyperpolarized 13C MRI contrast agent. *J Am Chem Soc* 133, 3776-3779 (2011).

108. Mishra, A., Pariani, G., Oerther, T., Schwaiger, M. & Westmeyer, G.G. Hyperpolarized Multi-Metal 13C-Sensors for Magnetic Resonance Imaging. *Analytical Chemistry* 88, 10790-10794 (2016).

109. Nonaka, H.*, et al.* A platform for designing hyperpolarized magnetic resonance chemical probes. *Nat Commun* 4(2013).

110. Lee, Y.*, et al.* Hyperpolarized binding pocket nuclear Overhauser effect for determination of competitive ligand binding. *Angew Chem Int Ed Engl* 51, 5179-5182 (2012).

111. Lerche, M.H.*, et al.* Study of molecular interactions with 13C DNP-NMR. *Journal of magnetic resonance (San Diego, Calif. : 1997)* 203, 52-56 (2010).

112. Lerche, M.H.*, et al.* Quantitative dynamic nuclear polarization-NMR on blood plasma for assays of drug metabolism. *NMR in biomedicine* 24, 96-103 (2011).

113. Ardenkjaer-Larsen Jan, H.*, et al.* Dynamic nuclear polarization polarizer for sterile use intent. *NMR in biomedicine* 24, 927-932 (2011).

114. Eul Hyun Suh, W.O., Ian Corbin, A. Dean Sherry, Jae Mo Park. Imaging branched-chain amino acid metabolism in glioma using hyperpolarized [1-13C] -ketoisocaproate. *Proc. Intl. Soc. Mag. Reson. Med* 25, #3604 (2017).

115. Harrison, C.*, et al.* Comparison of kinetic models for analysis of pyruvate-to-lactate exchange by hyperpolarized 13C NMR. *NMR in biomedicine* 25, 1286-1294 (2012).

116. Witney, T.H., Kettunen, M.I. & Brindle, K.M. Kinetic modeling of hyperpolarized 13C label exchange between pyruvate and lactate in tumor cells. *The Journal of biological chemistry* 286, 24572-24580 (2011).

117. Yang, C.*, et al.* Simultaneous steady-state and dynamic 13C NMR can differentiate alternative routes of pyruvate metabolism in living cancer cells. *The Journal of biological chemistry* 289, 6212-6224 (2014).

118. Schroeder, M.A.*, et al.* Real-time assessment of Krebs cycle metabolism using hyperpolarized 13C magnetic resonance spectroscopy. 23, 2529-2538 (2009).

119. Nelson, S.J.*, et al.* Metabolic Imaging of Patients with Prostate Cancer Using Hyperpolarized [1-¹³C]Pyruvate. *Science Translational Medicine* 5, 198ra108 (2013).

120. Cunningham, C.H.*, et al.* Hyperpolarized 13C Metabolic MRI of the Human Heart: Initial Experience. *Circulation research* 119, 1177-1182 (2016).

121. Merritt, M.E.*, et al.* Hyperpolarized 13C allows a direct measure of flux through a single enzyme-catalyzed step by NMR. *Proc Natl Acad Sci U S A* 104, 19773-19777 (2007).

122. Keshari, K.R., Kurhanewicz, J., Macdonald, J.M. & Wilson, D.M. Generating contrast in hyperpolarized 13C MRI using ligand-receptor interactions. *The Analyst* 137, 3427-3429 (2012).

123. Wilson, D.M.*, et al.* Generation of hyperpolarized substrates by secondary labeling with [1,1-13C] acetic anhydride. *Proceedings of the National Academy of Sciences of the United States of America* 106, 5503-5507 (2009).

124. Shanaiah, N.*, et al.* Class selection of amino acid metabolites in body fluids using chemical derivatization and their enhanced 13C NMR. *Proceedings of the National Academy of Sciences of the United States of America* 104, 11540-11544 (2007).

125. Comment, A. & Merritt, M.E. Hyperpolarized magnetic resonance as a sensitive detector of metabolic function. *Biochemistry* 53, 7333-7357 (2014).

Chapter 2

Hyperpolarized ^{15}N tripodal tetramine derivatives as MRI sensors of free Zn^{2+}

2.1 Introduction

Zn^{2+} plays an important role in various biochemical processes such as enzyme catalytic activity, neurotransmission, intracellular signaling, and antibiotic activity. Cellular Zn^{2+} homeostasis is related to the onset and progression of several diseases including diabetes and cancer.[1] For example, Zn^{2+} is essential for insulin production, storage, and secretion by pancreatic β-cells. In the brain, Zn^{2+} is involved in glutamate release from presynaptic vesicles *via* calcium-dependent exocytosis; an alteration in zinc homeostasis may also play a role in the development of various neurodegenerative disorders. In another example, the amount of total Zn^{2+} in prostate tissue decreases significantly during the early stages of malignancy.[2-4] Healthy prostate cells store and secrete large amounts of Zn^{2+} while malignant prostate cells have reduced levels of Zn^{2+}.[2] Indeed, in prostate cancer (PCa), there is a remarkable decrease in Zn^{2+} levels in malignant prostate tissue compared to normal prostate.[5] The current accepted clinical biomarker of PCa is based on a prostate-specific antigen (PSA) blood test but needs verification by other biomarkers such as prostate health index (Phi), prostate cancer antigen 3 (PCA3), and eventually by biopsy.[6] Prostate tissue biopsies are painful and have a chance of missing cancerous cell growth in a small area tissue collection. Previous studies have shown that Zn^{2+} levels in prostate tissue significantly decrease in the early stages of malignancy.[2] The Zn^{2+} content in normal prostate is 3,000 ~ 4,500 nmol/g wet tissue weight of epithelial tissue but it reduces to ~400 ~ 800 nmol/ g wet tissue

weight of epithelial tissue with the development of malignancy (Table 1.1).[3] For this reason, detecting a decrease in prostate Zn^{2+} levels may prove useful for early diagnosis of malignant prostate cancer.[4] Therefore, noninvasive real time *in vivo* detection of Zn^{2+} homeostasis could become an important diagnostic biomarker for prostate cancer and perhaps a variety of other diseases.

(NMOLS/GRAM WWT)	CITRATE	ZINC
NORM PERIPH ZONE	12,000–14,000	3,000–4,500
MALIG PERIPH ZONE	200–2000	400–800
OTHER TISSUES	250–450	200–400
NORM PROS FLUID	40,000–150,000	8,000–10,000
PCA PROS FLUID	500–3000	800–2000
BLOOD PLASMA	100–200	15

Table 2.1 Representative citrate and Zn^{2+} levels in various tissues and fluids, reproduced with permission from reference [3]

However, *in vivo* Zn^{2+} detection remains a major challenge because of the lack of non-invasive imaging. There are limited numbers of non-invasive techniques for *in vivo* Zn^{2+} detection. Optical imaging and magnetic resonance imaging (MRI) have a potential for real time Zn^{2+} *in vivo* detection without involving ionizing radiation. However, limited penetration depth due to attenuation and light scattering in tissues is a major obstacle in optical imaging.[7] A recent study demonstrated that MRI can successfully monitor Zn^{2+} secretion into extracellular space in malignant prostrate lesions using a gadolinium-based contrast agent.[8] Although several Zn^{2+} specific Gd-based MR contrast agents have been reported, these are limited to the extracellular space by their cellular impermeability. In addition, the detection limit of a typical Gd-based MRI

contrast agent is restricted to the 50 ~ 100 μM range by the intrinsic low sensitivity of conventional MRI methods, depending on the relaxivity of the MR agent.[1]

Dissolution DNP-NMR can overcome the low sensitivity problem of conventional MRI. Dynamic nuclear polarization (DNP) refers to technologies that enhance the NMR signal-to-noise ratio by amplifying nuclear spin polarization.[9] However, the lifetime of the hyperpolarized spin state is limited since hyperpolarized magnetization returns to thermal equilibrium by spin-lattice relaxation (T_1). DNP polarization is feasible for several nuclei including ^{13}C and ^{15}N, both of which have much lower NMR sensitivity compared to ^{1}H. Hyperpolarized (HP) ^{15}N is particularly attractive for DNP because the spin ½ ^{15}N nucleus in most molecules tends to have longer T_1 and wider chemical shift range than ^{13}C. In this study, cell permeable ^{15}N-labeled tripodal ligands were investigated as hyperpolarized ^{15}N MR sensors of Zn^{2+}, with the aim of detecting biologically relevant free Zn^{2+} in both intracellular and extracellular spaces.

There are several reports of HP-NMR based biological metal sensors such as ^{13}C-EDTAs as hyperpolarized multi-metal sensor and ^{129}Xe NMR based Zn^{2+} sensor. However, they have some limitations such as significant line broadening of the ligand ^{13}C signals after binding to Zn^{2+} and the lack of sufficient chemical shift difference between Zn^{2+} and Mg^{2+} or Ca^{2+} complexes.[10] The hyperpolarized ^{129}Xe NMR based Zn^{2+}sensors work by continuous xenon exchange between free ^{129}Xe and ^{129}Xe bound to the cryptophane host conjugated to a Zn sensing moiety. However, this system also shows only 1.7ppm ^{129}Xe chemical shift difference in the presence and absence of Zn^{2+} ions.[11]

2.2 Materials and Methods

2.2.1 Chemicals and reagents

All reagents were analytic grade and were purchased from Sigma Aldrich, then used without further purification. HSA (essentially fatty acid free and globulin-free) was used for the isothermal titration calorimetry to determine dissociation constant. A stock solution of HSA, which used for hyperpolarization binding study (stock # P9523 from Aldrich), was prepared HEPES buffer and the concentration was determined by ultraviolet absorption at 291nm (extinction coefficient of 39310 $M^{-1}cm^{-1}$, molecular weight of 66.4 KDa).

2.2.2 Synthesis of TPA derivatives

2.2.2.1 Synthesis of [^{15}N]TPA : *^{15}N-tris(2-pyridylmethyl)amine*

^{15}N-phthalimide (1)

^{15}N-ammonium acetate (506.1mg, 6.5mmol) was mixed with phthalic anhydride (800mg, 5.4mmol) and stirred for 4hr at 160°C. After the reaction mixture cooled to room temperature, the white solid was washed with cold water, filtered, and dried in vacuum to afford ^{15}N-phthalimide as white powder (0.73 g, 91%)

^{15}N-(pyridine-2-ylmethyl)phthalimide (2)

^{15}N-phthalimide (645mg, 4.3mmol) was dissolved in dimethylformamide (10 mL) and potassium carbonate (1.5g, 10.9mmol) and 2-(chloromethyl)pyridine (749mg, 4.6mmol) were added. The reaction mixture was stirred for 12hr at 50°C. After removal of the solvent, water was added to

precipitate the product and to remove inorganic salts. The crude product was filtered and dried in vacuum to afford ^{15}N-(pyridine-2-ylmethyl)phthalimide as a white solid (1.03g, yield 98%).

^{15}N-2-aminomethyl pyridine (3)

^{15}N-(pyridine-2-ylmethyl)phthalimide (850mg, 3.6mmol) was dissolved in 10% hydrochloric acid (30mL) and the solution was stirred for 12hr at 80°C. The hydrochloric acid was removed by rotary evaporation and the residue was dissolved in 20% sodium hydroxide (5mL) and extracted with dichloromethane (50mL). The organic layer was dried over anhydrous sodium sulfate, filtered, and concentrated by rotary evaporation. The residue was dried in vacuum to afford^{15}N-2-aminomethyl pyridine as a yellowish oil (349.25mg, yield 89%).

^{15}N-tris(2-pyridylmethyl)amine (4)

^{15}N-2-aminomethyl pyridine (348mg, 3.2mmol) was dissolved in acetonitrile (15mL) and potassium carbonate (1.8g, 12.8mmol) and 2-(chloromethyl)pyridine (1.1g, 6.4mmol) were added. The reaction mixture was stirred for 12hr at ambient temperature. After filtration of solvent, the crude product was dissolved in dichloromethane and filtrated to remove potassium carbonate. The organic layer was dried over anhydrous sodium sulfate, filtered, and dried in vacuum. The oily residue was purified by column chromatography in 97:3 dichloromethane : methanol solvent system and recrystallization from ethyl ether/hexane to afforded ^{15}N-tris(2-pyridylmethyl)amine as light yellowish solid (291.15mg, yield 31%)

2.2.2.2 Synthesis of [^{15}N]TPAd$_6$: ^{15}N labeled *tris(2-pyridylmethyl-d$_2$)amine*

Pyridine-2-ylmethan-d$_2$-ol (5)

Sodium borodeuteride (4.2g, 99.2mmol) was added slowly to a deuterated methanol solution (18mL) of ethyl picolinate (5g, 33.1mmol) at 0°C over 40min. The reaction mixture was stirred for 12hr at ambient temperature. After removal of solvent, the residue was stirred with saturated potassium carbonate solution (100mL) for 1hr and then extracted with chloroform. The organic layer was dried over anhydrous sodium sulfate, filtered, and dried in vacuum to afford the product as white solid (3.22g, yield 88%)

2-(chloromethyl-d_2) pyridine (6)

2-(chloromethyl-d_2) pyridine was prepared as previously described.[12] In brief, pyridine-2-ylmethan-d_2-ol (3.2g, 28.0mmol) was added dropwise to a solution of thionyl chloride (16.7g, 140.2mmol) in dichloromethane (20mL) in an ice bath. The reaction mixture was refluxed for 3hr and then stirred at room temperature for 12 hours. The product was precipitated by adding ethyl ether (20 mL). The precipitation was filtered and dried in vacuum to afford 2-(chloromethyl-d_2) pyridine as yellowish powder (3.56g, yield 98.5%).

^{15}N-(pyridine-2-ylmethyl-d_2)phthalimide (7)

^{15}N-(pyridine-2-ylmethyl-d_2)phthalimide was synthesized from 2-(chloromethyl-d_2) pyridine (1.8g, 11.1mmol) as described for ^{15}N-(pyridine-2-ylmethyl)phthalimide. ^{15}N-phthalimide (1.5g, 10.1mmol) was dissolved in dimethylformamide (18mL) and potassium carbonate (3.5g, 25.3mmol) and 2-(chloromethyl-d_2) pyridine (1.8g, 11.1mmol) was added and the reaction mixture was stirred for 12hr at 50°C. After removal of solvent, water was added to the crude

product to remove the inorganic salts. The precipitated product was filtered and dried in vacuum to afford ^{15}N-(pyridine-2-ylmethyl-d_2)phthalimide as white powder (2.39g, yield 98%).

^{15}N-2-(aminomethyl-d_2)pyridine (8)

This intermediate was synthesized from ^{15}N-(pyridine-2-ylmethyl-d_2)phthalimide (2.2g, 9.3mmol) as described for ^{15}N-2-aminomethyl. A solution of ^{15}N-(pyridine-2-ylmethyl-d_2)phthalimide (2.2g, 9.3mmol) in 10% hydrochloride (45mL) was stirred for 12hr at 80°C. After removal of the hydrochloric acid, the residue was dissolved in 20% sodium hydroxide (13mL) and extracted with dichloromethane. The organic layer was dried with anhydrous sodium sulfate, filtered, and dried in vacuum to afford ^{15}N-2-(aminomethyl-d_2)pyridine as a pale yellow oil (877.53mg, yield 85%).

^{15}N-tris(2-pyridylmethyl-d_2)amine (9)

^{15}N-2-(aminomethyl-d_2)pyridine (535mg, 4.9mmol) was dissolved in acetonitrile (15mL) and potassium carbonate (2.7g, 19.6mmol) and 2-(chloromethyl-d_2) pyridine (1.6g, 9.8mmol) were added. The reaction mixture was stirred for 12hr at 50°C. The inorganic salts were removed by filtration and the organic layer was dried in vacuum, then dissolved in ethyl acetate and heated. After filtering to remove insoluble impurities, the organic layer was dried over anhydrous sodium sulfate, filtered, and dried in vacuum. The oily residue was purified by recrystallization in ethyl ether to afford ^{15}N-tris(2-pyridylmethyl-d_2)amine as a light yellowish solid (920.76mg, yield 81%)

2.2.2.3 Synthesis of [^{15}N]BP: ^{15}N-Benzyl-1-(pyridine-2-yl)-N-(pyridine-ylmethyl)methanamine

^{15}N-Benzylphthalimide (10)

Benzyl bromide (1.01 g, 5.93 mmols) was added dropwise to a mixture of ^{15}N-phthalimide (1.00 g, 5.39 mmols) and potassium carbonate (1.50 g, 10.78 mmols) in 10 mL of dimethylformamide and heated with stirring to 80 ^{o}C over 3 days. The reaction was then cooled to room temperature and 100 mL of cold water was added to crash out the product in the form of a white solid. The solid was filtered, washed with cold water, and dried. (1.11g, 86.44% yield).

^{15}N-Benzylamine (11)

Anhydrous hydrazine (202.00 mg, 6.29 mmols) was added dropwise to a solution of ^{15}N-benzylphthalimide (1.00g, 4.19 mmols) in 12 mL of methanol and heated to 70 ^{o}C overnight under vigorous stirring. The reaction was then cooled to room temperature, filtered, and the filtrate was dried in vacuo. The resulting product was washed with 40 mL 2N sodium hydroxide and extracted in 200 mL dichloromethane. The organic layer was dried over anhydrous sodium sulfate and the dichloromethane was evaporated. The reaction yielded a colorless oil (315mg, 69.51% yield).

^{15}N-Benzyl-1-(pyridine-2-yl)-N-(pyridine-2-ylmethyl)methanamine (12)

A mixture of ^{15}N-benzylamine (315 mg, 2.94 mmols), 2-chloromethyl pyridine hydrochloride (966 mg, 5.88 mmols), and potassium carbonate (1.62g, 11.76 mmols) in 15 mL of acetonitrile was heated to 50 ^{o}C under vigorous stirring for 5 days. The reaction mixture was then cooled to room temperature, filtered, and the solvent was evaporated, yielding 724 mg of crude product. This was then further purified via column chromatography using silica with a solvent system of

90% ethyl acetate and 10% hexane. This yielded the purified product as oil (389mg, 45.57 % yield).

2.2.3 Determination of the TPA binding constant with HSA by isothermal titration calorimetry (ITC).

ITC experiments were performed to measure the binding constant for TSA binding to HSA using a MicroCal ITC 200. All samples were prepared in 100mM HEPES buffer, pH 7.4. HSA was dialyzed in a buffer solution and degassed prior to the experiment using FlatLyser with a molecular weight cut-off 20 kDa. The samples were placed in the instrument for thermal equilibrium at 25°C. TPA was titrated with 18 successive 2μL injection and time interval of 125s between each injection into the cell containing 300μL HAS. The measurement was performed at the biophysics core facility at UT Southwestern Medical Center.

2.2.4 Determination of the dissociation constant of TPA-Zn complexes

The dissociation constants (K_D) of the TPA ligands were determined by competitive binding assays using the fluorophore ZnAF-2F in 100 mM HEPES buffer (pH 7.4) at 25 °C. A solution containing 1 μM ZnAF-2F, 0.05 μM $ZnSO_4$ and 100 μM TPA or BP in buffer was prepared. Aliquots of this solution were serially diluted 2-fold by addition of a buffered solution which contained the same concentration of ZnAF-2F and $ZnSO_4$ without TPA. This gave twelve samples of different concentrations of TPA but all samples contained the same concentration of ZnAF-2F and $ZnSO_4$. The fluorescence of 100 μL aliquots of each of these samples was measured in triplicate in COSTAR 96 well plates. In order to account for the background

correction from the agent interacting with Zn^{2+}, $ZnSO_4$ without ZnAF-2F were prepared in a same manner and fluorescence were measured by triplicate (The excitation and emission wavelengths used were 492 and 520 nm with Gain 1000 with positioning delay 0.2s at 25°C, respectively. The fluorescence intensity data (Figure 2.1) were fitted to the following equations, and K_D was calculated by GraphPad Prism Software Version 7, Competition Binding equations of *One site - Fit Ki* (Graph Pad Software Inc.).

$$F = F_{min} + (F_{max} - F_{min})/(1 + 10\text{^}(X - \log IC_{50})) \quad (2.1)$$

$$\log IC_{50} = \log(10 \log K_D) * (1 + \text{ligand (nM)}/\text{Hot}K_D \text{ (nM)}) \quad (2.2)$$

F is the measured and background corrected fluorescence.

F_{max} and F_{min} are plateaus in the units of Y axis (fluoresce intensity): F_{max} is the maximal fluorescence in absence of competitors (TPAs ligands) and $F_{min}$is the minimal fluorescence observed in the competition binding experiment. Ligand (nM) is the concentration of ZnAF-2F in nM. A single concentration of ZnAF-2F (1 μM) is used for the entire experiment. HotK_D (nM) is the equilibrium dissociation constant of the ZnAF-2F (K_D = 5.5 nM for ZnAF-2F). IC_{50} corresponds to the concentration of competitor where the binding is reduced by half and decrease 50% of F_{max}. K_D is the dissociation constant in Molar.

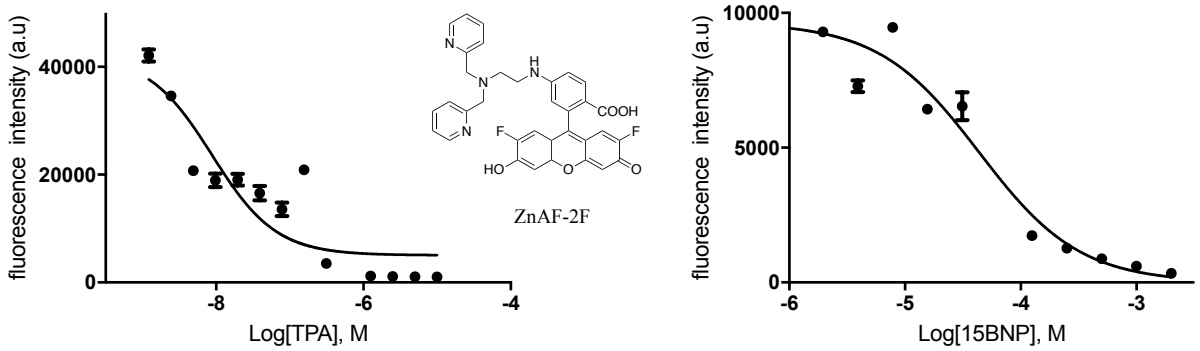

Figure 2.1 Competition binding curve for determination of Zn^{2+} binding dissociation constant using ZnAF-2F

2.2.5 General method for ^{15}N hyperpolarization

The synthesized TPAs were dissolved at a concentration of 640mM in glycerol and water (50:50 w/w) containing 2mM Gd (ProHance®) and 15mM trityl radical (OX063, GE-healthcare, UK). 50uL samples were polarized using a HyperSense polarizer (3.35 Tesla, Oxford Instruments Molecular Biotools, UK). The polarization was performed at 1.05K with 94.112 GHz microwave irradiation for 2hr and subsequently rapidly dissolved in a phosphate buffered solution (10mM PO_4^{3-}, 1mM Na_2EDTA, pH~7.4) or HEPES buffered solution to yield 8mM hyperpolarized solution in a 10-mm NMR tube. DNP experiment with unlabeled TPA was performed in the general HP condition and dissolved in water to yield 35mM final concentration. ^{15}N-NMR spectra were acquired on a 9.4 T spectrometer on a 9.4T Agilent vertical bore microimager (Agilent, USA) using 5-degree flip angle with repetition time (TR) of 2 sec. All ^{15}N chemical shifts are externally referenced to ^{15}N-ammonium ion (0 ppm). The ^{15}N spectra were processed using ACD/SpecManager (ACD Labs, Canada). Hyperpolarization signal enhancement and T_1 decay were calculated from Equation 1.17 and 1.18 as discussed in Chapter 1. The binding

stoichiometry experiment was performed using thermal ^{15}N NMR spectrometer (90-degree flip angle with repetition time (TR) of 250 sec.

2.2.6 ^{15}N CSI imaging

TPAd_6 phantom imaging was performed on a 9.4T Agilent vertical bore microimager (Agilent, USA). The phantom consisted of three of 8-mm NMR tubes inserted into a 22mm NMR tube containing DI water (8~10mL). 1mL of different Zn^{2+} concentrations were added to the three 8mm NMR tubes. The axial imaging plane was positioned near the phantom center. The acquisition of ^{15}N CSI imaging started 10s after the hyperpolarized sample transfer was completed. CSI parameter: CSI2 sequence (Agilent VnmrJ 4 Imaging, USA), field of view (FOV) = 40 x 40 mm; TR = 200 ms; TE = 1.30ms; Flip angle = 30 °; NA=1, matrix = 16X16. The ^{15}N CSI imaging data were reconstructed and analyzed using MATLAB (Mathworks, Natick MA, USA).

2.3 Results and Discussion

2.3.1 Design of ^{15}N-Zn^{2+} sensors for hyperpolarization

There are important criteria to be considered for the design of hyperpolarized ^{15}N Zn^{2+} sensors including: 1) selectivity for Zn^{2+}, 2) long ^{15}N spin-lattice relaxation times (T_1) with high levels of polarization to allow *in vivo* observation, 3) appropriate conditional dissociation constant (K_d) for the range of Zn^{2+} concentrations to be detected,[13] 4) fast complexation with Zn^{2+} to allow rapid detection, 5) appropriate chemical shift change upon Zn^{2+}-binding, and 6) proper cell membrane permeability to detect total tissue Zn^{2+}. Based on these considerations, we designed

^{15}N-enriched tripodal ligands and derivatives with different K_d values and T_1 that can potentially report *in vivo* "free" Zn-level to function as hyperpolarized ^{15}N MR Zn-sensors (Figure 2.2). Here, tris(2-pyridylmethyl)amine (TPA) is proposed as a design platform for hyperpolarized ^{15}N MR Zn-sensors.

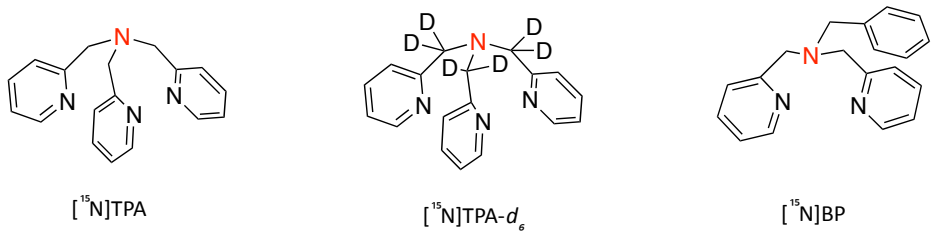

Figure 2.2 Structure of ^{15}N-labeled tripodal derivatives

Since Zn^{2+} is a "soft-to-intermediate" ion in terms of the hard soft acid-base theory, it forms stable complexes with ligands containing 3 to 6 N, O or S donor atoms. For this reason, tripodal ligands with N-donors in which the three coordinating side-arms are attached to a central atom are the most popular platform for Zn-sensors. These complexes have high stability and selectivity toward Zn^{2+} over most endogenous divalent biometals except for Cu^{2+}. However, the in vivo concentration of Cu^{2+} is much lower than that of Zn^{2+}; in addition, the ^{15}N signal of TPA-Cu complex will not be observed due to the fast relaxation caused by the paramagnetism of Cu^{2+}[14,15]. TPA is cell-permeable and will likely distribute across cell membranes at physiological pH (~7.4)[16] and can detect both intracellular and extracellular Zn^{2+}. Once it binds to intracellular Zn^{2+}, the TPA-Zn complex is positively charged and should be trapped in the intracellular compartment. For quantitative determination of Zn^{2+}, the dissociation constant of the sensor for Zn^{2+} should match the target concentration range of free Zn^{2+} in the tissue of interest, typically in the micromolar to nanomolar range.

2.3.2 Preliminary hyperpolarization studies using natural abundance TPA

To evaluate the prototype Zn-sensing ligand, tris(2-pyridylmethyl)amine (TPA) as a potential hyperpolarized ^{15}N-Zn^{2+} sensor, we performed hyperpolarized MR experiments with unlabeled TPA. There are two different types of nitrogen atoms in TPA; namely, the N-atoms in pyridine and the central *tert*-N-atom. Our preliminary data showed that there is a substantial chemical shift in both the N-atom of pyridine (50pm upfield) and the central *tert*-N-atom (20ppm upfield) upon Zn^{2+} binding (Figure 2.3). The hyperpolarized natural abundance of ^{15}N signal in pyridine (288.6 ppm) decayed more rapidly due to a strong chemical shift anisotropy than in *tert*-N-atom (δ_{15N} = 40.2 ppm).

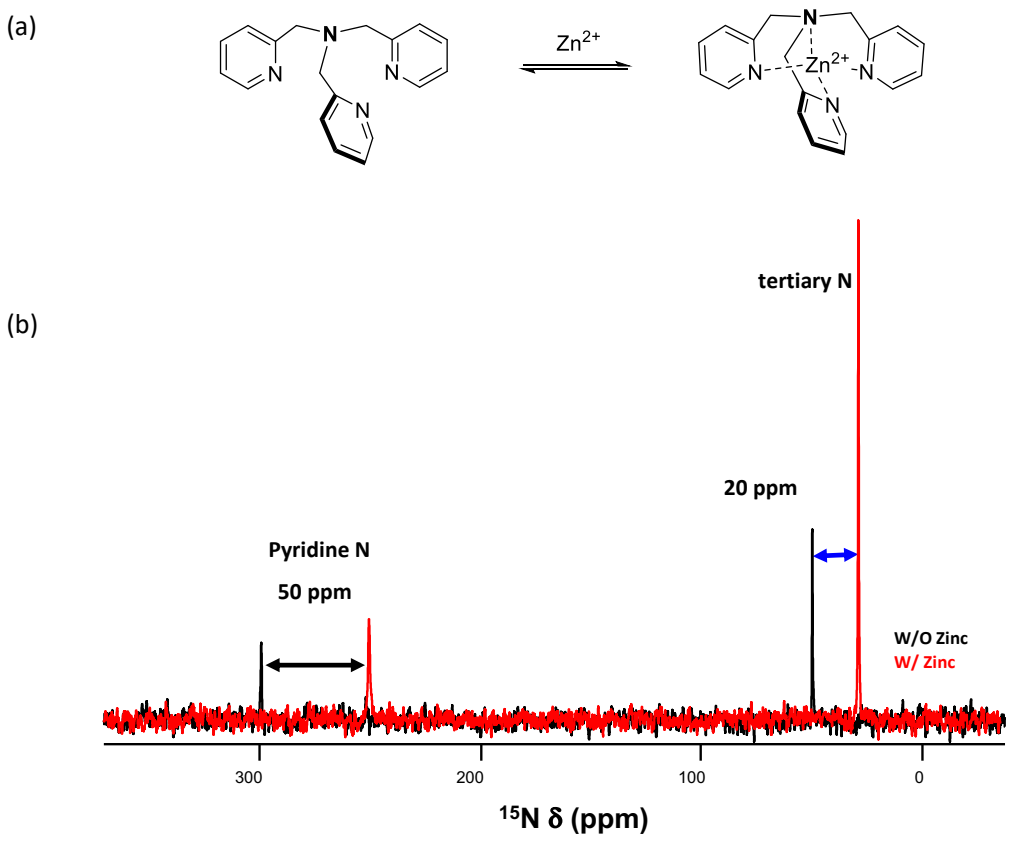

Figure 2.3 DNP MR experiments of hyperpolarized unlabeled TPA. (a) scheme for Zn sensing of TPA (b) the first ^{15}N spectrum of hyperpolarized unlabeled TPA in the absence (spectrum in black) and presence of 40mM Zn^{2+} (spectrum in red).

2.3.3 Synthesis of hyperpolarized ^{15}N labeled TPA

The labeling position at the central *tert*-N-atom was chosen because this N-atom had higher hyperpolarized ^{15}N signal than the pyridine N-atoms presumably due to its longer T_1 (Figure 2.3). ^{15}N labeled version of TPA was synthesized starting from $^{15}NH_4Cl$ and 2-chloromethyl pyridine or 1-(chloromethyl-d_2) pyridine using standard organic reactions as outlined in Scheme 2.1. ^{15}N BP was also synthesized using a similar synthetic approach.

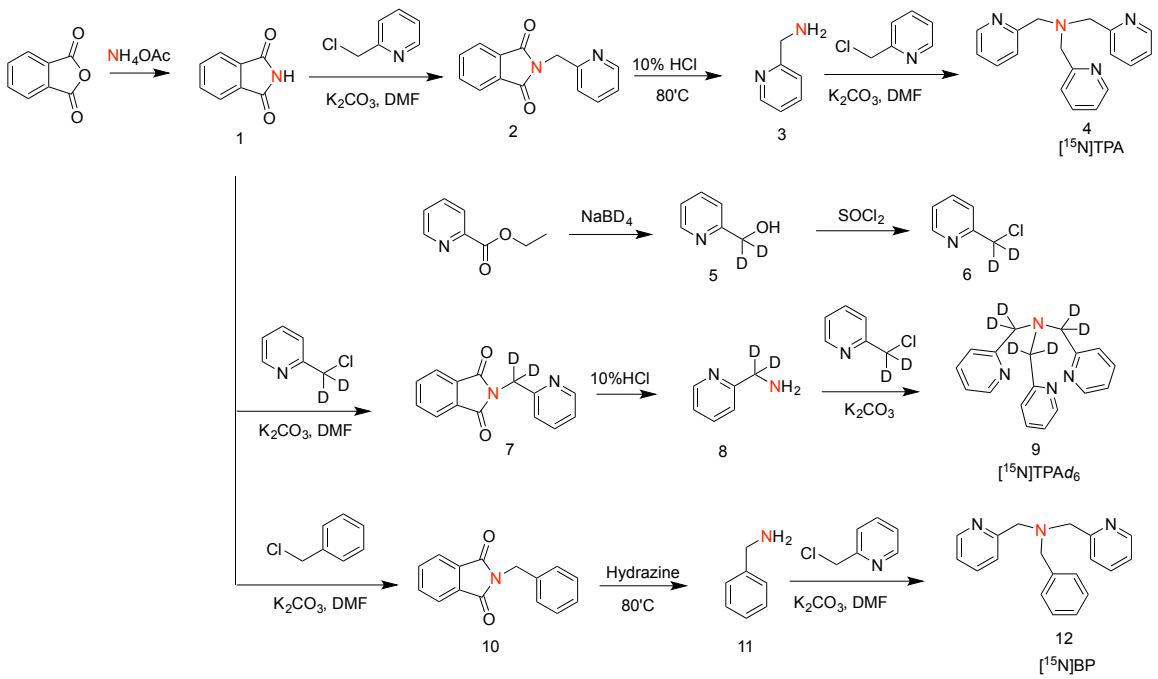

Scheme 2.1 Synthesis of ^{15}N-labeled tripodal derivatives

2.3.4 Hyperpolarization studies with ^{15}N labeled TPA and BP as Zn^{2+} sensor

The ^{15}N labeled TPA and BP were hyperpolarized under standard DNP conditions using HyperSense with trityl OX063 as the polarizing agent. It achieved 27,500-fold signal enhancement for TPA. A spin-lattice relaxation time (T_1) of ^{15}N labeled tertiary amine was calculated to be 27s at 25°C and 9.4T by fitting the decay of hyperpolarized NMR signal to equation 2.3 (Figure 2.4.e).[17,18] In accordance with natural-abundance hyperpolarization ^{15}N experiments, chelation experiments with hyperpolarized ^{15}N-TPA and Zn^{2+} ions revealed that the ^{15}N NMR signal of ^{15}N-TPA shifted 20 ppm upfield upon complexation (Figure 2.4.c and d). In the presence of free Zn^{2+} ions, the four nitrogen donor atoms of TPA coordinate to Zn^{2+}, which causes a change in the ^{15}N chemical shift of the nitrogen atoms. Significant upfield shift (20 ppm) in the ^{15}N resonance of the central ^{15}N atom was observed upon binding to Zn^{2+}. This indicated

that Zn^{2+} exchange between free ligand and TPA-Zn^{2+} complex is slow on the experimental NMR timescale. The spin lattice relaxation time (T_1) was determined by following the decay of hyperpolarized magnetization over time by applying a small flip angle pulse. The T_1 value can be calculated using Equation 2.3.

$$I(t) = I_0 \sin\theta \, (\cos\theta)^{t/TR} exp^{-t/T_1} \tag{2.3}$$

Where, *I(t)* is the signal intensity at time t, I_0 is the initial magnetization, TR is repetition time, and θ is the flip angle of rf pulse used to monitor the hyperpolarization signal.

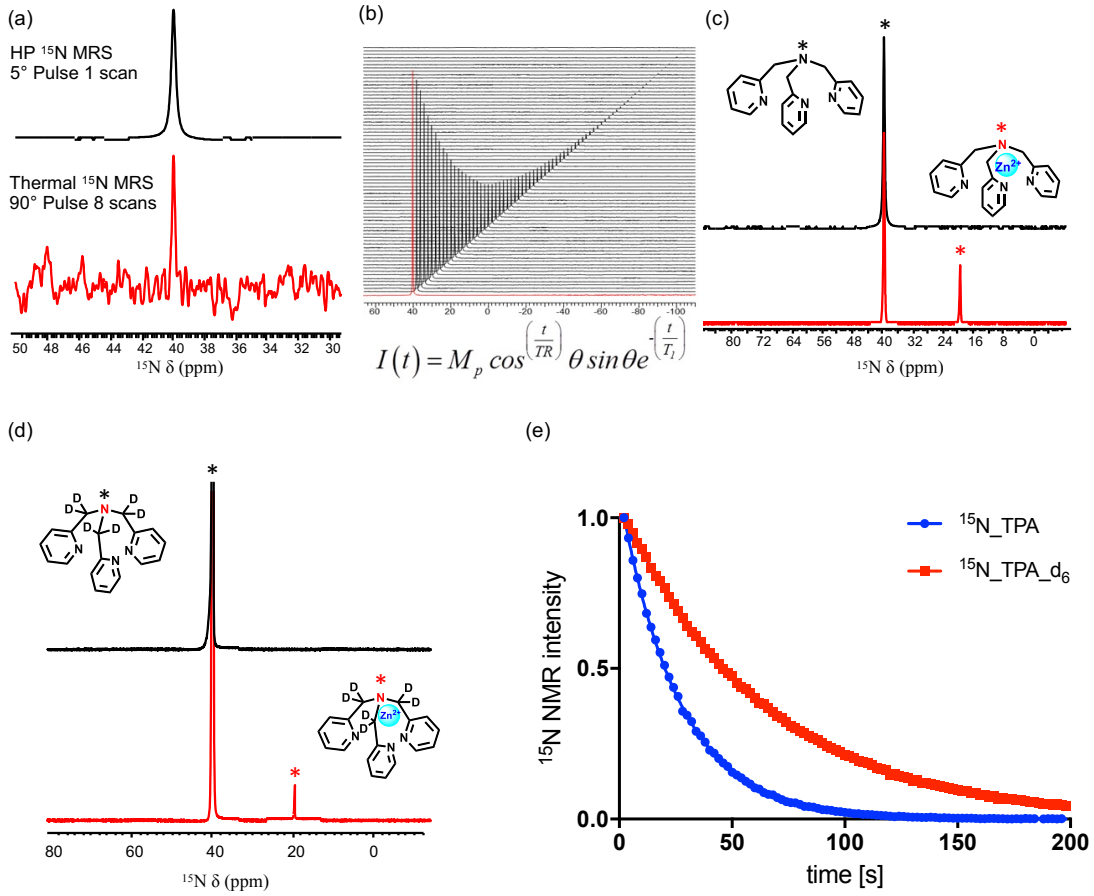

Figure 2.4 DNP-^{15}N MR experiments of ^{15}N-TPA. (a) ^{15}N NMR spectrum of hyperpolarized and thermal equilibrium ^{15}N-TPA at 9.4 T, 298K (b) Sequential ^{15}N-TPA spectrum decay, ^{15}N NMR chemical shift of (c) ^{15}N-TPA and (d) ^{15}N- TPA-d_6 in the absence and presence of Zn^{2+} (0.25eq) (e) T_1relaxation of ^{15}N-TPA derivatives measured at 9.4T.

In general, the dominant mechanism for ^{15}N T_1 relaxation is a combination of dipole-dipole (DD) relaxation and chemical shift anisotropy (CSA). DD is independent of the B_0 field strength, while CSA increases by the power of 2 with an increase in B_0.[19] The DD contribution to T_1 relaxation can be minimized by replacing the protons with deuterium in the vicinity of the observed nucleus, because dipole-dipole (DD) interaction with ^{1}H is the most efficient mechanism for relaxation.[20] Another way to elongate T_1 is to decrease the CSA contribution, which can be minimized by

increasing the symmetry of the molecule. TPA already has a symmetrical structure; thus for this molecule, the CSA contribution is not expected to be significant. However, the central ^{15}N in TPA has adjacent protons in the methylene groups that can significantly shorten the ^{15}N T_1 through dipole-dipole interaction. Therefore, a deuterated ^{15}N TPA derivative, ^{15}N-TPA-d_6, was synthesized to elongate the T_1. The T_1 of ^{15}N TPA-d_6 was measured at various magnetic field strengths to understand the dominant relaxation mechanism. T_1 values were found to be 79s at 1T, 89s at 3T, and 71s at 9.4T (Table 2.2), indicating that it is largely independent of magnetic field strength. The somewhat shorter T_1 at 1T is likely due to the relaxation effect of Gd^{3+} (ProHance), which is added to improve the polarization levels during DNP. Overall, the deuteration of the ligand led to a significant (nearly 3-fold) increase in the 15N spin lattice (T_1) relaxation time (T_1 = 89 s at 3 T) suggesting that the dominant T_1 relaxation mechanism is dipole-dipole relaxation.

OX063	ProHance	**Hyperpolizer**	**T_1 (sec)**
15mM	2mM	Hypersense	71 s (9.4T)
15mM	0mM	Hypersense	89 s (3T)
15mM	2mM	SpinLab	79 s (1T)

Table 2.2 T_1 of ^{15}N-TPA-d_6 under the different field and absence/presence of GdDO3A

2.3.5 Magnetic resonance spectroscopic imaging of HP ^{15}N-TPA-d_6

In general, chemical shift imaging (CSI) provides spectral (chemical environment) information as well as spatial information. CSI of the hyperpolarized TPA ^{15}N signal can be used to map *in vivo* Zn^{2+} distribution. In a proof of principle imaging experiment, ^{15}N chemical shift images of phantoms containing HP ^{15}N-TPA-d_6 in the absence and presence of Zn^{2+} were collected to

demonstrate the feasibility of in vivo imaging of Zn-distribution (Figure 2.5). The free and Zn-bound ^{15}N-TPA-d_6 were easily distinguished by ^{15}N-CSI due to the 20ppm ^{15}N NMR chemical shift separation. This result clearly demonstrates that HP ^{15}N-TPA-d_6 has a potential as a Zn^{2+} imaging probe for ^{15}N MRI imaging.

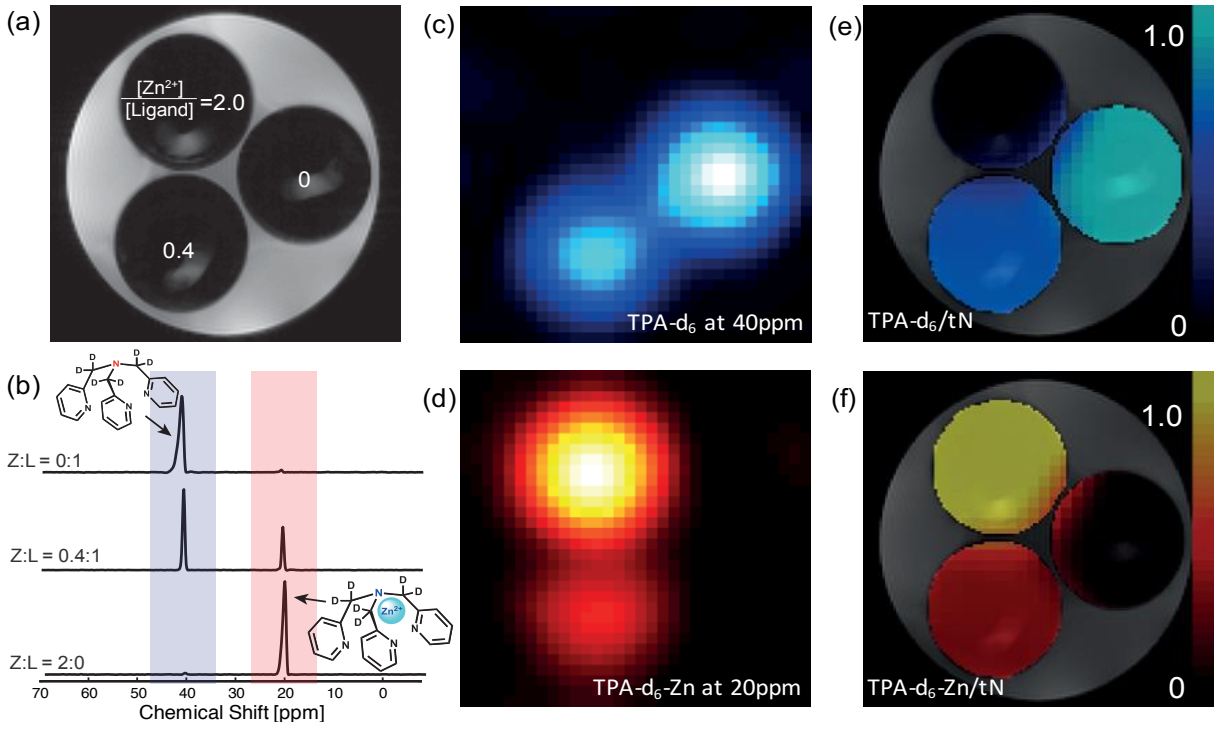

Figure 2.5 Hyperpolarized ^{15}N MR imaging of ^{15}N-TPA-$d_6$in HEPES buffer, Axial imaging slice that contains different Zn^{2+} concentration phantom (a) contrast-enhanced proton MRI of phantom (b) ^{15}N spectra with different ratio of Zn^{2+} to ^{15}N-TPA-d_6 (c) ^{15}N-CSI imaging based on free ligand (40ppm) and (d) ^{15}N-TPA-d_6 and Zn^{2+}complex (20ppm) (e-f).

2.3.6 Consideration for effective hyperpolarized MR Zn^{2+} probe

In the previous section, the feasibility of TPA as hyperpolarized ^{15}N Zn^{2+} sensor was demonstrated. However, there are several factors to be considered for effective use in a biological system.

2.3.6.1 Selectivity toward Zn^{2+} and binding stoichiometry

Competition of other species with Zn^{2+} for TPA could potentially interfere with Zn binding. In biological systems, competition can arise from protons (ligand protonation) or binding to endogenous metal ions; such as Ca^{2+}, which is the most abundant metal ion in tissue (1 to 2 mM extracellular concentration).

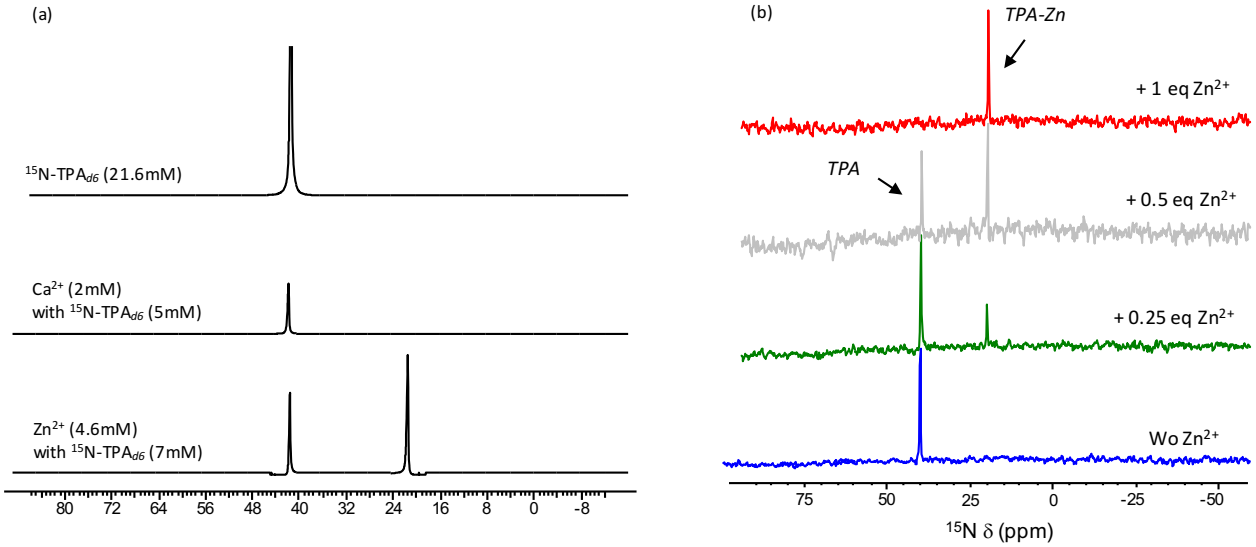

Figure 2.6 Zn^{2+} binding selectivity and stoichiometry of TPA (a) single-scan ^{15}N spectra in present of Ca^{2+} and (b) thermal ^{15}N NMR spectroscopy in the presence of various Zn^{2+} concentrations

In principle, protonation of the ligand at the ^{15}N-atom can affect the Zn-binding in the pH range of the pK_a. Fortunately, the pK_a values of TPA (2.55, 4.35, 6.17)[31] are lower than physiological pH range and the ^{15}N chemical shift of the ligand is not pH dependent in the range of pH 6.4-8.0. TPA has been actively studied as an optical Zn^{2+} imaging probe and its high Zn^{2+} binding

selectivity is well-established.[14,15] Hyperpolarized studies confirmed that interference was not observed from Ca^{2+} ions (2 mM) at biologically relevant pH values (Figure 2.6.a). In addition, one-to-one stoichiometry of ^{15}N-TPA-d_6 binds to Zn^{2+} was indicated by thermal ^{15}N NMR spectroscopy (Figure 2.6.b).

2.3.6.2 Detection limit of Zn^{2+} concentration in hyperpolarization study

Zn^{2+} detection limit was determined by adding decreasing amounts of Zn^{2+} to hyperpolarized samples of ^{15}N-TPA-d_6 and observing the ^{15}N signal of the Zn-complex in buffered solutions. These experiments revealed that the detection threshold of free Zn^{2+} was between 1-5 μM by HP ^{15}N spectroscopy of ^{15}N-TPA-d_6 (Figure 2.7). This value is lower than the intracellular concentration of Zn^{2+} in all secretory cells in mammalian tissues (μM to mM)[3,21,22] so it is anticipated that these HP Zn^{2+} sensors could be used to monitor Zn levels in diseases associated with low levels of Zn^{2+} in secretory granules such as diabetes, prostate cancer, and perhaps pancreatic cancer.

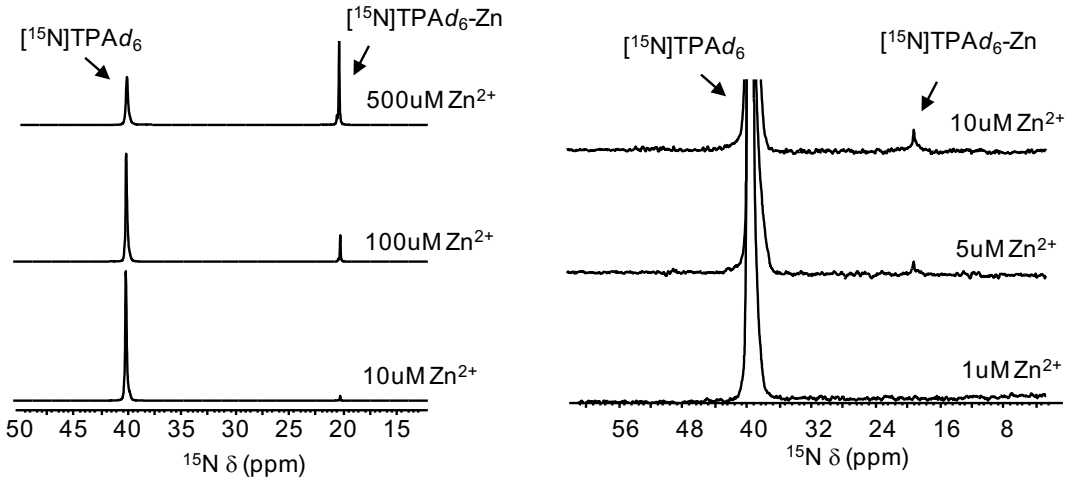

Figure 2.7 Single scan of ^{15}N NMR spectra of hyperpolarized HP ^{15}N-TPA-d_6 (1.2mM) with various concentration of Zn^{2+}

2.3.6.3 Binding affinity of TPA with Zn^{2+}

K_D is defined as the equilibrium constant for the dissociation reaction of the complex:

$$[TPA - Zn] \leftrightharpoons [TPA] + [Zn] \tag{2.4}$$

$$K_D = \frac{[TPA][Zn]}{[TPA-Zn]} \tag{2.5}$$

The low K_{DZn} of the complex indicates strong interaction of the ligand with Zn^{2+} and thus the equilibrium is shifted to the formation of the Zn^{2+} complex. Since the unit of K_D is in mol/L (M), it can be directly related to the concentration of Zn^{2+}. To quantitatively determine the Zn^{2+} concentration *in vivo* with reasonable accuracy by measuring the ratio of [TPA-Zn]/[TPA], the K_D dissociation constant should approximately match the level of Zn^{2+} in the potential target organ of interest, and is typically in the micromolar to nanomolar range. In other words, if the

Zn^{2+} concentration is significantly less than K_D, only the Zn^{2+} complex would be detected whereas if the Zn^{2+} concentration is much higher than K_D, only the free ligand would be detected. The binding competition of Zn^{2+} between the free Zn^{2+} sensor and other biological endogenous Zn^{2+} chelators should also be considered. In this context, the Zn^{2+} sensor should not have significantly higher binding affinity for Zn^{2+} than any endogenous enzymes or proteins since it could then induce an imbalance of Zn^{2+} homeostasis (i.e. it would remove Zn^{2+} bound to biomolecules). Since the dissociation constant of TPA toward Zn^{2+} is very low ($\log K_D \approx -11$), it cannot be used to quantitatively measure Zn^{2+} because [TPA-Zn] and [TPA] would be below the detection limit of HP-15N. However, it can be used to qualitatively observe in vivo Zn^{2+} by detecting the ^{15}N signal of the Zn-complex. Therefore, a derivative of TPA was designed and synthesized in which one of the methylpyridyl side-arms was replaced with a non-coordinating benzyl moiety (^{15}N-BP). This ligand is expected to have a weaker affinity for Zn^{2+} based on its 3 donor nitrogen structure. The dissociation constant of TPA ($K_D \approx 0.04$nM) and BP ($K_D \approx 300$nM) with Zn^{2+} were measured by competitive assay using the fluorophore ZnAF-2F (Kd = 5.5nM)[23]. Even though the binding affinity of BP is in the optimal range for an in vivo Zn^{2+} sensor, the solubility is not suitable for dissolution DNP. The benzyl group increases the hydrophobicity and decreases the solubility in water. Hyperpolarized ^{15}N MRS experiments of ^{15}N-BP were performed under the same conditions as for TPA. The chelation of Zn^{2+} ions by ^{15}N-BP was studied using thermal ^{15}N NMR, which revealed an 8 ppm upfield chemical shift change upon complexation (Figure 2.8.a). Hyperpolarized ^{15}N signal can be detected only when ethanol is used for dissolution (T_1 =14.5s, 9.4T) (Figure 2.8.b and c).

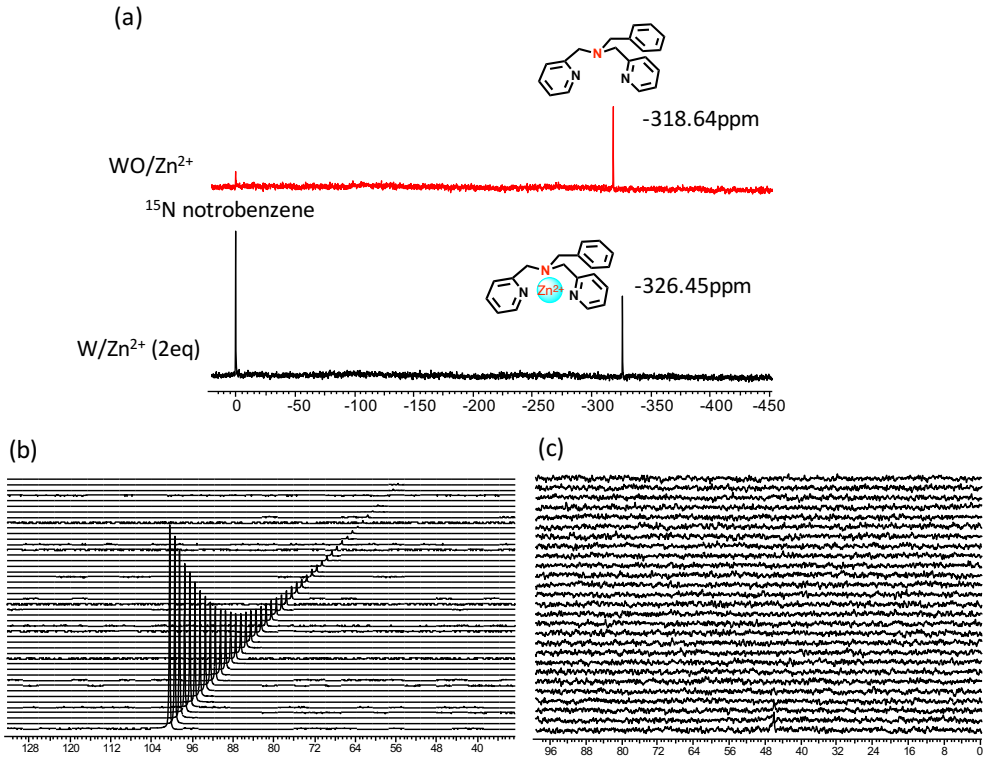

Figure 2.8 DNP-^{15}NMR experiments of ^{15}N-BP (a) thermal ^{15}N NMR study of ^{15}N-BP in the absence and presence of Zn^{2+} (b) hyperpolarized ^{15}N spectrum decay of ^{15}N BP in ethanol, and (c) PBS dissolution at 9.4T. The chemical shift is referenced to nitrobenzene.

2.3.6.4 Biocompatibility as *in vivo* Zn^{2+} sensor

It is well documented that serum albumin is capable of binding and transporting various hydrophobic molecules with aromatic group such as benzyl.[24,25] This binding significantly alters the pharmacokinetic and pharmacodynamic properties of the drug. In addition, binding also affects T_1 shortening leading to rapid loss of hyperpolarized magnetization by increasing the rotational correlation time (τ_c). The related information can be found in Figure 1.16 in the previous chapter. TPA is expected to strongly bind to albumin due to its pyridine rings. Therefore, the effect of albumin binding on the hyperpolarized ^{15}N signal of TPA was studied

using HP-^{15}N-TPA. (Figure 2.9.a). As expected, the total loss of ^{15}N polarization was observed within seconds in mouse plasma as well as in human serum albumin (0.5mM) presumably due to the accelerated T_1-mediated signal decay as a result of albumin binding[26] (Figure 2.9.a).

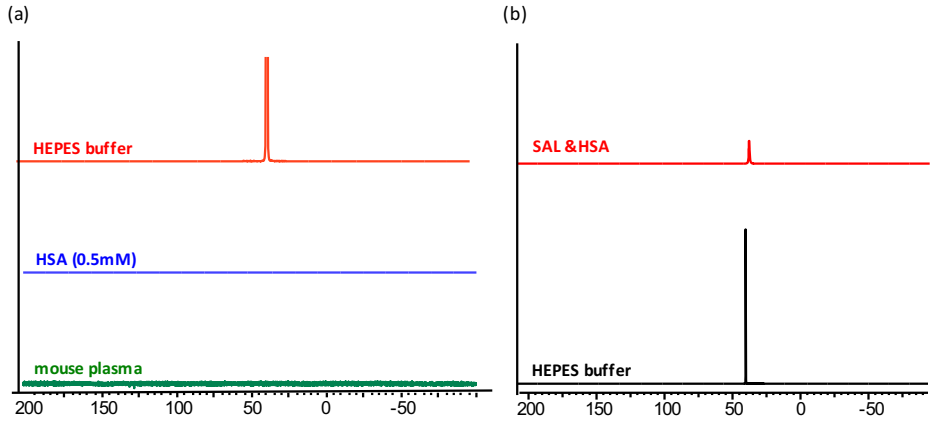

Figure 2.9 a) Competitive displacement experiment using salicylic acid. Single scan ^{15}N NMR spectra of hyperpolarized ^{15}N-TPA (7mM) in (a) mouse plasma, HSA (0.5mM), and HEPES (pH 7.0) and (b) with salicylic acid (SAL, 25mM in HEPES) as displacer

The binding constant of TPA to human serum albumin (HSA) was measured by isothermal titration calorimetry (ITC) and was found to be $K_d = 1x10^{-7}$ M. The rapid loss of polarization would obviously be an obstacle for in vivo studies. To address this problem, the feasibility of using a displacer to eliminate the HSA binding by competitive inhibition[27,28] was studied. First, salicylate was tested. However, competitive displacement by salicylate only partially restored the ^{15}N signal (Figure 2.9.b). This was not surprising as salicylic acid binds to HSA with lower affinity ($K_d \sim 10^{-4}$M) than TPA (Figure 2.10) through multiple binding sites including the primary subdomain site I, site II, and other multiple weak binding sites.[29]

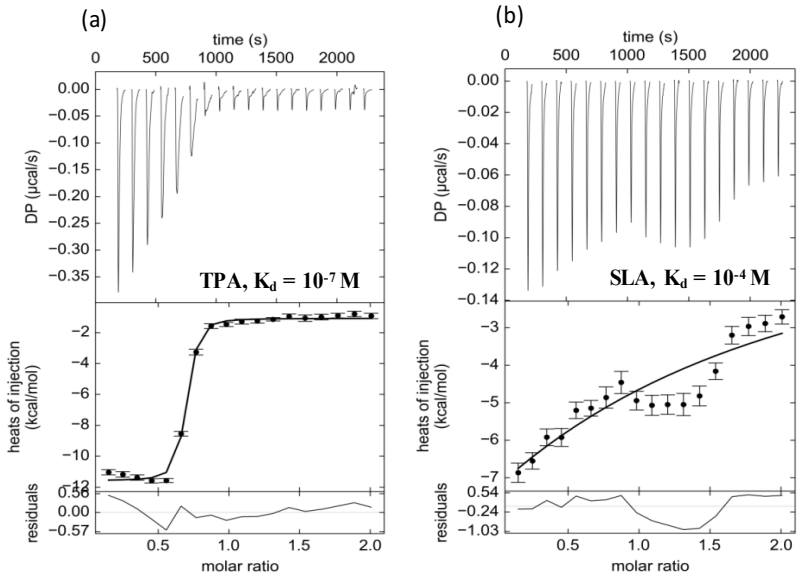

Figure 2.10 Direct measurement of HSA binding affinity to (a) TPA and (b) SAL by isothermal titration calorimetry, HSA 26uM in HEPES buffer (100mM, pH 7.0)

Next, iophenoxic acid (IPA) was tested. Iophenoxic acid is non-toxic and was used as an X-ray contrast agent in the past.[30] IPA binds more strongly to HSA than TPA (Kd ~10^{-8} M) at drug site I as well as drug site II. Competitive displacement experiments with IPA and HP-^{15}N-TPA-d_6 in the presence of human plasma (0.5 mM) revealed that 5 mM IPA nearly completely restored the hyperpolarized ^{15}N TPA signal (Figure 2.11.a)

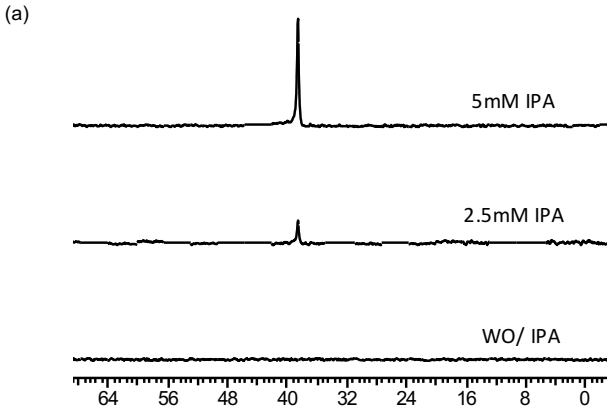

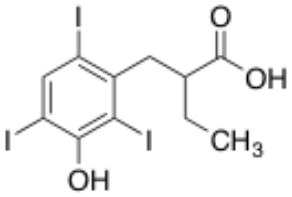

Iophenoxic acid (IPA)

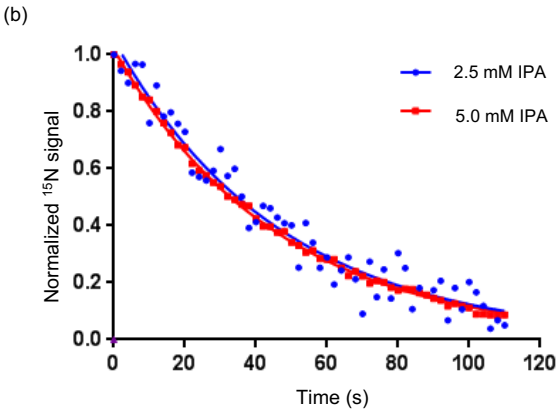

IPA (mM) in plasma	T_1 of ^{15}N-TPA-d_6
2.5	51.3 ± 2.3
5.0	50.4 ± 0.4

Figure 2.11 Competitive displacement experiment using iophenoxic acid (IPA) (a) single scan of ^{15}N NMR spectra of hyperpolarized ^{15}N-TPAd_6 (5mM) in various concentration of IPA (b) T_1 decay

2.4 Conclusions

In this study, hyperpolarized ^{15}N labeled Zn^{2+} sensors were designed with the goal of detecting the *in vivo* Zn^{2+} distribution using ^{15}N magnetic resonance spectroscopy. ^{15}N labeled tripodal ligand tris(pyridylmethyl)amine (TPA) was found to selectively bind Zn^{2+} with long T_1 and high ^{15}N MR sensitivity. The T_1 value of deuterated tris(pyridylmethyl)amine-d_6 (^{15}N-TPA-d_6) was found to be around 80s and Zn^{2+} detection limit of hyperpolarized ^{15}N-TPA-d_6 was found to be

around 5 μM Zn^{2+}. It was shown that protonation and Ca^{2+} binding does not interfere with Zn sensing. As expected, albumin binding of the hyperpolarized ligand resulted in rapid loss of ^{15}N polarization. However, the hyperpolarized ^{15}N signal could be restored by the addition of a competitive displacer (iophenoxic acid) that has a higher affinity for albumin than TPA. These results demonstrate that ^{15}N labeled, deuterated TPA derivatives are promising hyperpolarized Zn^{2+} sensors. For future study, toxicity and biodistribution need to be investigated for *in vivo* Zn^{2+} detection.

2.5 References

1. De Leon-Rodriguez, L., Lubag Jr, A.J.M. & Dean Sherry, A. Imaging free zinc levels in vivo – What can be learned? *Inorganica Chimica Acta* 393, 12-23 (2012).

2. Costello, L.C., Feng, P., Milon, B., Tan, M. & Franklin, R.B. Role of zinc in the pathogenesis and treatment of prostate cancer: critical issues to resolve. *Prostate Cancer And Prostatic Diseases* 7, 111 (2004).

3. Costello, L.C. & Franklin, R.B. Zinc is decreased in prostate cancer: an established relationship of prostate cancer! *Journal of biological inorganic chemistry : JBIC : a publication of the Society of Biological Inorganic Chemistry* 16, 3-8 (2011).

4. Ghosh, S.K.*, et al.* A Novel Imaging Approach for Early Detection of Prostate Cancer Based on Endogenous Zinc Sensing. *Cancer Research* 70, 6119-6127 (2010).

5. Li, Y.V. Zinc and insulin in pancreatic beta-cells. *Endocrine* 45, 178-189 (2014).

6. Loeb, S. Prostate Health Index - Improving screening in men with family history. *Nature Reviews Urology* 10, 497 (2013).

7. Rice, B.W., Cable, M.D. & Nelson, M.B. *In vivo* imaging of light-emitting probes. *Journal of biomedical optics* 6, 432-440 (2001).

8. Clavijo Jordan, M.V.*, et al.* Zinc-sensitive MRI contrast agent detects differential release of Zn(II) ions from the healthy vs. malignant mouse prostate. *Proceedings of the National Academy of Sciences* 113, E5464-E5471 (2016).

9. Ardenkjær-Larsen, J.H.*, et al.* Increase in signal-to-noise ratio of > 10,000 times in liquid-state NMR. *Proceedings of the National Academy of Sciences* 100, 10158-10163 (2003).

10. Mishra, A., Pariani, G., Oerther, T., Schwaiger, M. & Westmeyer, G.G. Hyperpolarized Multi-Metal 13C-Sensors for Magnetic Resonance Imaging. *Analytical Chemistry* 88, 10790-10794 (2016).

11. Naoko, K.*, et al.* A Sensitive Zinc-Activated 129Xe MRI Probe. *Angewandte Chemie International Edition* 51, 4100-4103 (2012).

12. Zhang, J., Cui, H., Hojo, M., Shuang, S. & Dong, C. Synthesis and spectral studies of 2-[(N-ethyl carbazole)-3-sulfonyl ethylenediamine]-1-N,N-2-(2-methypyridy) as a fluorescence probe for Zn2+. *Bioorganic & Medicinal Chemistry Letters* 22, 343-346 (2012).

13. Frederickson, C. Imaging Zinc: Old and New Tools. *Science's STKE* 2003, pe18-pe18 (2003).

14. Dai, Z. & Canary, J.W. Tailoring tripodal ligands for zinc sensing. *New Journal of Chemistry* 31, 1708-1718 (2007).

15. Hahn, F.E., Jocher, C., Luegger, T. & Pape, T. Coordination chemistry of aliphatic, tripodal ligands with zinc salts. *Zeitschrift fuer Anorganische und Allgemeine Chemie* 629, 2341-2347 (2003).

16. Huang, Z., Zhang, X.-a., Bosch, M., Smith, S. & Lippard, S.J. Tris(2-pyridylmethyl)amine (TPA) as a membrane-permeable chelator for interception of biological mobile zinc(). *Metallomics : integrated biometal science* 5, 648-655 (2013).

17. Patyal, B.R.*, et al.* Longitudinal Relaxation and Diffusion Measurements Using Magnetic Resonance Signals from Laser-Hyperpolarized ^{129}Xe Nuclei. *Journal of Magnetic Resonance* 126, 58-65 (1997).

18. Lumata, L.*, et al.* DNP by Thermal Mixing under Optimized Conditions Yields >60 000-fold Enhancement of 89Y NMR Signal. *Journal of the American Chemical Society* 133, 8673-8680 (2011).

19. Claytor, K., Theis, T., Feng, Y. & Warren, W. Measuring long-lived 13C2 state lifetimes at natural abundance. *Journal of Magnetic Resonance* 239, 81-86 (2014).

20. Chiavazza, E., Viale, A., Karlsson, M. & Aime, S. 15N-permethylated amino acids as efficient probes for MRI-DNP applications. *Contrast media & molecular imaging* 8, 417-421 (2013).

21. Costello, L.C. & Franklin, R.B. The clinical relevance of the metabolism of prostate cancer; zinc and tumor suppression: connecting the dots. *Molecular Cancer* 5, 17-17 (2006).

22. Frederickson, C.J.*, et al.* Concentrations of extracellular free zinc (pZn)e in the central nervous system during simple anesthetization, ischemia and reperfusion. *Exp Neurol* 198, 285-293 (2006).

23. Hirano, T., Kikuchi, K., Urano, Y. & Nagano, T. Improvement and Biological Applications of Fluorescent Probes for Zinc, ZnAFs. *Journal of the American Chemical Society* 124, 6555-6562 (2002).

24. Bertucci, C. & Domenici, E. Reversible and covalent binding of drugs to human serum albumin: methodological approaches and physiological relevance. *Curr. Med. Chem.* 9, 1463-1481 (2002).

25. Zaton, A.M.L. & Villamor, J.P. Study of heterocycle rings binding to human serum albumin. *Chemico-Biological Interactions* 124, 1-11 (2000).

26. Bloembergen, N., Purcell, E. & Pound, R. Relaxation Effects in Nuclear Magnetic Resonance Absorption. *Phys Rev* 73, 679-712 (1948).

27. Mudge, G.H., Desbiens, N. & Stibitz, G.R. Binding of iophenoxate and iopanoate to human serum albumin. *Drug metabolism and disposition: the biological fate of chemicals* 6, 432-439 (1978).

28. Kragh-Hansen, U., Chuang, V.T.G. & Otagiri, M. Practical Aspects of the Ligand-Binding and Enzymatic Properties of Human Serum Albumin. *Biological and Pharmaceutical Bulletin* 25, 695-704 (2002).

29. He, X.M. & Carter, D.C. Atomic structure and chemistry of human serum albumin. *Nature* 358, 209 (1992).

30. Ryan, A.J., Chung, C.W. & Curry, S. Crystallographic analysis reveals the structural basis of the high-affinity binding of iophenoxic acid to human serum albumin. *BMC structural biology* 11, 18 (2011).

31. YH Chiu, Canary JW. Stability and acidity constants for ternary ligand-zinc-hydroxo complexes of tetradentate tripodal ligands.*Inorg Chem*.2003,*42*(17): 5107-16

Chapter 3

In vivo assessment of increased oxidation of branched-chain amino acids in glioblastoma

Eul Hyun Suh, Edward P. Hackett, Richard M. Wynn, David T. Chuang, Bo Zhang, Weibo Luo, A. Dean Sherry, Jae Mo Park*

The manuscript has been published for *Scientific reports* 9, 340 (2019)

3.1 Introduction

In tumors, energy dependence on substrates is significantly altered to compensate for elevated biosynthesis and bioenergetics needed for tumor proliferation.[1] For instance, most cancer cells rely on energy-inefficient aerobic glycolysis, known as 'the Warburg effect',[2] to facilitate the uptake and incorporation of nutrients into the biomass for rapid proliferation. The biosynthetic demands of rapid proliferation in cancer drive altered utilization of other nutrients such as glutamine[3] and acetate,[4,5] and branched-chain amino acids (BCAAs: leucine, valine, and isoleucine). In particular, BCAAs are reportedly essential for tumor proliferation[6-8] and altered BCAA utilization has been demonstrated in multiple cancer.[9] Overexpressed branched-chain amino acid aminotransferase 1 (BCAT1), a cytosolic enzyme that transfers α-amino groups to α-ketoglutarate to yield the respective branched-chain α-keto acid (BCKA), has been suggested as a prognostic cancer indicator.[6,10-12] Moreover, a recent study showed increased expression of mitochondrial BCAT (BCAT2) in pancreatic adenocarcinoma.[13] Despite the emerging roles of BCAAs, however, the molecular mechanism of associated enzyme activities in cancer still remains elusive.[8,9,14]

In the brain, BCAAs serve as nitrogen donors in the glutamine/glutamate cycle as well as sources for energetic and biosynthetic demands[15,16] (Figure 3.1). As the first step of BCAA catabolism, BCAAs are transaminated to BCKAs by BCAT isoenzymes. Although the BCATs catalyze the reversible transamination reaction between BCAA and BCKA, the catabolic pathway of BCAAs is the predominant direction in most cell types.[15] α-ketoglutarate is converted to glutamate *via* BCAT1 in neurons and *via* BCAT2 in astrocytes to yield the major excitatory neurotransmitter of the central nervous system.[17] In the tripartite synapse, astrocytes convert excess glutamate to α-ketoglutarate by reanimating BCKAs to maintain the concentration of glutamate below 5-10 mM as a glutamate-buffering mechanism for brain nitrogen homeostasis. As a result of this regulatory mechanism, the physiological concentration of α-ketoisocaproic acid (KIC) is maintained at 0.7 ± 0.1 μM in rat brain, which is significantly lower than KIC in rat blood plasma (18.9 ± 1.4 μM).[18] Subsequently, the BCKAs are converted to branched-chain acyl-CoA's via branched-chain α-keto acid dehydrogenase complex (BCKDC) at an irreversible oxidative decarboxylation step. Thus, CO_2 production from a BCKA provides a direct indicator of BCAA oxidation. The ensuing enzymatic reactions are unique for each BCAA with end products from each degradative pathway eventually being oxidized through the citric acid cycle (CAC). In brain malignancies (e.g., glioma), BCAA uptake via L–amino acid transporter-1 (LAT1) is enhanced compared to normal astrocytes[19] and BCAT1 activity is augmented in primary gliomas with wild-type isocitrate dehydrogenase (IDH^{wt}). In particular, the BCATs are suggested as cancer-specific biomarkers, but the directionality of the BCAT-mediated reaction and how the BCAT enzyme levels are associated with metabolic phenotypes in tumor have been addressed in different manners.[9] In glioblastoma, BCAA catabolism is

upregulated to support cell proliferation.[6] In contrast, increased reverse direction was observed in non-small cell lung cancer for tissue protein synthesis[14] and in leukemia for cancer progression.[8] As the tumor metabolism is progressively remodeled by adapting to the surrounding tumor microenvironment, it is important to understand the environmental factors and tumor heterogeneities, and therefore necessary to assess comprehensive tumor characteristics *in vivo.*[20]

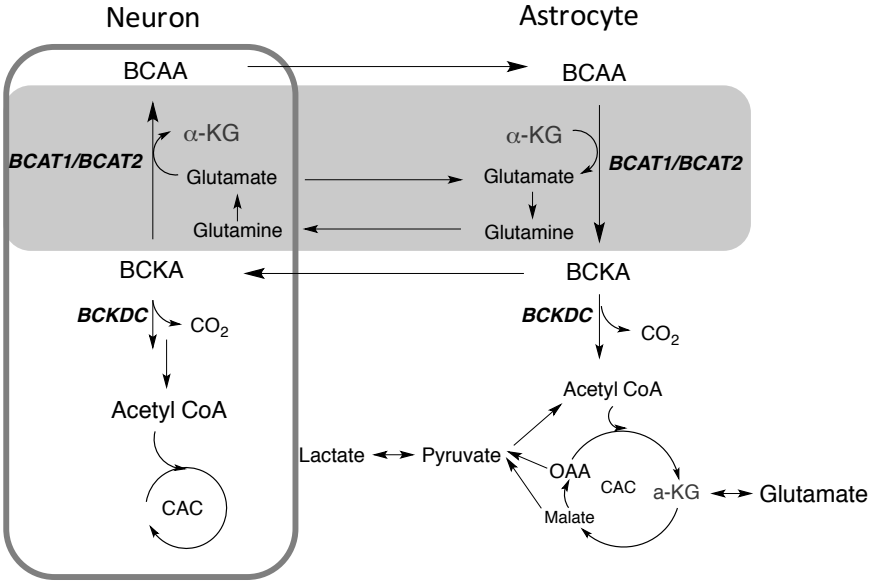

Figure 3.1 Schematic diagram of BCAA metabolism in the brain, BCAT, branched-chain amino acids aminotransferase; BCKDC, branched-chain α-ketoacid dehydrogenase complex; CAC, citric acid cycle; α-KG, α-ketoglutarate; OAA, oxaloacetate.

Non-invasive assessment of *in vivo* BCAA metabolism is crucial to understand the altered BCAA metabolism and to identify potential imaging biomarkers in cancer. PET tracers such as [1-^{11}C]L-leucine are used to quantify BCAA uptake and to estimate regional rates of cerebral protein synthesis from BCAAs using a complex kinetic model.[21,22] However, the absence of spectral information in PET limits the access to the downstream metabolites of BCAA metabolism. Dynamic nuclear polarization (DNP or 'hyperpolarization') in combination with a

rapid dissolution and ^{13}C MR spectroscopy allows *in vivo* investigation of multiple metabolic pathways by detecting metabolic flux of ^{13}C labeled substrates.[23] It has been a useful imaging tool for assessing cancer-specific enzyme-catalyzed metabolic phenotypes.[24,25] In particular, hyperpolarized (HP) [1-^{13}C]KIC has been used to assess BCAT-mediated leucine metabolism in the brain *in vivo*.[26] [1-^{13}C]KIC has a relatively long longitudinal relaxation time (T_1), a key parameter that determines the length of the observable time-window for *in vivo* metabolism. KIC is rapidly transported into the cell via monocarboxylic transporter (MCT)[26] and can assess both BCAT and BCKDC activities via production of [1-^{13}C]leucine or $^{13}CO_2$ (and thus $H^{13}CO_3^-$), respectively. Indeed, previous studies showed that the HP [1-^{13}C]KIC conversion to [1-^{13}C]leucine was correlated with BCAT activity in prostate cancer cells, lymphoma, and normal rat brain. In the prostate cancer cells, elevated BCAT levels resulted in increased production of HP [1-^{13}C]leucine from HP [1-^{13}C]KIC.[27] Another HP [1-^{13}C]KIC study observed increased [1-^{13}C]leucine conversion in EL4 lymphoma.[28] Moreover, Butt, *et al*. demonstrated that ^{13}C metabolic imaging using HP ^{13}C KIC is a practical method to access the BCAT activity *in vivo* in rat brains.[26]

BCAA can be partially oxidized for protein synthesis or can be fully oxidized as an energy source. Although major BCAA oxidative capacity is high in skeletal muscle or liver, brain has 20% of the whole-body capacity to oxidize BCAA[29] and this rate is greater than incorporation rate of BCAA into protein.[15] Previous studies have shown increased uptake of BCAA by C6 glioma[19] and breast cancer cell lines (MDA-MB-231, MCF-7) via LAT1.[30] We hypothesized that BCAA oxidation would be increased in brain tumor-bearing rats as a unique feature of the tumor, which can be visualized by ^{13}C MRI in combination with DNP. In this study, we investigated the

feasibility of HP [1-^{13}C]KIC as an imaging agent to measure altered BCAA metabolism in glioma by assessing BCAT- and BCKDC-catalyzed *in vivo* enzyme reactions. Moreover, ^{13}C NMR isotopomer analysis was performed after a steady-state infusion of [U-^{13}C]leucine into glioma-bearing rats to elucidate the downstream metabolism of BCAA. These results were further evaluated by subsequent *ex vivo* tissue analysis of BCAT/BCKDC enzyme activities and its expression levels by biochemistry experiments.

3.2 Materials and Methods

3.2.1 Hyperpolarization study of [1-^{13}C] α-ketoisocaproic acid

[1-^{13}C] α-ketoisocaproic acid (KIC) was prepared from [1-^{13}C] α-ketoisocaproic acid sodium salt (Cambridge Isotope Laboratories, Andover, MA, USA) by dissolving in 1-M HCl (pH < 1) and extracting the aqueous layer with diethyl ether. The combined organic layer was dried over anhydrous sodium sulfate, filtered and evaporated to afford [1-13C]KIC (7M, colorless oil, purity > 95%, 94% yield).[27] For hyperpolarization, a 70-μL sample of the [1-13C]KIC mixed with 11-mM trityl radical (OX063, Oxford Instruments Molecular Biotools Ltd, Oxfordshire, UK) was placed in a sample vial, which was then assembled with a research fluid path (GE Healthcare, Waukesha, WI, USA) containing 16 mM of dissolution media (0.1 g/L Na2EDTA) in the dissolution syringe. After placed in a SPINlab® polarizer (GE Healthcare), the sample was polarized at ~0.8K in a 5T magnet by irradiating microwaves at a frequency of 139.93 GHz. The polarized sample (3 - 4 hrs) was dissolved and mixed with neutralization media (0.72 M NaOH, 0.4 M Trizma and 0.1 g/L Na2EDTA), resulting in 6.5 - 7.0 mL of 80-mM [1-13C]KIC solution (pH 7.4 - 8.2).

3.2.2 Hyperpolarized ^{13}C MRS study of F98 cell

HP ^{13}C MR cell studies were performed on a clinical GE 3T Discovery 750W MR scanner and the GE SPINlab™. F98 cells were cultured as described above and collected ($1.1 \pm 0.1 \times 108$, n = 3) and washed with PBS twice. The cells were suspended in 2 mL of DMEM media and then were placed in FalconTM 50mL centrifuge tube at 37 °C. 2 mL of HP [1-13C]KIC was injected into the tube within 15 - 18 sec following the dissolution. Dynamic and time-average 13C spectra were acquired using a custom-made ^{13}C transmit/receive surface coil (∅inner = 28 mm).

3.2.3 MR Imaging protocol

In vivo imaging studies were carried out at the clinical GE 3T Discovery 750W MR scanner ($\varnothing_{bore}$ = 70 cm). For ^{1}H imaging, a quadrature birdcage volume RF coil ($\varnothing_{inner}$ = 80 mm) was used for both RF excitation and data acquisition. After locating the rat brain at the center of the birdcage coil using a 3-plane fast gradient-recalled echo (FGRE) sequence, high-resolution axial brain images were acquired using a dual-echo T_2-weighted fast spin echo (FSE; echo times [TEs] = 11.3 msec/64.0 msec, TR = 5,000 msec, 7 - 13 slices, field of view [FOV] = 96 × 96 mm^2, matrix size = 256 × 192, slice thickness = 2 mm, echo train length = 8). B_0 field inhomogeneity over the brain region was minimized using a single voxel point-resolved spectroscopy (PRESS) sequence by adjusting linear shim currents. For ^{13}C MRSI, a custom-made ^{13}C transmit/receive surface coil ($\varnothing_{inner}$ = 28 mm) was used. A 2D spiral chemical shift imaging pulse sequence described in previous study[31] with a variable flip angle scheme[32], $\theta_n = \tan^{-1}\left(\frac{1}{\sqrt{4-n}}\right), n = 1, \ldots, 4$, was used to acquire single time-point metabolite maps of rat brain (four spatial interleaves of spiral k-space readout, spectral bandwidth = 210.8 Hz, #echoes = 64, FOV = 50 ×

50 mm^2, matrix size = 16 × 16, slice thickness = 7.7 mm, acquisition time = 1.5 sec) following an intravenous injection of 80-mM HP [1-^{13}C]KIC (injection-to-scan time = 25 sec). Finally, a CE T_1-weighted spin echo (SE) images were acquired at the end of each imaging session (TE = 12 msec, TR = 700 msec, 96 × 96 mm^2, 7 - 13 slices, matrix size = 256 × 192, slice thickness = 2 mm).

3.2.4 Image reconstruction

The HP ^{13}C MRSI were reconstructed for individual peak similarly as described in the previous study.[33] After a 5-Hz Gaussian line broadening and 4-fold zero-fillings along the time domain, an inverse FFT was applied to the raw data. Prior to a spatial apodization (hanning function) and a zero-filling (4×) along each spatial domain, chemical shift artifact was removed by correcting the off-resonance and aliasing pattern of each peak (spectral tomosynthesis), followed by a gridding onto the Cartesian coordinate and a spatial 2D inverse FFT.

Metabolic maps of HP [1-^{13}C]KIC, [1-^{13}C]leucine, and $H^{13}CO_3^-$ were produced by integrating the signal around each peak in absorption mode. The metabolic images were normalized by the maximum signal. Regions of interest (ROIs) of tumor and NAB were drawn manually to calculate the signal intensities for the metabolites. All the ^{13}C data were reconstructed and analyzed using MATLAB (Mathworks, Natick MA, USA).

3.2.5 Infusion of [U-^{13}C]leucine

^{13}C isotope tracer infusion studies were performed as previously descried.[4] After 15 - 18 days from the tumor implantation, rats were fasted (n = 3) for 15 hrs prior to leucine infusion (U-^{13}C; 99%, Sigma-Aldrich Isotec). After a tail vein catheterization under anesthesia (< 10 min), all the

rats stayed awake during the infusion. Each infusion started with a bolus injection of [U-^{13}C]leucine (0.25 mg/g per body weight in 4 mL saline solution over 1 min), continued by a slow infusion (0.006 mg/g of body weight/min in saline solution at 4.8 mL/hr). Depending on the body weight, up to 2.5 hrs were required to complete the leucine infusion. Following the completion of the infusion, each animal was fully anesthetized and 4 - 6 mL of blood sample was collected by cardiac puncture. After decapitation, the whole brain was harvested and sliced to 2-mm coronal sections using brain matrices (Ted Pella, Inc., Redding CA, USA). Tumor (112.2 ± 24 mg) and contralateral NAB tissues (92.0 ± 10.8 mg) were rapidly collected from the brain slices, immediately frozen by liquid nitrogen and stored at -80 °C. The quantification of ^{13}C fractional enrichment on glutamate methods are in supporting material.

3.2.6 Statistical analysis

Statistical significance between tumor and contralateral NAB was evaluated by a paired t-test (α = 0.05, one-tailed) using GraphPad Prism version 7.0 (GraphPad Software, Inc., La Jolla CA, USA). Unpaired t-tests were used for comparison between tumor-bearing rats and healthy controls. All the data were presented as mean ± standard deviation.

3.2.7 GBM animal model and tumor implantation

F98 glioma cell line was used for both *in vitro* and *in* vivo studies. It is histologically classified as an anaplastic glioma, which is pathologically undifferentiated malignant glioma,[34,35] and the characteristics of tumor growth are similar to human glioblastoma multiforme (GBM) in overexpression of the EGFR[35]. The F98 glioma cells (CRL-2397^{TM}) were obtained from ATCC (Manassas, VA, USA). The cells were cultured at 37 °C in a monolayer using Dulbecco's

Modified Eagle Medium (DMEM) with 10% fetal bovine serum (FBS) and streptomycin with 5% CO_2[35]. The cells were harvested at 85~ 90% confluency. Approximately 1×10^4 cells were prepared for each animal. After a Trypan blue exclusion test for cell viability, the cells were implanted into the right striatum of male Fisher rats (n = 12, body weight = 240 ± 10 g). The tumor implantation was performed at the Neuro-Models Core Facility of the University of Texas Southwestern Medical Center. The growth of tumors was confirmed after 15 ~ 18 days of implantation by T_2-weighted and contrast-enhanced (CE) T_1-weighted proton MRI. The tumor regions identified by postmortem hematoxylin and eosin (H&E) stain was better matched to the hyperintense regions of the CE T_1-weighted-MRI rather than those of T_2-weighted images.

When the tumors were established (15 ~ 18 days after the implantation) the animals were either injected with hyperpolarized [1-^{13}C]KIC for MR spectroscopic imaging (MRSI) or infused with [U-^{13}C]leucine for isotopomer analysis. Tumor volumes were estimated as 93.5 ± 10.3 mm^3 by measuring hyperintense regions in a 2D T_2-weighted MRI using OsiriX dicom viewer. Tumor sizes were further confirmed by a 2D contrast-enhanced T_1-weighted MRI (50.0 ± 26.5 mm^3). Immediately after the imaging or infusion studies, the glioma and normal-appearing brain (NAB) tissues were collected for enzyme assays, histology, or isotopomer analysis. For comparison, healthy male Fisher rats (n = 3, body weight = 252 ± 10 g) were also examined. All the animal protocols were approved by the local Institutional Animal Care and Use Committee.

3.2.8 Quantification of ^{13}C fractional enrichment on glutamate

Quantitative analysis about the downstream metabolic products of [U-^{13}C]leucine was performed using the tissue samples from the infusion study. ^{13}C NMR spectra of PCA tissue extracts of

glioma and NAB were compared. [U-^{13}C]leucine was oxidized to [1,2-$^{13}C_2$]acetyl-CoA and [2-^{13}C]acetyl-CoA, which were metabolized into [4,5-$^{13}C_2$]glutamate and [4-^{13}C]glutamate through CAC.[36] Infused ^{13}C-leucine can result in ^{13}C singlets, doublets, or multiples of [4-^{13}C]glutamate, depending on metabolic turnover. Mostly, the singlet of C4 glutamate (C4S) and doublets of glutamate (C4D) were shown in our ^{13}C leucine infusion study. The ^{13}C enrichment of C4 glutamate in brain tissue were determined by C4 glutamate doublet (C4D, $^1J_{45}$ = 51.0 Hz) and C4 glutamate singlet (C4S) of the corresponding ^{13}C resonance at 34.4 ppm. However, this singlet of glutamate (C4S) includes natural abundance level (1.1%) of ^{13}C isotope of intrinsic glutamate pool in addition to the singlets resulting from metabolic conversion of [U-^{13}C]leucine to a ^{13}C-enrichment glutamate. To exclude the contribution of the natural abundance level, the total concentration of glutamate was measured using ^{1}H NMR and an internal reference of 1-mM DSSd_6.

The amount of ^{13}C incorporation into glutamate C4S and C4D was calculated from the ratio of peak area of C4S or C4D over the peak area of the 1-mM DSSd_6 and was presented in μmol/g unit after normalization by wet tissue weight. Therefore, the portion of ^{13}C incorporated in C4 glutamate can be obtained by (β+γ)/α. (Figure 3.5d.)

$\alpha = \frac{\int 1H\ NMR\ of\ C4}{\int Dssd6}$, where α is the total glutamate concentration in the tissue sample.

$\beta = \frac{\int 13C\ NMR\ of\ C4S}{\int Dssd6}$ = [C4S] - 0.01α, where [C4S] is ^{13}C NMR integration of C4S glutamate.

$\gamma = \frac{\int 13C\ NMR\ of\ C4D}{\int Dssd6}$ = [C4D], where [C4D] is ^{13}C NMR integration of doublet of glutamate C4.

3.2.9 Lactate and leucine concentration in brain tissue *via* ^{1}H NMR

Lactate and leucine concentration of glioma and contralateral NAB brain tissues were determined from the ratio of the area of DSSd_6 (Figure 3.2). Chemical shifts were referred to internal DSSd_6 at 0 ppm, which was used an internal reference and concentration standard. The total leucine plasma level was within the physiological condition during the infusion (91.2 μmol/L in tumor-bearing rats, 152.6 μmol/L in healthy control).[37]

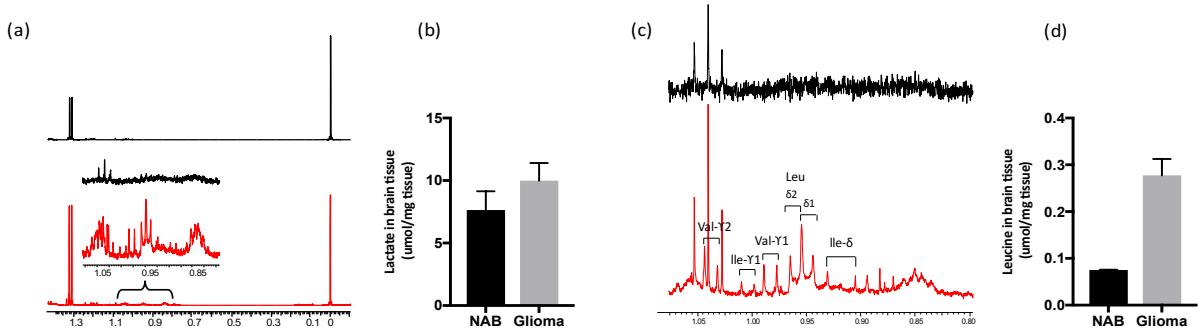

Figure 3.2 ^{1}H NMR spectra acquired from NAB (black spectrum) and glioma (red spectrum) after [U-^{13}C]leucine infusion. Elevated lactate (a) and leucine uptake (c) were measured in glioma compared to NAB (b,d).

3.2.10 Histology

Paraffin-embedded glioma and H&E staining were obtained from tumor-bearing brain slices by the Division of Molecular Pathology Core Facility at University of Texas Southwestern Medical Center (Figure 3.3).

3.2.11 Radiochemical assay for BCKDC activity

Flash frozen tumor-appearing brain tissue (117.5 ± 32 mg, n = 4) and contralateral NAB tissue (112 ± 21.7 mg, n = 5) were thawed and manually homogenized in ice-cold glass tissue

homogenizer containing 1 mL of homogenizing buffer. The homogenizer buffer was composited of 30 mM KPi (pH 7.5), 3 mM EDTA, 5 mM DTT, 3% fetal bovine serum, 5% triton X-100, 1 μM leupeptin, 50 mM NaF, 2.0 mM DCA, and 1.0 mM S-CPP. The tissue homogenate was transferred to an ice-cold 10 mL polycarbonate tube and centrifuged at 25,000 G for 10 min to spin down tissue debris. The supernatant was transferred to a new 10 mL tube and centrifuged at 40,000 G for 90 min to pellet all the branched-chain α-ketoacid dehydrogenase complex (BCKDC). The supernatant was removed and the BCKD containing pellets were resuspended into 1 mL dilution buffer composed of 50 mM HPEPS (pH 7.5), 0.5 mM DTT, 0.1 % Triton X-100, 3 % fetal bovine serum, and 1 μM leupeptin on ice. Samples (50 μL) were placed in; 24-well assay plates containing 295 μL of assay buffer composite with 30 mM KPi (pH 7.5), 0.4 mM CoA, 3 mM NAD^+, 5% fetal bovine serum, 2 mM thiamine diphosphate, 2 mM $MgCl_2$, and 42 μg/ml of human E3. 25 μL of [1-^{14}C]KIC substrate (0.5 mM in 25 μL; specific radioactivity: 1,000 cpm/nmol) was added to each well and placed bridge per well containing 2 M NaOH soaked filter wicks. Assay plates were sealed with clear Mylar adhesive film and incubated at 37 °C for 30 min to begin BCKDC activity assay. The plates were cooled down on ice for 10 min. 50 μL of trichloroacetic acid solution (20%) was added to each well to stop the assay reaction. Assay plates were further incubated at 37 °C for 45 min to completely inactivate the BCKDC. The amount of carbon dioxide ($^{14}CO_2$), trapped on 2M NaOH soaked filter wicks was measured in a liquid scintillation counter[38,39]. Protein concentration of each sample was measured by a Bradford assay with BSA as a standard. BCKDC enzymatic activity was measured as nmol CO_2/min/g tissue.

3.2.12 Spectrophotometric assay for BCAT activity

Flash frozen tumor tissue and contralateral NAB tissue were thawed and homogenized as described in the previous section (n = 3 each for tumor and NAB tissue). Spectrophotometric BCAT activity assay was performed from the rat brain tissues as described in Ref.[40] Briefly, 20 U/ml L-lactic dehydrogenase (from rabbit muscle, Sigma-Aldrich) and 10 U/ml glutamic-pyruvic transaminase (from porcine heart, Sigma-Aldrich) were prepared in 100 mM potassium phosphate (pH 7.4). Stock solution of the following substrates and enzymatic cofactors was prepared in deionized water: 42 mM KIC, 4 mM NADH, and 2 mM pyridoxal 5'-phosphate hydrate). All the assay solution was kept ice-cold. 100 mL of assay buffer solution containing 0.2M Tris, 0.6 M L-glutamic acid, and 1.6 M L-alanine (pH 8.3) and 10 μL of substrate stock solution was placed in 96-well assay plates. 2 μL of tissue homogenate and 48 μL of deionized water were added to each well, yielding a final solution of 200 μL per well. Absorbance of 334 nm wavelength at 37 °C was monitored every 30 sec for 30 min. Specific activity (U/gram protein) was calculated from protein concentration measured via Bradford assay.

3.2.13 Immunoblot

Tissues were lysed in lysis buffer (50 mM Tris-HCl, pH 7.4, 150 mM NaCl, 1% Triton-X100, and protease inhibitor cocktail) and were homogenized (BioSpec-985370 Tissue-Tearor Homogenizer) on ice, followed by sonication on ice. Equal amounts of lysates were fractionated by SDS-PAGE and subjected to immunoblot assays with the following antibodies: BCAT1 (Proteintech, 13640-1-AP), BCAT2 (Proteintech, 16417-1-AP), actin (Proteintech, 66009-1-Ig), BCKDE1A (Bethyl, A303-790A), and BCKDK (Abcam, ab151297)

3.3 Results and Discussion

3.3.1 GBM animal model

We used F98 cell line for glioma model. It is histologically classified as an anaplastic glioma, which is pathologically undifferentiated malignant glioma,[34,35] and the characteristics of tumor growth are similar with human glioblastoma multiforme (GBM) in overexpression of the epidermal growth factor receptor (EGFR).[35] The growth of tumors was confirmed 15 - 18 days after the cell implantation using both T_2-weighted and contrast-enhanced (CE) T_1-weighted proton MRI. The tumor regions identified by postmortem hematoxylin and eosin (H&E) stain was better matched to the hyperintense regions of the CE T_1-weighted-MRI rather than those of T_2-weighted images.

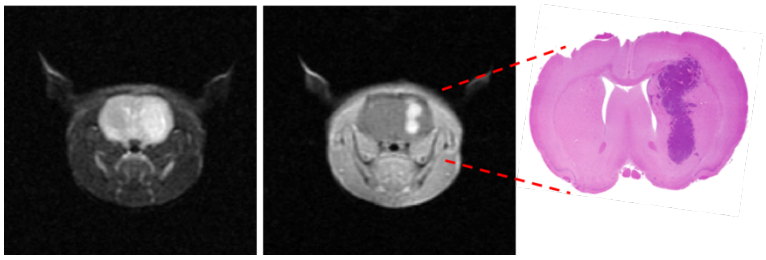

Figure 3.3 T_2-weighted and contrast-enhanced T_1-weighted proton MRI from an axial slice of rat brain 15~18 days after F98 cell implantation, H&E histology confirmed the tumor.

3.3.2 *In vivo* ^{13}C imaging branched-chain amino acid metabolism in glioma using hyperpolarized [1-^{13}C] α-ketoisocaproate to assess BCAT/BCKDC activity of glioma

We first tested HP [1-^{13}C]KIC in F98 glioma cells *in vitro.* A time-resolved pulse-and-acquire ^{13}C sequence with a non-selective radiofrequency (RF) pulse was used to monitor the injected [1-^{13}C]KIC (δ_{13C} = 172.6 ppm) and products every 3 sec. BCAT and BCKDC activities were

reported by the appearance of [1-^{13}C]leucine (δ_{13C} = 176.8 ppm) and $H^{13}CO_3^-$ (δ_{13C} = 163.1 ppm), respectively. The signal of HP [1-^{13}C]leucine reached a maximum about 20 sec after the injection of HP [1-^{13}C]KIC (Figure 3.4 a-c). All the KIC samples were polarized by a SPINlab™ DNP polarizer. The polarization level and the T_1 at 3T were measured as 24% (35 sec after the dissolution) and 77 sec from independent calibration experiments.

For *in vivo* imaging, a two-dimensional spiral chemical shift imaging pulse sequence with a variable RF scheme was used to acquire single time-point metabolite maps of glioma-bearing rat brain following an intravenous injection of HP [1-^{13}C]KIC (injection-to-scan = 30 sec, scan time = 0.5 sec).[31] Upon intravenous bolus injection of [1-^{13}C]KIC into F98 glioma rats, [1-^{13}C]leucine and $H^{13}CO_3^-$ were detected in the rat brain tissue (Figure 3.4 d-f). KIC has been found to cross the blood-brain barrier (BBB) predominantly by a carrier-mediated transport system and subsidiary by simple diffusion under physiological condition.[41] Exogenously injected HP KIC was taken up by MCTs and metabolized to leucine and bicarbonate (HCO_3^-) by BCAT and BCKDC, respectively. Reversible BCAT reaction enables a carbon isotope exchange between KIC and leucine in addition to the net flux of HP ^{13}C from KIC to leucine.[42] Therefore, HP ^{13}C KIC to leucine conversion is determined by the endogenous ^{12}C leucine pool size as well as membrane transport of KIC, delivery to the tumor, and BCAT enzyme activities.[43] On the other hand, conversion of HP KIC to HCO_3^-, a decarboxylated product of [1-^{13}C]KIC, is irreversibly mediated by BCKDC and, therefore, indicates a pure metabolic catabolic flux. ^{13}C-leucine, the transamination product of KIC, was smaller in the tumor as compared to the contralateral normal-appearing brain (NAB) ([1-^{13}C]leucine/total ^{13}C = 0.0053 in tumor *vs.* 0.0081 in NAB, p

< 0.05).The low ^{13}C conversion from KIC to leucine in the tumor implies predominant net conversion of leucine to KIC or suppressed isotope exchange between KIC and leucine (e.g., depletion of intrinsic leucine pool). Conversely, more $H^{13}CO_3^-$ was detected in the tumor ($H^{13}CO_3^-$/total ^{13}C = 0.005, $p < 0.05$) compared to the NAB (0.0027), suggesting elevated KIC catabolism by BCKDC towards isovaleryl-CoA.

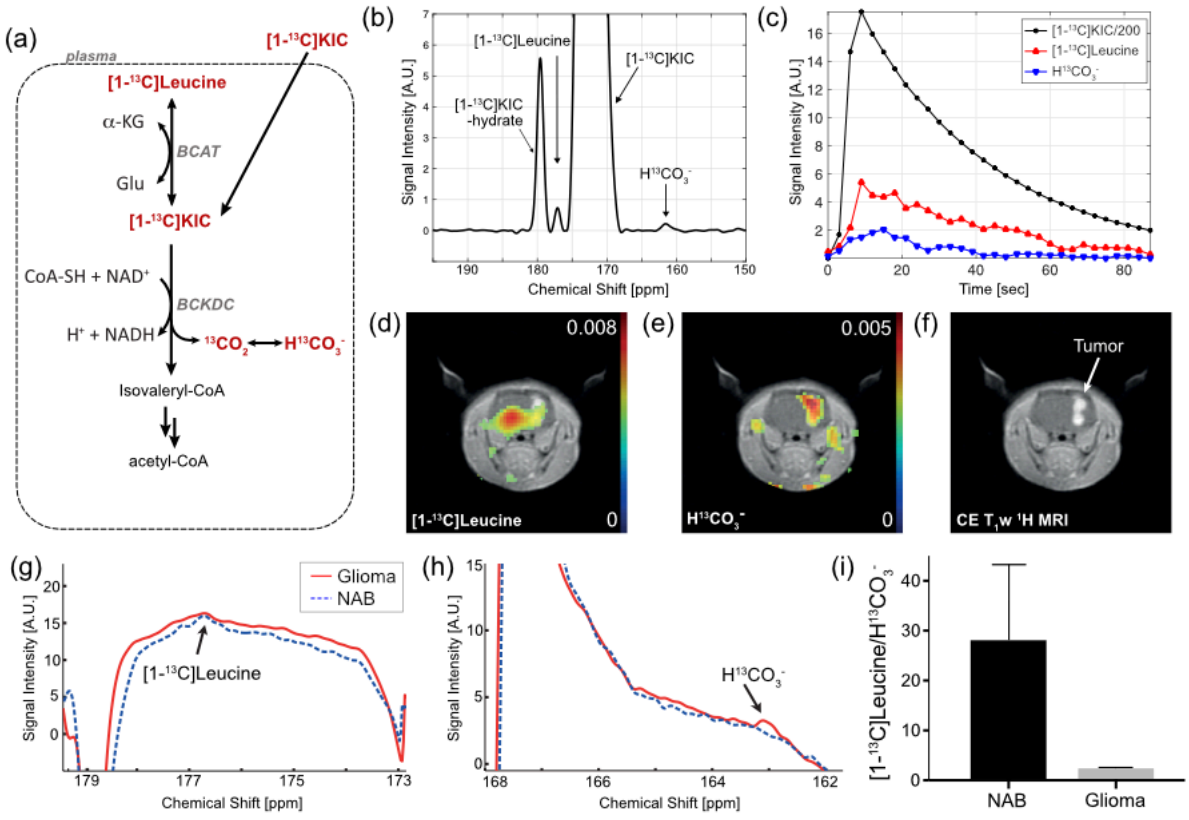

Figure 3.4 (a) Metabolic pathway of hyperpolarized (HP) [1-^{13}C]KIC. ^{13}C-labeled KIC and its metabolic products are highlighted in red. (b) An *in vitro* time-averaged spectrum from F98 cells showed the injected HP [1-^{13}C]KIC and produced [1-^{13}C]leucine and and $H^{13}CO_3^-$ peaks. (c) The corresponding time courses of HP KIC and the products. (d-e) *In vivo* chemical shift imaging of a F98 glioma-bearing rat using HP [1-^{13}C]KIC and (f) the contrast-enhanced (CE) T_1-weighted

^{1}H imaging. Metabolite distributions of [1-^{13}C]leucine and H$^{13}CO_3^-$ in a tumor-bearing rat brain slice after an injection of HP [1-^{13}C]KIC. (g-h) The reconstructed spectra in the glioma (solid red) and the contralateral normal-appearing brain (NAB; dotted blue) and (i) *in vivo* metabolite ratio of [1-^{13}C]leucine to H$^{13}CO_3^-$

3.3.3 Increasing of [U-^{13}C]leucine oxidation in F98 glioma

To elucidate the metabolic fate of BCAA in glioma, leucine metabolism was further explored in F98 glioma using *ex vivo* ^{13}C NMR isotopomer analysis. The isotopomer analysis can track multiple metabolic pathways by accessing the distribution of ^{13}C isotopomers in tissue after infusion of ^{13}C-labeled substrates. We evaluated downstream metabolism of leucine in brain tumor after a [U-^{13}C]leucine infusion into F98 glioma-bearing rats. Oxidation of [U-^{13}C]leucine in the glioma produced distinct labeling in several CAC intermediates as downstream products. In particular, ^{13}C-glutamate labeling patterns enable direct comparison of leucine utilization between glioma and NAB. The glutamate doublet in ^{13}C NMR spectra is also analyzed to determine the quantity of ^{13}C labeled acetyl-CoA entering the CAC. The protocol for ^{13}C-leucine infusion study is described in Figure 3.5 a. Both glioma and contralateral NAB tissues were harvested and freeze-clamped after a steady-state infusion of [U-^{13}C]L-leucine. ^{13}C NMR spectra from glioma and NAB tissue extracts were compared by examining the distribution of ^{13}C isotopomers. The data showed that [U-^{13}C]leucine was converted to [U-^{13}C]KIC and further catabolized to [1,2,3,4,5-$^{13}C_5$]isovaleryl-CoA and H$^{13}CO_3^-$ via mitochondrial BCKDC, followed by conversion to [2,3,4-$^{13}C_3$]acetoacetate and [1,2-$^{13}C_2$]acetyl-CoA. Both [1,2-$^{13}C_2$] and [2-^{13}C]acetyl-CoA are oxidized in the CAC and form various ^{13}C isotopomers in ^{13}C-glutamate. ^{13}C NMR spectra reflected higher quantities of ^{13}C-labeled leucine in glioma tissue versus NAB

tissue (Figure 3.5b). Glutamate derived from leucine was estimated from C4 doublet of [4,5-$^{13}C_2$]glutamate (23.1 ± 6.2 % of total glutamate pool in glioma, 15.5 ± 5.9 % in NAB, $p < 0.05$, Figure 3.5d,e). Moreover, the multiplets appearing in the lactate C2 resonance were more abundant in the spectrum of glioma tissue, reflecting oxidation of leucine in the CAC followed by cycling of three carbon units out of the CAC and into pyruvate (pyruvate cycling) (Figure 3.5c). Based on the ^{1}H MR spectroscopy, leucine concentration in brain tissue was significantly higher in glioma (0.278 ± 0.035 μmol/g of wet tissue) than in contralateral NAB (0.075 ± 0.001 μmol/g). Lactate pool was also larger in the glioma (9.989 ± 1.413 μmol/g) compared to the NAB (7.639 ± 1.506 μmol/g) (Figure 3.2). Together, these results indicate that leucine uptake and oxidation are increased in glioma. The total leucine plasma level was within the physiological levels during the infusion (91.7 ± 16μmol/L in tumor-bearing rat),[37] which implies that leucine metabolism was observed under physiological conditions. Increased catabolism of leucine in tumor tissue observed in this study is consistent with our previous *in vivo* ^{13}C imaging study using HP [1-^{13}C]KIC in F98 glioma that showed higher decarboxylation products of HCO_3^- from [1-^{13}C]KIC in the tumor compared to NAB.

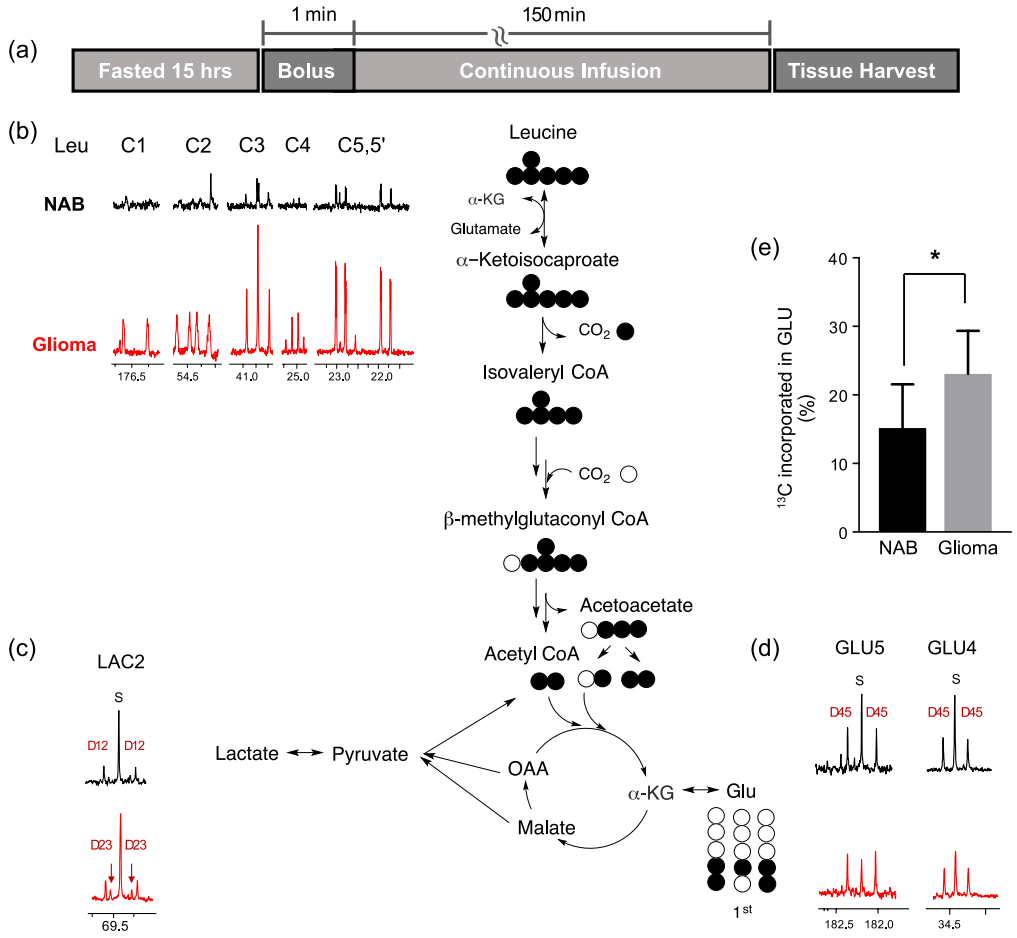

Figure 3.5 ^{13}C NMR spectra acquired from glioma and contralateral normal-appearing brain (NAB) *ex vivo* a er a steady-state [U-^{13}C]leucine infusion. (**a**) Protocol for the [U-^{13}C]leucine infusion. (**b**) Elevated leucine uptake and signi cantly higher (**c**) lactate and (**d**) glutamine labeling were observed in the tumor as compared to NAB, indicating an increased oxidation of leucine in the tumor. (**e**) ^{13}C -labeled [4-^{13}C]glutamate derived from [U-^{13}C]leucine relative to the total glutamate pool size (%) from the leucine infusion study (*$p < 0.05$). D indicates doublet.

3.3.4 *Ex vivo* assay of BCAT and BCKDC activities in brain tissues

To verify the results of the *in vivo* imaging and steady-state infusion study, enzyme activities and expression levels of BCAT and BCKDC were measured in brain tissues. BCAT activity assays were performed as previously described using *in vitro* continuous spectrophotometric

method. L-alanine aminotransferase and L-lactate dehydrogenase were used as coupled enzyme in this assay.[40] BCKDC-E1α subunit activity was assayed in the brain tissue according to the methods of radiochemical assay by [1-^{14}C]KIC substrate and measure the [^{14}C]decarboxylation by BCKDC-E1α.[44] The previous study reported that BCAT1 is a major isoenzyme in rat brain, responsible for 60 - 70% of total BCAT activity.[45] This is congruent with our western blot analysis; the expression of BCAT1, rather than BCAT2, is relatively predominant in both NAB and glioma. While the total BCAT activities were comparable between glioma (3.34 ± 0.36 U/gram of protein) and NAB (3.16 ± 0.05), the expression levels of isoenzyme BCAT1 and BCAT2 were significantly tumor-specific: lower BCAT1 and higher BCAT2 in glioma than in NAB (Figure 3.6). Increased expression level of BCAT2 with unaltered BCKDC level in glioma suggests that BCAT2 is a key enzymatic step that regulates BCAA catabolism. The distinct levels of BCAT1 and 2 in glioma might be due to the characteristics of its cellular origin as a glial cell,[35,46] since tumors conserve the metabolic phenotype of their tissue origin.[47] Indeed, BCAT2 is predominant in glial cells whereas BCAT1 is primarily in cortical neurons.[17,48,49] In contrast, both the activity and the expression level of the BCKDC-E1α subunit were at similar levels in glioma (3.795 ± 1.866 nmol CO_2/min/g tissue) and NAB (4.405 ± 0.86) (Figure 3.6). Increased expression level of BCAT2 and unaltered BCKDC level in glioma together suggests that BCAT2 is a key enzymatic step that regulates BCAA catabolism in glioma. Islam, M.M., *et al*.[45] recently reported that BCAT2 forms a protein-protein complex with BCKDC such that the substrates like KIC are channeled to the adjacent E1 subunit of BCKDC for further catabolism. Such channeling of substrates could explain the enhanced $H^{13}CO_3^-$ production observed in glioma versus normal brain tissue.

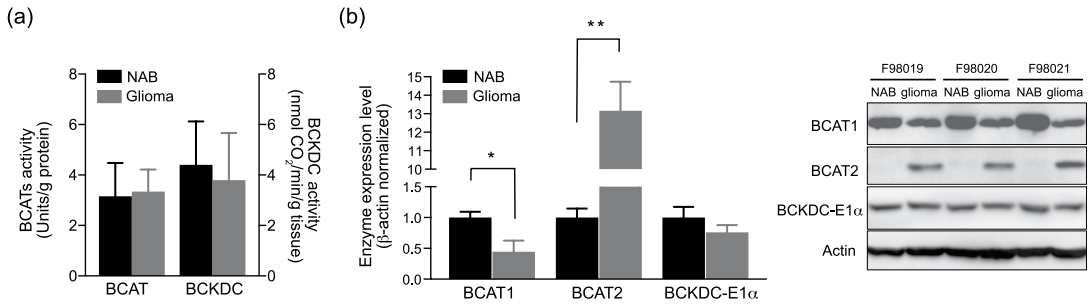

Figure 3.6 Ex vivo assay of (a) BCAT and BCKDC activities in brain tissues. (b) Protein expression levels, normalized to the protein expression in the contralateral normal-appearing brain (NAB), of BCAT1, BCAT2 and BCKDC-E1α (Western blot analysis, *$p < 0.05$, **$p<0.01$).

3.4 Conclusions

HP [1-^{13}C]KIC is a promising substrate to investigate *in vivo* brain tumor metabolism. KIC can be delivered to intracellular space via MCT and instantly converted to [1-^{13}C]leucine by BCAT[26] or to CO_2 (and thus HCO_3^-) by BCKDC. The detection of BCKDC activity is crucial for assessing BCAA oxidation since it irreversibly catabolizes BCKAs and regulates the BCAA oxidation. Here we demonstrated the feasibility of HP [1-^{13}C]KIC to assess BCAT/BCKDC activity in F98 glioma *in vivo* and discovered that leucine oxidation was increased in the tumor as a unique feature of glioma. In addition, we showed the increase of *in vivo* leucine oxidation in F98 glioma as a unique metabolic feature of brain tumor using steady-state infusion [U-^{13}C]leucine. Both the *in vivo* HP KIC imaging and the leucine infusion study indicate that KIC catabolism is upregulated through BCAT/BCKDC and further oxidized via the CAC in F98 glioma. To our knowledge, this is the first report of HP [1-^{13}C]KIC *in vivo* imaging in rat glioma model.

GBM is one of the most aggressive primary brain tumors. Diagnosis and prognosis is limited by a poor understanding of molecular biomarkers[50] and biopsy is restricted if the tumor is inoperable. Although the role of BCAA in cancer needs further investigation, multiple enzymatic steps of BCAA metabolism can be important as prognostic and diagnostic biomarkers in tumor. The HP KIC imaging method can assess activities of two key enzymes in BCAA catabolism, BCAT and BCKDC, and therefore potentially play a crucial role in tumor characterization, drug development, and therapeutic decision. In particular, BCAT1 expression is dependent on the concentration of α-ketoglutarate substrate in glioma cell lines and could be suppressed by ectopic overexpression of mutant IDH1 in immortalized human astrocytes, providing a link between IDH1 function and BCAT1 expression. This link is supported by IDH^{wt} astrocytic gliomas being characterized by high BCAT1 expression.[6] The overexpression of mutant IDH isoform 1 associated with reduced BCAT1 expression and reduced invasiveness and tumor growth provides a plausible rationale for the aggressiveness of primary GBM and the relatively less aggressive low grade or secondary gliomas. Besides glioma and other cancer applications, we expect that this technique can be utilized to investigate BCAT/BCKDC-associated pathological features in multiple other diseases with altered BCAA metabolism such as traumatic brain injury.[51]

3.5 Acknowledgements

We thank to Ian Corbin for sharing the F98 cells. We acknowledge the funding support: National Institute of Health (P41 EB015908, S10 OD018468, R37 HL034557, R00 CA168746, R01 DK62306); Cancer Prevention & Research Institute of Texas (RP140021-P2, RR140036); UT Southwestern Mobility Foundation Center; The Texas Institute of Brain Injury and Repair;

The Welch Foundation (I-1903, I-1286, AT-584); Susan G Komen® (CCR16376227).

3.6 Author Contributions

E.H.S. and J.M.P. designed the research; E.H.S., E.P.H. and J.M.P. performed the hyperpolarized ^{13}C imaging experiments; E.H.S. performed F98 cell culture; E.P.H. was responsible of tumor implantations and animal care; E.H.S. and E.P.H. performed steady-state infusion and tissue extractions; E.H.S., A.D.S. and J.M.P. analyzed ^{13}C NMR spectra; E.H.S. analyzed tissue histology; E.H.S., R.M.W., and D.T.C. performed enzyme assays; B.Z. and W.L. performed Western blot analysis; E.H.S., R.M.W., D.T.C., W.L., A.D.S. and J.M.P. contributed on writing the manuscript.

3.7 References

1. Kurhanewicz, J.*, et al.* Analysis of Cancer Metabolism by Imaging Hyperpolarized Nuclei: Prospects for Translation to Clinical Research. *Neoplasia* 13, 81-97 (2011).

2. Warburg, O über den Stoffwechsel der Carcinomzelle. *Klinische Wochenschrift* 4, 534-536 (1925).

3. Hosios, A.M.*, et al.* Amino Acids Rather than Glucose Account for the Majority of Cell Mass in Proliferating Mammalian Cells. *Developmental cell* 36, 540-549 (2016).

4. Mashimo, T.*, et al.* Acetate Is a Bioenergetic Substrate for Human Glioblastoma and Brain Metastases. *Cell* 159, 1603-1614 (2014).

5. Comerford, S.A.*, et al.* Acetate dependence of tumors. *Cell* 159, 1591-1602 (2014).

6. Tonjes, M.*, et al.* BCAT1 promotes cell proliferation through amino acid catabolism in gliomas carrying wild-type IDH1. *Nat Med* 19, 901-908 (2013).

7. Zhou, W.*, et al.* Over-expression of BCAT1, a c-Myc target gene, induces cell proliferation, migration and invasion in nasopharyngeal carcinoma. *Mol Cancer* 12, 53 (2013).

8. Hattori, A.*, et al.* Cancer progression by reprogrammed BCAA metabolism in myeloid leukaemia. *Nature* 545, 500-504 (2017).

9. Ananieva, E.A. & Wilkinson, A.C. Branched-chain amino acid metabolism in cancer. *Current opinion in clinical nutrition and metabolic care* 21, 64-70 (2018).

10. Panosyan, E.H., Lin, H.J., Koster, J. & Lasky, J.L. In search of druggable targets for GBM amino acid metabolism. *BMC Cancer* 17, 162 (2017).

11. Zhang, L. & Han, J. Branched-chain amino acid transaminase 1 (BCAT1) promotes the growth of breast cancer cells through improving mTOR-mediated mitochondrial biogenesis and function. *Biochemical and Biophysical Research Communications* 486, 224-231 (2017).

12. Zheng, Y.H.*, et al.* BCAT1, a key prognostic predictor of hepatocellular carcinoma, promotes cell proliferation and induces chemoresistance to cisplatin. *Liver International* 36, 1836-1847 (2016).

13. Dey, P.*, et al.* Genomic deletion of malic enzyme 2 confers collateral lethality in pancreatic cancer. *Nature* 542, 119-123 (2017).

14. Mayers, J.R., *et al.* Tissue-of-origin Dictates Branched-Chain Amino Acid Metabolism in Mutant Kras-driven Cancers. *Science* 353, 1161-1165 (2016).

15. Hutson, S.M., Sweatt, A.J. & LaNoue, K.F. Branched-Chain Amino Acid Metabolism: Implications for Establishing Safe Intakes. *The Journal of Nutrition* 135, 1557S-1564S (2005).

16. Yudkoff, M., *et al.* Brain Amino Acid Requirements and Toxicity: The Example of Leucine. *The Journal of Nutrition* 135, 1531S-1538S (2005).

17. Bixel, M., Shimomura, Y., Hutson, S. & Hamprecht, B. Distribution of key enzymes of branched-chain amino acid metabolism in glial and neuronal cells in culture. *The journal of histochemistry and cytochemistry : official journal of the Histochemistry Society* 49, 407-418 (2001).

18. Keen, R.E., Nissenson, C.H. & Barrio, J.R. Analysis of Femtomole Concentrations of α-Ketoisocaproic Acid in Brain Tissue by Precolumn Fluorescence Derivatization with 4,5-Dimethoxy-1,2-diaminobenzene. *Analytical Biochemistry* 213, 23-28 (1993).

19. Kim, D.K., *et al.* System L-amino acid transporters are differently expressed in rat astrocyte and C6 glioma cells. *Neuroscience research* 50, 437-446 (2004).

20. Hanahan, D. & Weinberg, R.A. Hallmarks of cancer: the next generation. *Cell* 144, 646-674 (2011).

21. Smith, C.B., *et al.* Measurement of regional rates of cerebral protein synthesis with L-[1-11C]leucine and PET with correction for recycling of tissue amino acids: II. Validation in rhesus monkeys. *Journal of cerebral blood flow and metabolism : official journal of the International Society of Cerebral Blood Flow and Metabolism* 25, 629-640 (2005).

22. Veronese, M., Bertoldo, A., Tomasi, G., Smith, C.B. & Schmidt, K.C. Impact of tissue kinetic heterogeneity on PET quantification: case study with the L-[1-11C]leucine PET method for cerebral protein synthesis rates. *Scientific reports* 8, 931 (2018).

23. Ardenkjær-Larsen, J.H., *et al.* Increase in signal-to-noise ratio of > 10,000 times in liquid-state NMR. *Proceedings of the National Academy of Sciences* 100, 10158-10163 (2003).

24. Golman, K., Zandt, R.i.t., Lerche, M., Pehrson, R. & Ardenkjaer-Larsen, J.H. Metabolic Imaging by Hyperpolarized 13C Magnetic Resonance Imaging for *In vivo* Tumor Diagnosis. *Cancer Research* 66, 10855-10860 (2006).

25. Brindle, K.M., Bohndiek, S.E., Gallagher, F.A. & Kettunen, M.I. Tumor imaging using hyperpolarized 13C magnetic resonance spectroscopy. *Magnetic Resonance in Medicine* 66, 505-519 (2011).

26. Butt, S.A.*, et al.* Imaging cerebral 2-ketoisocaproate metabolism with hyperpolarized (13)C magnetic resonance spectroscopic imaging. *Journal of cerebral blood flow and metabolism : official journal of the International Society of Cerebral Blood Flow and Metabolism* 32, 1508-1514 (2012).

27. Billingsley, K.L.*, et al.* The Feasibility of Assessing Branched-Chain Amino Acid Metabolism in Cellular Models of Prostate Cancer with Hyperpolarized [1-(13)C]-Ketoisocaproate. *Magnetic resonance imaging* 32, 791-795 (2014).

28. Karlsson, M.*, et al.* Imaging of branched chain amino acid metabolism in tumors with hyperpolarized 13C ketoisocaproate. *International journal of cancer* 127, 729-736 (2010).

29. Suryawan, A.*, et al.* A molecular model of human branched-chain amino acid metabolism. *The American Journal of Clinical Nutrition* 68, 72-81 (1998).

30. Shennan, D.B., Thomson, J., Gow, I.F., Travers, M.T. & Barber, M.C. L-leucine transport in human breast cancer cells (MCF-7 and MDA-MB-231): kinetics, regulation by estrogen and molecular identity of the transporter. *Biochimica et biophysica acta* 1664, 206-216 (2004).

31. Park, J.M.*, et al.* Metabolic response of glioma to dichloroacetate measured in vivo by hyperpolarized (13)C magnetic resonance spectroscopic imaging. *Neuro Oncol* 15, 433-441 (2013).

32. Zhao, L.*, et al.* Gradient-Echo Imaging Considerations for Hyperpolarized 129Xe MR. *Journal of magnetic resonance. Series B* 113, 179-183 (1996).

33. Dirk, M., S., L.Y., E., H.R., H., G.G. & M., S.D. Fast metabolic imaging of systems with sparse spectra: Application for hyperpolarized 13C imaging. *Magnetic Resonance in Medicine* 56, 932-937 (2006).

34. Barth, R.F. & Kaur, B. Rat brain tumor models in experimental neuro-oncology: the C6, 9L, T9, RG2, F98, BT4C, RT-2 and CNS-1 gliomas. *Journal of Neuro-Oncology* 94, 299-312 (2009).

35. Mathieu, D., Lecomte, R., Tsanaclis, A.M., Larouche, A. & Fortin, D. Standardization and detailed characterization of the syngeneic Fischer/F98 glioma model. *The Canadian journal of neurological sciences. Le journal canadien des sciences neurologiques* 34, 296-306 (2007).

36. Bixel, M.G., Engelmann, J., Willker, W., Hamprecht, B. & Leibfritz, D. Metabolism of [U-(13)C]leucine in cultured astroglial cells. *Neurochemical research* 29, 2057-2067 (2004).

37. Holecek, M., Siman, P., Vodenicarovova, M. & Kandar, R. Alterations in protein and amino acid metabolism in rats fed a branched-chain amino acid- or leucine-enriched diet during postprandial and postabsorptive states. *Nutrition & metabolism* 13, 12 (2016).

38. Chuang, D.T. & Cox, R.P. [18] Enzyme assays with mutant cell lines of maple syrup urine disease. *Methods in Enzymology* 166, 135-146 (1988).

39. Tso, S.-C.*, et al.* Structure-based design and mechanisms of allosteric inhibitors for mitochondrial branched-chain α-ketoacid dehydrogenase kinase. *Proceedings of the National Academy of Sciences* 110, 9728-9733 (2013).

40. Schadewaldt, P. & Adelmeyer, F. Coupled Enzymatic Assay for Estimation of Branched-Chainl-Amino Acid Aminotransferase Activity with 2-Oxo Acid Substrates. *Analytical Biochemistry* 238, 65-71 (1996).

41. Steele, R.D. Blood-brain barrier transport of the alpha-keto acid analogs of amino acids. *Federation proceedings* 45, 2060-2064 (1986).

42. Vannucci, S.J. & Simpson, I.A. Developmental switch in brain nutrient transporter expression in the rat. *American journal of physiology. Endocrinology and metabolism* 285, E1127-1134 (2003).

43. Day, S.E.*, et al.* Detecting tumor response to treatment using hyperpolarized 13C magnetic resonance imaging and spectroscopy. *Nat Med* 13, 1382-1387 (2007).

44. Chuang, D.T. [19] Assays for E1 and E2 components of the branched-chain keto acid dehydrogenase complex. in *Methods in Enzymology*, Vol. 166 146-154 (Academic Press, 1988).

45. Islam, M.M.*, et al.* A novel branched-chain amino acid metabolon. Protein-protein interactions in a supramolecular complex. *The Journal of biological chemistry* 282, 11893-11903 (2007).

46. Zong, H., Verhaak, R.G.W. & Canoll, P. The cellular origin for malignant glioma and prospects for clinical advancements. *Expert Review of Molecular Diagnostics* 12, 383-394 (2012).

47. Hu, J.*, et al.* Heterogeneity of tumor-induced gene expression changes in the human metabolic network. *Nature Biotechnology* 31, 522 (2013).

48. Castellano, S., Casarosa, S., Sweatt, A.J., Hutson, S.M. & Bozzi, Y. Expression of cytosolic branched chain aminotransferase (BCATc) mRNA in the developing mouse brain. *Gene Expression Patterns* 7, 485-490 (2007).

49. Garcia-Espinosa, M.A., Wallin, R., Hutson, S.M. & Sweatt, A.J. Widespread neuronal expression of branched-chain aminotransferase in the CNS: implications for leucine/glutamate metabolism and for signaling by amino acids. *Journal of neurochemistry* 100, 1458-1468 (2007).

50. Huse, J.T., Phillips, H.S. & Brennan, C.W. Molecular subclassification of diffuse gliomas: seeing order in the chaos. *Glia* 59, 1190-1199 (2011).

51. Sharma, B., Lawrence, D.W. & Hutchison, M.G. Branched Chain Amino Acids (BCAAs) and Traumatic Brain Injury: A Systematic Review. *The Journal of head trauma rehabilitation* 33, 33-45 (2018).

Chapter 4

Investigating of hyperpolarized MR probe for glyoxylate cycle

4.1 Introduction

The glyoxylate cycle, first discovered by Kornberg & Krebs (1957),[1] is the bypass of the oxidative decarboxylation steps of the TCA cycle to conserve carbon skeletons for biomass synthesis from two carbon compounds.[2] In general, acetyl-CoA enters the TCA cycle on each turn and produces of two molecules of CO_2 and four pairs of electrons for energy production. Therefore, the acetyl moiety of acetyl-CoA can't be conserved for biomass production through TCA cycle. However, in those tissues with a glyoxylate bypass, two carbon skeletons can be conserved for biomass production by bypassing the oxidative decarboxylation steps. In the combined TCA and glyoxyate cycles, acetyl-CoA condenses with oxaloacetate to form citric acid and isocitrate. Isocitrate is then cleaved to succinate and glyoxylate by aldol cleavage using isocitrate lyase (ICL; encoded by *aceA* in *E. coli*). Glyoxylate then condenses with another acetyl CoA in a Claisen-like reaction to yield malate in a reaction catalyzed by malate synthase (MS; encoded by *aceB* in *E. coli*).[3,4] This malate is used as a gluconeogenic precursor or subsequently oxidized to oxaloacetate as another molecule to start a second turn of the TCA cycle. This combined pathway then uses two acetyl CoA molecules to produce a single four-carbon intermediate using only two extra enzymes, isocitrate lyse and malate synthase.[3] In addition, cleavage of isocitrate in the first step not only yields glyoxylate but also succinate to conserve TCA cycle intermediates or to be converted into oxaloacetate (OAA) and phosphoenolpyruvate

as a precursor of glucose in gluconeogenesis (Figure 4.1). The driving force of the branch point between the glyoxylate bypass and TCA cycle is the phosphorylation of isocitrate dehydrogenase (ICD). Phosphorylation inhibits ICD activity and thus forces isocitrate production via bypass[5-7]. Intermediates of the TCA cycle also allosterically inhibit isocitrate lyase more than isocitrate dehydrogenase. Even low concentrations of TCA cycle intermediates have been shown to strongly inhibit isocitrate lyase *in vivo.*[8]

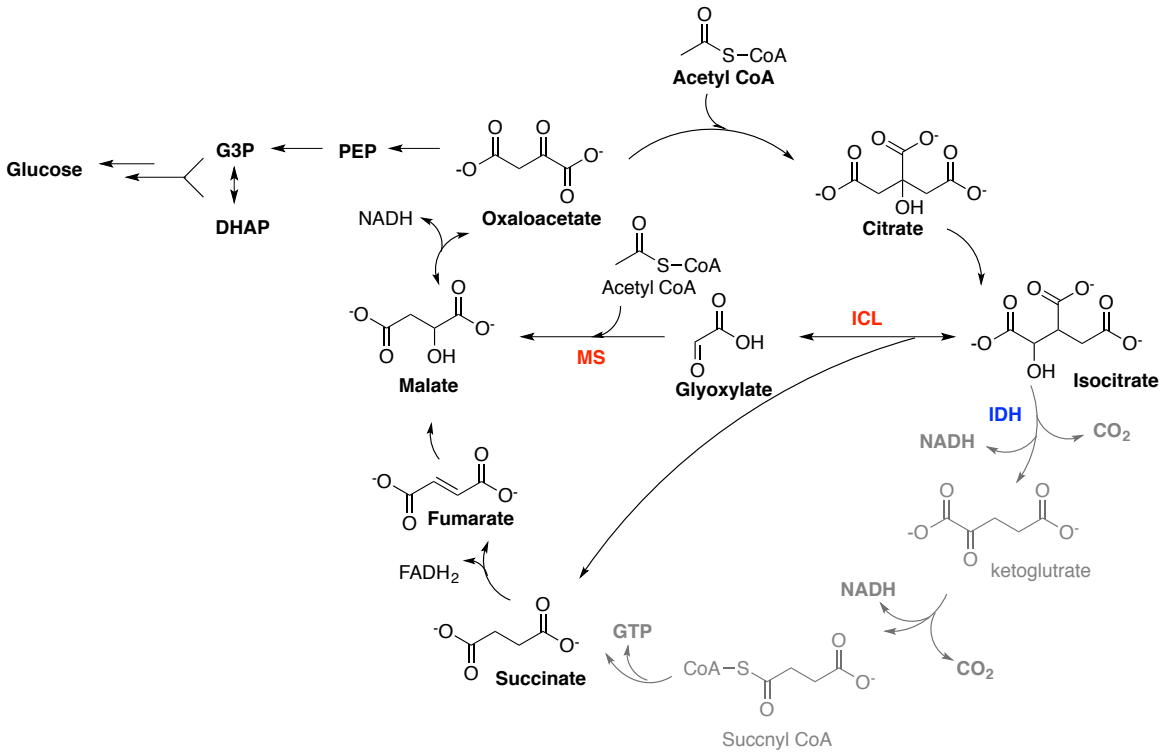

Figure 4.1 Schematic overview of glyoxylate cycle, The bypass of oxidative decarboxylation step is shown in gray. Glyoxylate cycle shares several enzymes with citric acid cycle. IDH, isocitrate dehydrogenase; ICL, isocitrate lyase; MS, malate synthase; PEP, phosphoenolpyruvate; G3P, glycerolaldehyde-3-phosphate; DHAP, dihydroxyacetone phosphate, Adapted from ref [9]

A glyoxylate cycle has been found in plants, bacteria, fungi, and nematodes. This pathway allows these species to grow on acetate or to use acetyl-CoA derived from β-oxidation of fatty

acids to synthesize carbohydrate.[10-13] In plants, the glyoxylate cycle converts fats to carbohydrate under limited carbohydrate conditions such as seed germination. The glyoxylate cycle enzymes exist in special organelles called glyoxysomes in plants, while the glyoxylate enzymes are found in the cytoplasm of yeast. Acetyl-CoA can be metabolized to succinate in glyoxysomes. The succinate must be transported back into mitochondria for conversion to oxaloacetate and PEP due to lack of fumarase and succinic dehydrogenase in glyoxysomes. The glyoxylate cycle also plays an important role in the response to oxidative stress in fungal virulence[14] since it has the potential to disturb cellular redox potential via bypassing the step of producing NADH and $FADH_2$ in the TCA cycle.

The glyoxylate cycle has been suggested to be absent in animals. However, ICL and MS activity rarely has been reported in rat and chick livers.[15-24] For a few instances, Goodman et al. demonstrated the presence of ICL and MS in human liver homogenates and conformed their activity in human liver homogenates by showing the rate of conversion of ^{14}C-isocitrate to ^{14}C glyoxylate, and the rate of conversion of ^{14}C glyoxylate to ^{14}C malate using cytochemical studies.[24] Davis et al. reported glyoxylate cycle evidence in brown adipose tissue of hibernating black bear. Peroxisome enzyme activity of palmitoyl-CoA oxidase and catalyse activity in the brown fat of the hibernating bear were increased without change in mitochondrial enzyme activity compared to non-hibernating bear. The study also demonstrated that net glycogen content increases in the dormant brown adipose tissue after incubation with palmitate.[17] However, the presence of a glyoxylate cycle in vertebrate remains controversial.[25,26] Although previous reports have suggested the presence of glyoxylate cycle enzyme activity in vertebrates, there is another notion that no apparent genes for key glyxoylate cycle enzymes, isocitrate lyase and

malate synthase, have been found. On this basis, the absence of glyoxylate cycle can be applied to in the design of drugs against bacterial and fungal parasites.[2] Evidence for glyoxylate cycle activity has been found under specific temporal or regulated conditions such as liver of the fetal guinea pig[23] and liver tissue of starving rats,[18,27] hibernating black bear brown adipose tissue,[17] chick liver after suffering vitamin D deficiency,[28] and in cartilage of the epiphyseal growth plate of rats.[29] The reasons for these rare occurrences in mammals is possibly due to the lack understanding of how glyxoylate enzymes are induced or activated or the lack of direct detection methods. Recently, the activity of CLYBL, a human mitochondrial enzyme with unknown function, was reported to have malate synthase and β-methylmalate synthase activities. Those enzymes had not been reported in humans previously. This study showed substantial malate synthase activity by producing malate through glyoxylate coupling with acetyl CoA. It also presents the close correlation of CLYBL with mitochondrial vitamin B12 processing proteins.[30] Thus, CLYBL in humans provides the potential evidence of malate synthesis from glyoxylate in mammals. As an extension of CLYBL enzyme activity, glyoxylate which is not produced through glyoxylate shunt, but through other metabolic pathways from hydroxyproline, glycine, or glycolate still can condense with acetyl CoA to generate malate.

Glyoxylate can be produced through other metabolic pathways in humans such as the intermediary metabolism of glycine, hydroxyproline, and glycolate. For example, mitochondrial hydroxyl-oxoglutarate (HOG) aldolase produces glyoxylate during hydroxyproline metabolism. High concentrations of glyoxylate are toxic to the cell so concentration is regulated by a detoxification pathway.[31] Reactive aldehydes can be catalytically removed by diverse

dehydrogenases or oxidases. Cytosolic glyoxylate is readily converted to oxalate by lactate dehydrogenase, which cannot be further metabolized by mammals and accumulates as insoluble calcium oxalate stones that cause tissue damage. In addition, cytosolic and mitochondrial glyoxylate reductase also produces a limited amount of oxalate from glyoxylate. Peroxisomal glyoxylate is converted into glycine by the peroximal enzyme, alanine-glyoxylate aminotransferase, for glyoxylate detoxification. The third pathway is the reduction of glyoxylate to glycolate by cytosolic glyxoylate reductatse (GR) in liver (Figure 4.2).[31,32]

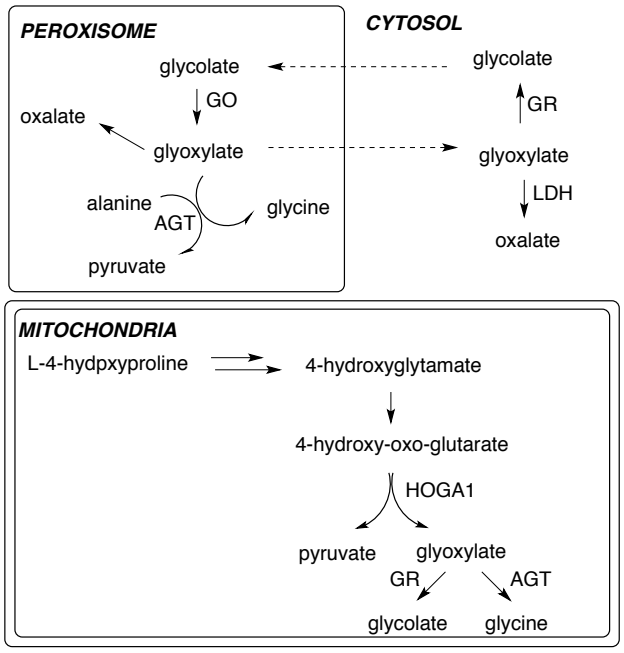

Figure 4.2 Glyoxylate detoxification metabolic pathways in human mitochondria and peroxisomes. GO, glycolate oxidase; AGT, alanine glyoxylate aminotransferase; HOGA1, 4-hydorxy-oxoglutarate aldolase; GR, cytosolic glyoxylate reductase; LDH, lactate dehydrogenase

Detection of highly reactive glyoxylate in biological samples is challenging since it can react with free amino groups. Glyoxylate is a two carbon aldo acid that reacts with amino groups to form a Schiff base imine on-enzymatically.[33] In addition, the cellular toxicity of the aldehyde is

dynamically regulated by enzymatic reaction of alanine glyoxylate aminotransferase (AGT) in mammalian systems.[34] In general, isocitrate lyase and malate synthase, enzymes unique to the glyoxylate cycle, can be detected by photometric assay or radiometric assay. Malate synthase activity can be measured by spectrophotometric assay by measuring the thiol ester cleavage from acetyl CoA in the presence of glyoxylate.[35] Alternatively, malate synthase enzyme reaction can be detected by a fluorometirc determination of malic acid generation[36] or by measuring of residual glyoxylate by derivatization to semicarbazone[37] or phenyl hydrazone[35] for spectrophotometric detection. It can be also modified to 2,4-dinitrophenyl hydrazine,[38,39] nitrophenylformazan carboxylic acid,[40,41] or *p*-nitrophenylhydrazon for colorimetrical detection.[42] However, those derivatization methods could overestimate the malate synthase activity by detecting thiol ester from other sources or by detecting semicarbazone or phenyl hydrazone moieties formed by other aldehydes derivatives.

^{13}C NMR spectroscopy using ^{13}C enriched substrates can selectively probe enriched intermediates of the glyoxylate cycle and detect metabolic products simultaneously[43]. [U-^{13}C] and [1-^{13}C] glyoxylate were tested to probe glyoxylate metabolism by examining the distribution of ^{13}C isotopomers using ^{13}C NMR and mass spectroscopy. ^{13}C NMR spectroscopy in combination with DNP can detect the single enzymatic reaction in real time by taking advantage of highly specific chemical information and high MR sensitivity. The chemical conversion of hyperpolarized metabolic substrates by specific enzymes can be monitored in real time to obtain reaction kinetics *in vivo*. For this reason, hyperpolarized [1-^{13}C]glyoxylate was proposed as an activity-based probe to assess glyoxylate cycle activity directly by detecting production of malate via malate synthase. To achieve this, [1-^{13}C]glyoxylate was synthesized from [1-

^{13}C]dichloroacetic acid using conventional organic synthesis. The feasibility of [1-^{13}C]glyoxylate was used to detect malate synthase enzyme activity in yeast and in PDH KO mouse embryo fibroblasts (MEFs) using ^{13}C isotope analysis to understand the role of glyoxylate in the context of its metabolism in mammals. In addition, the potential of [1-^{13}C]glyoxylate as a hyperpolarized metabolic probe was also examined.

4.2 Materials and Methods

4.2.1 Chemicals and reagents

All reagents purchased from Aldrich were analytical grade and used without further purification. [1-^{13}C]dichloroacetic acid was purchased from Sigma Aldrich (Cat No. 604232-500.00MG) and [U-^{13}C] glyoxylate monohydrate was purchased from Toronto Research Chemicals Inc. (Cat No. G755002).

4.2.2 Synthesis of [1-^{13}C]glyoxylate

Sodium (4.6mmol) was added to 3ml of absolute ethanol to prepare the sodium ethoxide. When the sodium had dissolved, dichloroacetic acid (1.33mmol) was added to the solution with stirring and refluxing for 3hr. The solution turned yellow-orange in color when sodium chloride begins to separate as the initial reaction[44]. After the reaction mixture was cooled to 0°, 1.1mL of 2M HCl in ethanol was slowly added for 30min to the reaction mixture. The reaction mixture was stirred at room temperature for 2hr. The reaction mixture is placed in an ice bath and the excess acid was neutralized to ~ pH 7 by slow addition of 2M sodium ethoxide. The mixture was filtered through filter paper and the precipitate is extracted using ethyl acetate three times and the organic layer was washed with water, dried over anhydrous sodium sulfate, filtered, and dried in

vacuum to afford a light yellowish oil (59 mg, overall yield 41.3%, purity >98%). ^{1}H NMR (400MHz, water) δ 5.2ppm, ^{13}C NMR (100MHz, water) δ 172.99ppm, 86.01ppm.

4.2.3 [U-^{13}C] glyxoylate study in MEFs vs *PDH* KO MEFs

WT MEF and *PDHA1* knockout MEFs cell were kindly provided by Ralph J. DeBerardinis.[45] They were cultured in Dulbecco's Modified Eagle Medium (DMEM) including 10 mM glucose, 4mM glutamine, 10% fetal bovine serum (FBS), and streptomycin with 5% CO_2. Cells were detached from the culture plate for passaging using 0.05 % trypsin. The metabolic assay using [U-^{13}C]glyoxylate was performed following a method adapted from Mullen*, et al.*[46] When the cells reached ~80% confluence (~1.2×10^6), they were labeled with 0mM, 0.5mM, 1mM, and 2mM of [U-^{13}C]glyoxylate in DMEM supplemented with 10% FBS and allowed to incubate for 6hr. For the analysis of intracellular metabolites by GC/MS, the cells were separated from the media and rinsed in ice-cold PBS and lysed by freeze-thawing three times in cold 50% methanol. The lysates were centrifuged to remove precipitated protein (16,000 × *g* and 4°C for 15 min). Total protein was quantified from the pellets (BAC protein Assay, Thermo). 5μL of sodium 2-oxobutylate solution was added as internal standard (1:500 dilution of 20% w:v solution of sodium 2-oxobutylate). The samples were dried at 42°C using air and after addition of a few drops of methylene chloride, dried again for a few more minutes to completely remove the residual moisture. The samples were derivatized by trimethylsilylation (Tri-Sil HTP reagent, Thermo Scientific) at 42°C for 2hr then used for gas chromatography-mass spectrometry (GC-MS) analysis. The abundance of labeled products were analyzed in fumarate (*m/z* 245–249) and

malate (*m/z* 335–339).[47] Chromatograms were integrated using MultiQuant software version 2.1 (Applied Biosystems SCIEX, Foster City, CA) and ^{13}C metabolic flux analysis was performed using Metran software (TLO,MIT).

4.2.4 [1-^{13}C] glyxoylate study in *saccaharomyces cerevisiae*

Saccharomyces cerevisiae were kindly provided by Benjamin Tu. Rich medium of Yeast Extract-pepton-Dextrose (YPD) contained 1% yeast extract, 2% peptone and 2% glucose, and glucose starved synthetic defined medium (SD) contains 6.7 g/L yeast nitrogen base with ammonium sulfate (DIFCO). After cells were grown in YPD overnight, they were diluted in YPD (OD_{600} = 0.2). The cells were transferred to SD medium and grown to OD_{600} ~ 1.0. for the glyoxylic acid metabolism study. The yeast cells were starved for 12 hrs., then 5mM of [1-^{13}C]glyoxylic acid or 5mM of [U-^{13}C] acetate was added to the culture media and the cells were incubated for various time. Cultured cells are collected for metabolite extractions at specific time points at 30min, 1hr, and 2hr. Collected cells were centrifuged to separate the cell pellets from the media. The cell pellets were quenched in a cold 5% PCA (0~4°C), spun down at 4°C, then extracted with 5% perchloric acid. The supernatants with metabolites were collected and dried for ^{13}C NMR spectroscopy. Proton-decoupled ^{13}C spectra of perchloric acid (PCA) extracts were acquired at 150MHz using a Bruker Avance III HD 600 MHz spectrometer equipped with a 10-mm double resonance ($^{13}C/^{23}Na$) cryoprobe. The resulting ^{13}C NMR spectra were processed and analyzed using ACD/SpecManager 12.0 software.[48]

4.2.5 Hyperpolarized studies using [1-^{13}C] glyxoylate

[1-^{13}C] glyxoylate prepared in our lab was polarized in DMSO matrix containing 2mM Gd (ProHance®) and 15mM trityl radical (OX063, GE-healthcare, UK). 50uL of sample was polarized using a HyperSense polarizer (3.35 Tesla, Oxford Instruments Molecular Biotools, UK). The polarization was fulfilled at 1.05K with 94.112 GHz microwave irradiation for 2hr and subsequently rapidly dissolved in 3mL of phosphate buffered solution (10mM PO_4^{3-}-1mM Na_2EDTA, pH~7.4) to yield 26mM hyperpolarized solution in a 10-mm NMR tube. ^{13}C NMR spectra were acquired on a 9.4 T spectrometer on a 9.4T Agilent vertical bore microimager (Agilent, USA) using 5-degree flip angle with repetition time (TR) of 5 sec.

4.3 Results and Discussion

4.3.1 Design of HP probes for detecting glyoxylate cycle activity

To elucidate glyoxylate cycle activity in cells or tissues using hyperpolarized ^{13}C MR methods, [1-^{13}C] glyoxylate was proposed as hyperpolarized ^{13}C MR probe to detect malate synthase activity.

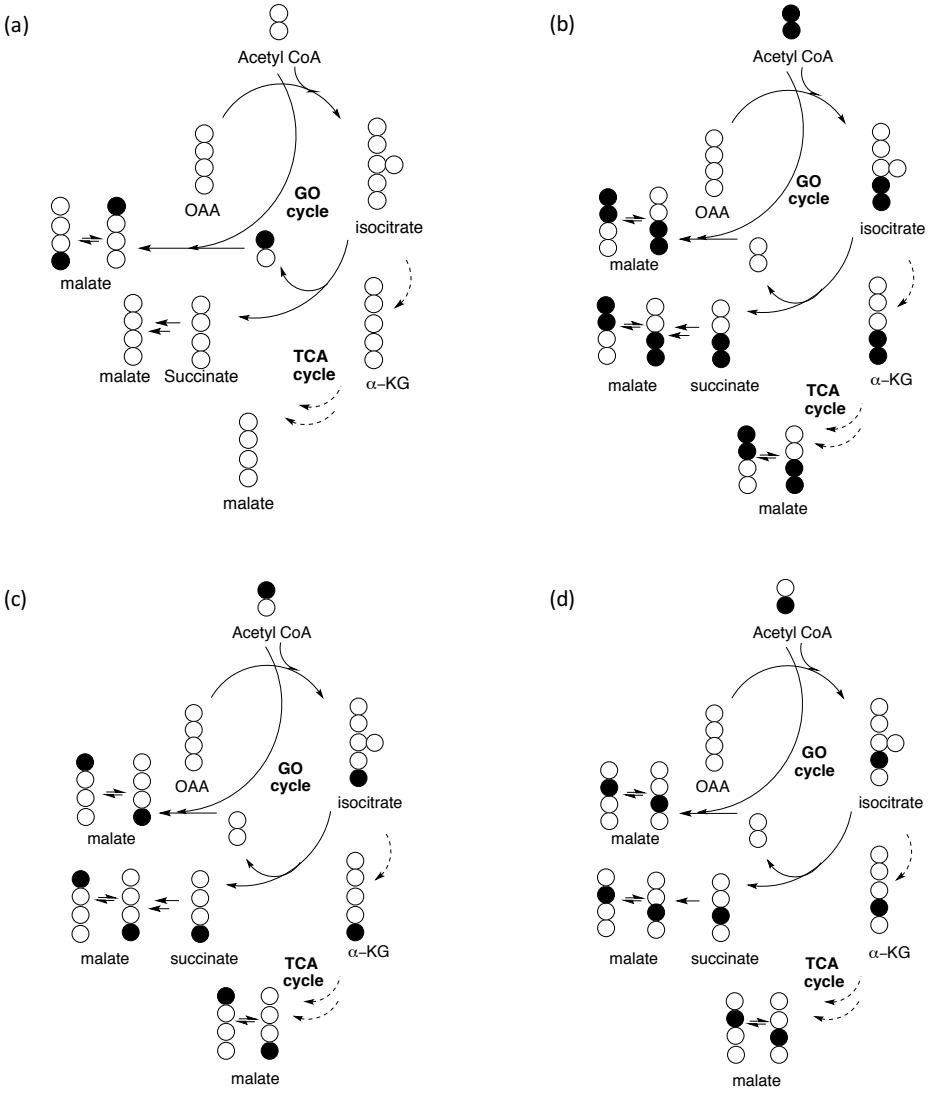

Figure 4.3 ^{13}C isotopomer distribution for incorporation of (a) [1-^{13}C] glyoxylate, (b) [1.2-$^{13}C_2$] acetate, (c) [1-^{13}C] acetate, and (d) [2-^{13}C] acetate on the glyoxylate cycle and tricarboxylic acid cycle. GO, glyoxylate cycle; TCA, tricarboxylic acid; α-KG, α-ketoglutaric acid

Many studies have used ^{13}C labeled acetate to elucidate glyoxylate metabolism in yeast[49,50] since ^{13}C tracer experiment using NMR enables detecting multiple metabolic pathway simultaneously, as well as non-invasively detecting the distribution of ^{13}C isotopomers. ^{13}C from acetate is incorporated into malate and oxaloacetate through the glyoxylate and TCA cycles and various

products of ^{13}C-labeled oxaloacetate can be detected in various metabolic products. The relative contribution of ^{13}C labeled acetate passing through the complete TCA cycle versus the glyoxylate bypass to oxaloacetate can in principle be distinguished by examining the ^{13}C labeling patterns.[50] However, when metabolic pathway turnover is low, ^{13}C labeled acetate flux though glyoxylate cycle versus TCA cycle is difficult to distinguish from acetate flux only through the TCA cycle (Figure 4.3). The relatively short polarization lifetime of HP probes limits the assay conditions in a HP ^{13}C spectroscopy study. Due to the polarization decay with a longitudinal relaxation of T_1, high turnover metabolic products cannot be detected using hyperpolarized ^{13}C labeled acetate. For this reason, [1-^{13}C] glyoxylate was proposed as a HP probe to exploit the glyoxylate cycle in hyperpolarization experiment (Figure 4.4).

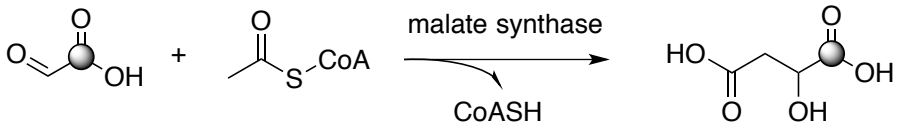

Figure 4.4 [1-^{13}C]glyoxylate as hyperpolarization probe to detect malate synthase

4.3.2 Synthesis of [1-^{13}C] glyoxylate

Several synthetic methods were attempted for preparing ^{13}C labeled glyoxylate. Synthetic Schemes were designed considering commercial availability and cost. ^{13}C labeled oxalic acid and fumarate are commercially available with reasonable price, so they were first used as starting material for the synthesis of ^{13}C labeled glyoxylate.

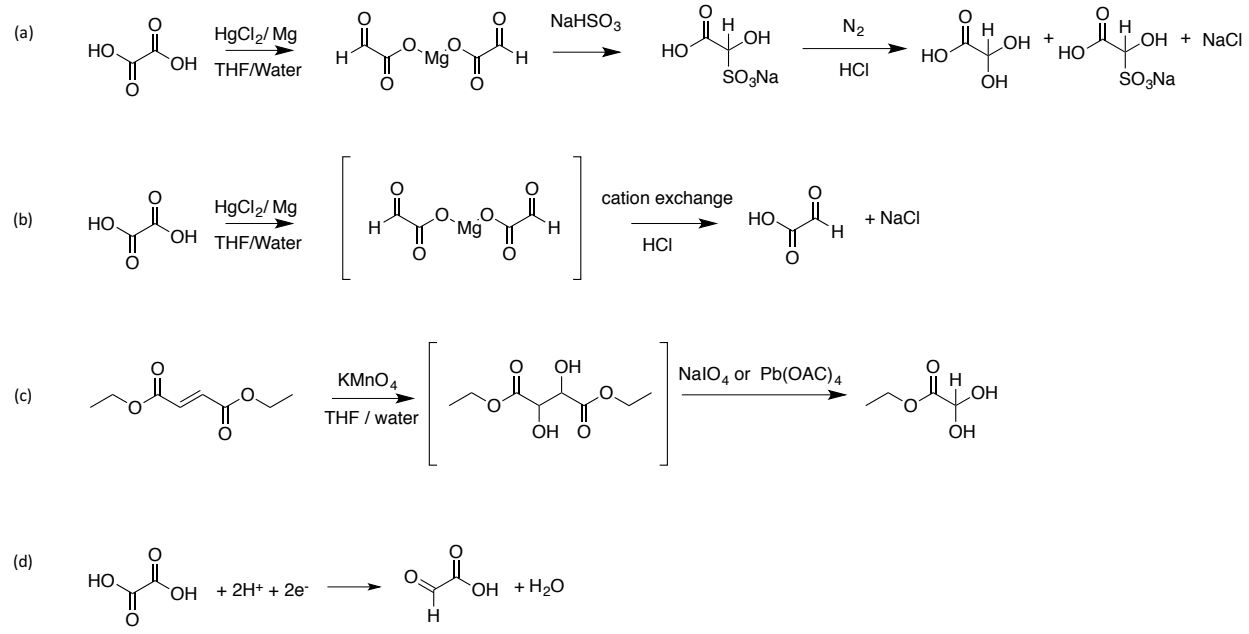

Scheme 4.1 Synthesis pathways for preparing glyoxylate

First, magnesium amalgam was employed as reducing a agent to synthesize glyoxylic acid from oxalic acid. The reaction was not complete, and it was not easy to remove starting material and intermediate sulfonate salt by the methods of organic solvent extraction and cation exchange. In addition, the yield of converting bisulfite salt to glyoxylic acid was very low, less than 5% (Scheme 4.1.a~b).[51,52] Next, based on ethyl and butyl glyoxylate prepared by oxidation of ethyl and butyl tartrate with red lead oxide, sodium bismuthate,[53] and lead tetraacetate,[54] diethyl fumarate was converted to diethyl tartrate by potassium permanganate. Further oxidation to ethyl glyoxylate using lead tetraacetate[55] and sodium periodate was tried (Scheme 4.1.c). However, the oxidation reactions were not efficient. Alternatively, glyoxylate can be synthesized from reduction of oxalate by electrolytic method, which requires electrolysis apparatus, and limits the reaction scale (Scheme 4.1.d).[56-58] Finally, [1-^{13}C]glyoxylate was synthesized by a modified

Moffett method where ethyl diethoxyacetate was synthesized from dichloroacetic acid using sodium ethoxide followed by esterification of the intermediate diethoxyacetic acid. [44] [1-^{13}C] diethoxyacetate was synthesized from commercially available [1-^{13}C] dichloroacetic acid, then the diethoxy group was hydrolyzed by 6N hydrochloric acid to yield dihydroxy acetic acid of hemiacetal of glyoxylate (Scheme 4.2). Since glyoxylate is an organic compound which has an aldehyde and carboxylic acid, the aldehyde group forms entirely gem-diol, glyoxylate hydrate in the aqueous solution with K_{eq} = 163.[59]

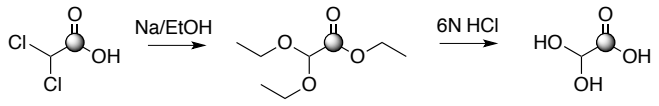

Scheme 4.2 Synthesis of [1-^{13}C] glyoxylic acid

4.3.3 [1-^{13}C] glyoxylate as an activity based probe to detect glyoxylate cycle activity

Most studies have suggested that the glyoxylate cycle is absent in mammalian metabolism since the existence of activity of the enzymes are uncertain. However, recent observations have suggested that the glyoxylate cycle may play a role in mammalian pathology of Type 2 diabetes.[34,60] Since the glyoxylate pathway can convert fat into glucose without consuming carbon, this pathway could potentially enable overproduction of glucose. It has been proposed that glyoxylate cycle is inactive under normal physiological conditions but is activated during starvation or over-supply of fat.[60] This could be related to the presence of glyoxylate cycle activity as evidenced by isocitrate lyase and malate synthease activities in the brown adipose in a dormant black bear.[26] As an extension of same context, it is possibly proposed that glyoxylate cycle can be induced in diseases associated with increased glucose metabolism such as cancer.

Song *et. al.* further proposed that increasing fat flux into hepatocytes induces proliferation of peroxisomes to increase the capacity of β-oxidation and this final product of acetate acts as a potential inducer of glyoxylate pathway.[60] However, these hypotheses involving the glyoxylate pathway existing in mammalian pathology have not been fully tested largely due to limitations in direct detection of metabolic flux through this pathway. For this reason, a ^{13}C isotope labeling study using [1,2-$^{13}C_2$] and [1-^{13}C]glyoxylate as a glyoxylate cycle probes was tested in mammalian MEF cells, and in yeast cells. In addition, a dissolution hyperpolarization study was attempted to evaluate its applicability as HP probes.

4.3.3.1 [U-^{13}C] glyoxylate incorporate into TCA cycle in normal and impaired cells

To examine whether exogenous glyoxylate incorporates into TCA cycle in normal and impaired mammalian cell differently, [U-^{13}C] glyoxylate was doped into the culture media of MEFs and PDH-KO MEFs (Figure 4.5).

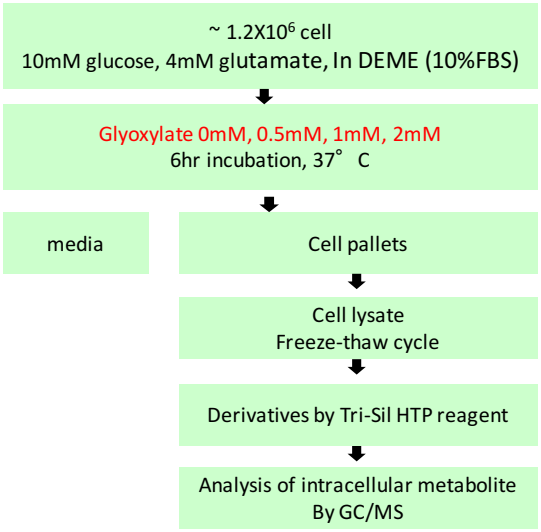

Figure 4.5 Experimental flow chart for ^{13}C isotopomer study using [U-^{13}C] glyoxylate

When cultured with [U-^{13}C]glyoxylate, no evidence could be found for integration of exogeneous glyoxylate in either MEFs nor PDH-KO MEFs. The fraction of malate and fumarate containing ^{13}C carbon were barely detectable after a 6 hr culture of MEFs and PHD-KO MEFs cells with [U-^{13}C] glyoxylate in the presence of 10mM unlabeled glucose and 4mM glutamine (Figure 4.6). These could be due to 1) these glucose-replete culture conditions may not optimal for activation of the glyoxylate cycle, 2) the permeability of glyxoylate into cells may not be favorable, or 3) the exogenous glyoxylate cannot incorporated into the glyoxylate cycle at the level of malate synthase due to a structural requirements of this enzyme as part of a metabolon. There is little information about a potential structural metabolon formed between ICL and MS to avoid intracellular accumulation of glyoxylate in the microbial systems.[61] If glyoxylate metabolic pathway is composed of multiple enzyme cluster as metabolons, exogenous glyoxylate, the intermediate of the glyoxylate cycle, may be restricted to using only glyoxylate formed in the previous step by ICL.

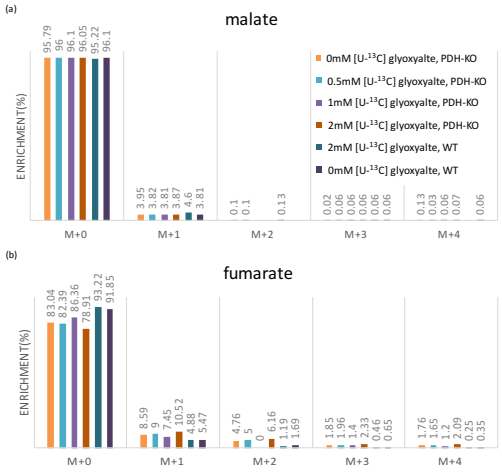

Figure 4.6 Mass isotopologues of malate and fumarate after culture of MEF and PDH-KO MEF for 6hr with [U-^{13}C]glyoxylate

4.3.5 ^{13}C NMR study of [1-^{13}C]glyoxylate utilization in *saccaharomyces cerevisiae*

There are many factors that could affect the outcome of glyoxylate metabolism in mammal cells so additional experiments were conducted in yeast cells since they are known to have an active glyoxylate cycle. Metabolism of [1-^{13}C]glyoxylate was tested in yeast under aerobic conditions and, as a control, metabolism of [U-^{13}C]acetate was also examined. The major metabolic product from acetate in yeast is trehalose (TRE,1-O-α-D-glucopyranosyl-α-D-glucopyranoside). If [1-^{13}C] glyoxyate or [U-^{13}C]acetate is utilized in yeast as a carbon source for production of trehalose, then this would be evident in a ^{13}C NMR spectrum labeled TRE based upon ^{13}C-^{13}C couplings.

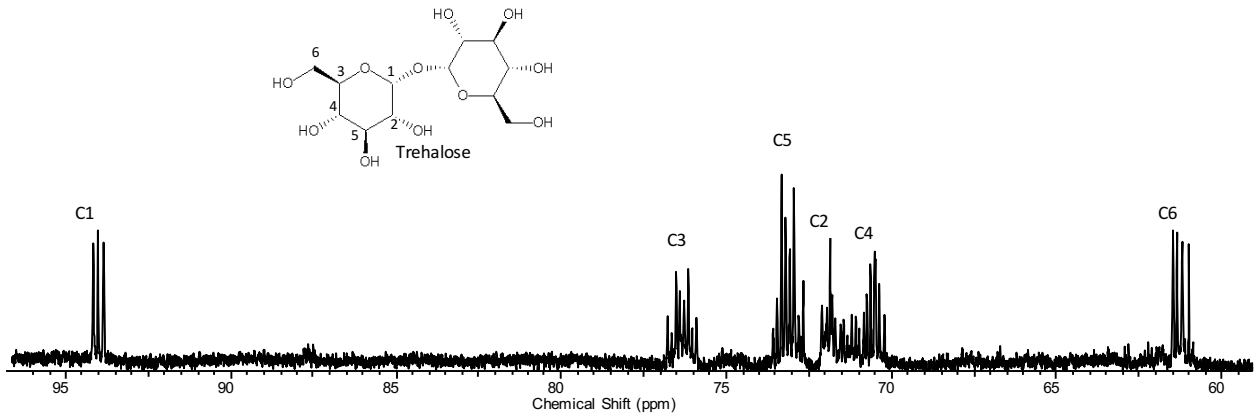

Figure 4.7 ^{13}C NMR spectrum of yeast cell PCA extraction after an aerobic incubation for 2hr with [U-^{13}C]acetate

As a control experiment, [U-^{13}C]acetate was cultured in yeast cell and checked its PCA extraction by ^{13}C NMR (Figure 4.7). TRE assigned C1~C6 peaks are shown at 94.4, 73.3, 73.7, 70.9, 72.2, and 61.7 ppm with ^{13}C-^{13}C splitting patterns which are caused by ^{13}C-^{13}C coupling between adjacent ^{13}C labeled carbon. This data implies that the TRE was synthesized from [U-

^{13}C] acetate by participating in the glyoxylate cycle partially since both glyoyxlate cycle and TCA cycle are involved in TRE synthesis from the acetate.[5] In a second experiment, [1-^{13}C]glyoxylate was incubated in yeast under the same conditions as in the [U-^{13}C]acetate experiment. The appearance of [3,4-$^{13}C_2$] labeled in TRE was expected when [1-^{13}C]glyoxylate is involved in gluconeogenesis. However, no ^{13}C labeled TRE was observed in the experiment (Figure 4.8). There was no significant difference of ^{13}C NMR spectra between incubating with [1-^{13}C]glyoxylate versus unlabeled acetate.

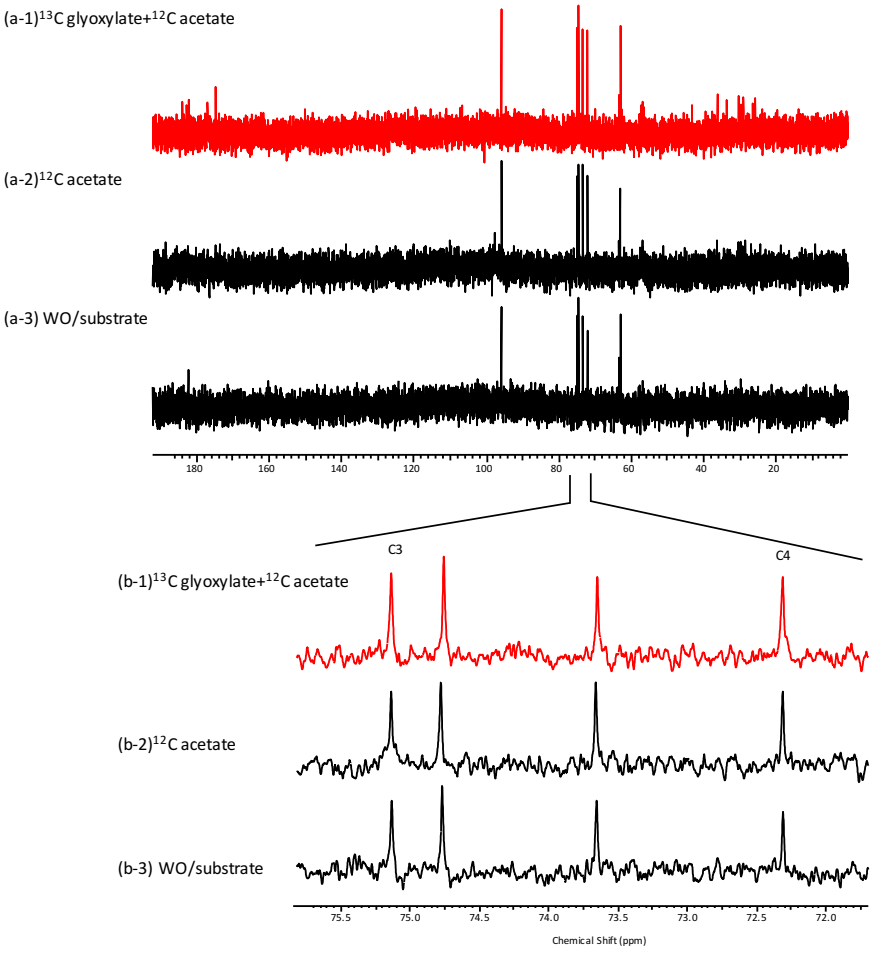

Figure 4.8 ^{13}C NMR spectra of yeast cell after incubation with [1-^{13}C]glyoxylate and the C1-C4 refer to the carbon atoms of TRE.

The flow of the ^{13}C label in this experiment is affected by not only the rate of the conversion of enzyme reaction involved in glyoxylate cycle but also by the rate of at which the substrates cross the cell membrane. Since one of the key enzymes of the glyoxylate cycle, malate synthase, is located in peroxisomes in the yeast, it would be required for exogenous glyoxylate to be translocated into cells and also into peroxisomes to be converted to malate. The mechanism of metabolite transport into peroxisomes is not clear but previous studies indicated that peroxisomes contain a transport channel.[62] Therefore, metabolite intermediates can cross the peroxisome by regulated transporter or diffusion based on size and charge of the intermediate.[2]

4.3.6 Hyperpolarization studies using [1-^{13}C]glyoxylate

[1-^{13}C]glyoxylate was hyperpolarized under standard conditions using a HyperSense DNP polarizer. After dissolution, the longitudinal relaxation time (T_1) was determined to be 15s at 9.4T by fitting hyperpolarized NMR signal (Figure 4.10). The T_1 decay of C1 glyoxylate is faster than expected for a single carboxylate carbon suggesting there may be dipolar coupling with the single proton on the C2 carbon. One could likely lengthen the T_1 of [1-^{13}C]glyoxylate by substituting a deuterium for the proton on C2 but this was not pursued.

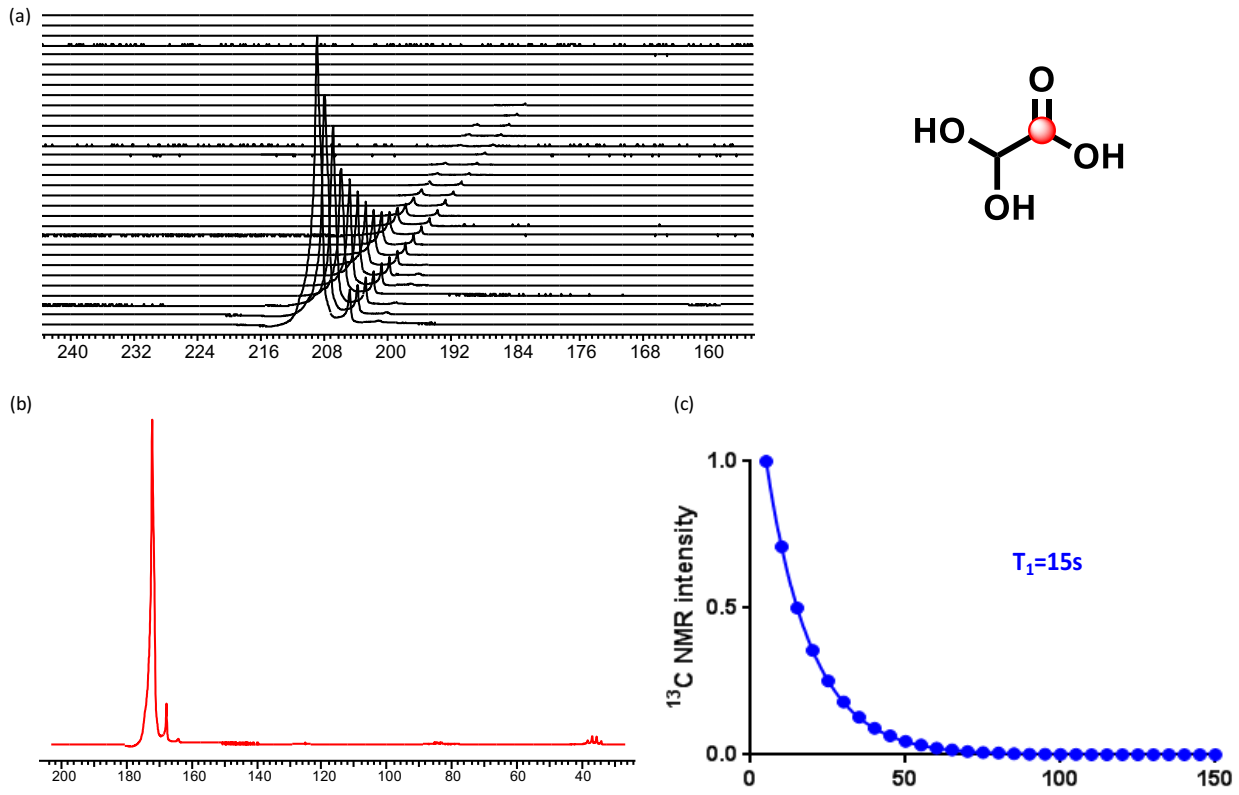

Figure 4.9 (a) Sequential ^{13}C NMR spectrum decay of [1-^{13}C]glyoxylate (b) the first ^{13}C spectra of hyperpolarized [1-^{13}C] glyoxylate (c) representative T_1 decay of hyperpolarized [1-^{13}C] glyoxylate after dissolution in PBS under 9.4T

4.4 Conclusions

The glyoxylate cycle converts a C2-carbon unit to C4-precursors to replenish the TCA cycle or to produce precursors of amino acid or carbohydrates for biosynthesis. It is known to exist in fungi and plants. In a recent studies, evidence for a glyoxylate cycle was reported in human and rat liver even though the absence of related enzymes make it unclear which metabolic pathways are involved. However, recently found CLYBL has been shown to have malate synthase activity. In addition, it is proposed that glyoxylate cycle in mammals may only be active under specific conditions such as in black bear brown fat during hibernation, starvation, or high fat diet. In this

study, to better understand the presence of glyoxylate cycle in mammals or, if present, to understand its physiological and pathological metabolic role, [1-^{13}C]glyoxylate was used to evaluate its potential as activity based hyperpolarized ^{13}C MR probe in the cells. Activity-based metabolite probe for detecting enzyme activity using dissolution DNP enables evaluating enzyme activity based on its functional properties rather than its abundance. Proper ^{13}C labeled metabolite probe is needed to use for activity-based metabolic detection of glyoxylate.

4.5 References

1. Kornberg, H.L. & Krebs, H.A. Synthesis of cell constituents from C2-units by a modified tricarboxylic acid cycle. *Nature* 179, 988-991 (1957).

2. Kunze, M., Pracharoenwattana, I., Smith, S.M. & Hartig, A. A central role for the peroxisomal membrane in glyoxylate cycle function. *Biochimica et Biophysica Acta (BBA) - Molecular Cell Research* 1763, 1441-1452 (2006).

3. Kornberg, H. Krebs and his trinity of cycles. *Nature reviews. Molecular cell biology* 1, 225-228 (2000).

4. Ajl, S.J. Conversion of a acetate and glyoxylate to malate. *Journal of the American Chemical Society* 78, 3230-3231 (1956).

5. Ikeda, T. & LaPorte, D.C. Isocitrate dehydrogenase kinase/phosphatase: aceK alleles that express kinase but not phosphatase activity. *Journal of Bacteriology* 173, 1801-1806 (1991).

6. Garnak, M. & Reeves, H. Phosphorylation of Isocitrate dehydrogenase of Escherichia coli. *Science* 203, 1111-1112 (1979).

7. Garnak, M. & Reeves, H.C. Purification and properties of phosphorylated isocitrate dehydrogenase of Escherichia coli. *The Journal of biological chemistry* 254, 7915-7920 (1979).

8. Ozaki, H. & Shiio, I. Regulation of the TCA and Glyoxylate Cycles in Brevibacterium flavum: I. Inhibition of lsocitrate Lyase and Isocitrate Dehydrogenase by Organic Acids Related to the TCA and Glyoxylate Cycles*. *The Journal of Biochemistry* 64, 355-363 (1968).

9. Dolan, S.K. & Welch, M. The Glyoxylate Shunt, 60 Years On. *Annual review of microbiology* 72, 309-330 (2018).

10. Kornberg, H.L. & Beevers, H. A mechanism of conversion of fat to carbohydrate in castor beans. *Nature* 180, 35-36 (1957).

11. Butterworth, P.J. Lehninger: principles of biochemistry (4th edn) D. L. Nelson and M. C. Cox, W. H. Freeman & Co., New York, 1119 pp (plus 17 pp glossary), ISBN 0-7167-4339-6 (2004). *Cell Biochemistry and Function* 23, 293-294 (2005).

12. Dunn, M.F., Ramirez-Trujillo, J.A. & Hernandez-Lucas, I. Major roles of isocitrate lyase and malate synthase in bacterial and fungal pathogenesis. *Microbiology (Reading, England)* 155, 3166-3175 (2009).

13. Barrett, J. *Biochemistry of parasitic helminths*, (University Park Press, Baltimore, 1981).

14. Lorenz, M.C. & Fink, G.R. The glyoxylate cycle is required for fungal virulence. *Nature* 412, 83-86 (2001).

15. Davis, W.L.*, et al.* The glyoxylate cycle in rat epiphyseal cartilage: the effect of vitamin-D3 on the activity of the enzymes isocitrate lyase and malate synthase. *Bone* 10, 201-206 (1989).

16. Davis, W.L., Matthews, J.L. & Goodman, D.B. Glyoxylate cycle in the rat liver: effect of vitamin D3 treatment. *FASEB journal : official publication of the Federation of American Societies for Experimental Biology* 3, 1651-1655 (1989).

17. Davis, W.L., Goodman, D.B., Crawford, L.A., Cooper, O.J. & Matthews, J.L. Hibernation activates glyoxylate cycle and gluconeogenesis in black bear brown adipose tissue. *Biochimica et biophysica acta* 1051, 276-278 (1990).

18. Popov, V.N., Igamberdiev, A.U., Schnarrenberger, C. & Volvenkin, S.V. Induction of glyoxylate cycle enzymes in rat liver upon food starvation. *FEBS Lett* 390, 258-260 (1996).

19. Popov, V.N., Volvenkin, S.V., Eprintsev, A.T. & Igamberdiev, A.U. Glyoxylate cycle enzymes are present in liver peroxisomes of alloxan-treated rats. *FEBS Lett* 440, 55-58 (1998).

20. Popov, V.N.*, et al.* Induction of a peroxisomal malate dehydrogenase isoform in liver of starved rats. *Biochemistry. Biokhimiia* 66, 496-501 (2001).

21. Kokavec, A. & Crowe, S.F. Alcohol consumption in the absence of adequate nutrition may lead to activation of the glyoxylate cycle in man. *Medical hypotheses* 58, 411-415 (2002).

22. Morgunov, I.G.*, et al.* Evidence of the glyoxylate cycle in the liver of newborn rats. *Medical science monitor : international medical journal of experimental and clinical research* 11, Br57-60 (2005).

23. Jones, C.T. Is there a gloxylate cycle in the liver of the fetal guinea pig? *Biochemical and Biophysical Research Communications* 95, 849-856 (1980).

24. Davis, W.L. & Goodman, D.B. Evidence for the glyoxylate cycle in human liver. *The Anatomical record* 234, 461-468 (1992).

25. Holmes, R.P. The absence of glyoxylate cycle enzymes in rodent and embryonic chick liver. *Biochimica et biophysica acta* 1158, 47-51 (1993).

26. Jones, J.D., Burnett, P. & Zollman, P. The glyoxylate cycle: does it function in the dormant or active bear? *Comparative biochemistry and physiology. Part B, Biochemistry & molecular biology* 124, 177-179 (1999).

27. Popov, V.N., Volvenkin, S.V., Eprintsev, A.T. & Igamberdiev, A.U. The Induction of Glyoxylate Cycle Enzymes in Tissues of Starving Rats. *Biology Bulletin of the Russian Academy of Sciences* 27, 565-570 (2000).

28. Davis, W.L.*, et al.* Identification of glyoxylate cycle enzymes in chick liver--the effect of vitamin D3: cytochemistry and biochemistry. *The Anatomical record* 227, 271-284 (1990).

29. Davis, W.L., Jones, R.G., Farmer, G.R., Matthews, J.L. & Goodman, D.B. Glyoxylate cycle in the epiphyseal growth plate: isocitrate lyase and malate synthase identified in mammalian cartilage. *The Anatomical record* 223, 357-362 (1989).

30. Strittmatter, L.*, et al.* CLYBL is a polymorphic human enzyme with malate synthase and beta-methylmalate synthase activity. *Human molecular genetics* 23, 2313-2323 (2014).

31. Salido, E., Pey, A.L., Rodriguez, R. & Lorenzo, V. Primary hyperoxalurias: Disorders of glyoxylate detoxification. *Biochimica et Biophysica Acta (BBA) - Molecular Basis of Disease* 1822, 1453-1464 (2012).

32. Williams, E.L.*, et al.* The enzyme 4-hydroxy-2-oxoglutarate aldolase is deficient in primary hyperoxaluria type 3. *Nephrology Dialysis Transplantation* 27, 3191-3195 (2012).

33. Dutta, U., Cohenford, M.A., Guha, M. & Dain, J.A. Non-enzymatic interactions of glyoxylate with lysine, arginine, and glucosamine: a study of advanced non-enzymatic glycation like compounds. *Bioorganic chemistry* 35, 11-24 (2007).

34. Nikiforova, V.J.*, et al.* Glyoxylate, a New Marker Metabolite of Type 2 Diabetes. *Journal of Diabetes Research* 2014, 9 (2014).

35. Dixon G.H., K.H.L. Assay methods for key enzymes of the glyoxylate cycle. *The Biochemical journal* 72(1959).

36. Hummel, J.P. The fluorometric determination of malic acid. *The Journal of biological chemistry* 180, 1225-1228 (1949).

37. Olson, J.A. Spectrophotometric measurement of alpha-keto acid semicarbazones. *Archives of biochemistry and biophysics* 85, 225-233 (1959).

38. Friedemann, T.E. & Haugen, G.E. PYRUVIC ACID: II. THE DETERMINATION OF KETO ACIDS IN BLOOD AND URINE. *Journal of Biological Chemistry* 147, 415-442 (1943).

39. Bonting, S.L. Colorimetric determination of pyruvic acid and other alpha-keto acids in submicrogram quantities. *Archives of biochemistry and biophysics* 58, 100-108 (1955).

40. Kramer, D.N., Klein, N. & Baselice, R.A. Quantitative Determination of Glyoxylic Acid. *Analytical Chemistry* 31, 250-252 (1959).

41. McFadden, B.A. & Howes, W.V. The determination of glyoxylic acid in biological systems. *Analytical Biochemistry* 1, 240-248 (1960).

42. Juni, E. & Heym, G.A. Determination of carbonyl acids formed upon periodate oxidation. I. Assay procedure. *Analytical Biochemistry* 4, 143-158 (1962).

43. Cohen, S.M., Ogawa, S. & Shulman, R.G. 13C NMR studies of gluconeogenesis in rat liver cells: utilization of labeled glycerol by cells from euthyroid and hyperthyroid rats. *Proceedings of the National Academy of Sciences of the United States of America* 76, 1603-1609 (1979).

44. Moffett, R.B. ETHYL DIETHOXYACETATE. *Organic Syntheses* 4, 427 (1955).

45. Rajagopalan, K.N.*, et al.* Metabolic plasticity maintains proliferation in pyruvate dehydrogenase deficient cells. *Cancer & metabolism* 3, 7-7 (2015).

46. Mullen, A.R.*, et al.* Oxidation of alpha-ketoglutarate is required for reductive carboxylation in cancer cells with mitochondrial defects. *Cell reports* 7, 1679-1690 (2014).

47. Cheng, T.*, et al.* Pyruvate carboxylase is required for glutamine-independent growth of tumor cells. *Proceedings of the National Academy of Sciences of the United States of America* 108, 8674-8679 (2011).

48. Malloy, C.R., Sherry, A.D. & Jeffrey, F.M.H. Carbon flux through citric acid cycle pathways in perfused heart by 13C NMR spectroscopy. *FEBS Letters* 212, 58-62 (1987).

49. Dickinson, J.R., Dawes, I.W., Boyd, A.S. & Baxter, R.L. 13C NMR studies of acetate metabolism during sporulation of Saccharomyces cerevisiae. *Proceedings of the National Academy of Sciences of the United States of America* 80, 5847-5851 (1983).

50. den Hollander, J.A., Behar, K.L. & Shulman, R.G. 13C NMR study of transamination during acetate utilization by Saccharomyces cerevisiae. *Proceedings of the National Academy of Sciences of the United States of America* 78, 2693-2697 (1981).

51. Benedict, S.R. A NOTE ON THE PREPARATION OF GLYOXYLIC ACID AS A REAGENT. *Journal of Biological Chemistry* 6, 51-52 (1909).

52. Weinhouse, S. & Friedmann, B. Metabolism of labeled 2-carbon acids in the intact rat. *The Journal of biological chemistry* 191, 707-717 (1951).

53. Rigby, W. Sodium Bismuthate as an Oxidizing Agent for Organic Compounds. *Nature* 164, 185 (1949).

54. n-Butyl Glyoxylate. in *Organic Syntheses* coll.vol.4, p214 (1963)

55. Vargha, L. & Reményi, M. 235. Selective oxidations with red lead. *Journal of the Chemical Society (Resumed)*, 1068-1069 (1951).

56. Krupka, R.M. & Towers, G.H.N. Small-Scale Preparation of Glyoxylic Acid labelled with Carbon-14. *Nature* 181, 335 (1958).

57. Scott, K. The role of temperature in oxalic acid electroreduction. *Electrochimica Acta* 37, 1381-1388 (1992).

58. Pickett, D.J. & Yap, K.S. A study of the production of glyoxylic acid by the electrochemical reduction of oxalic acid solutions. *Journal of Applied Electrochemistry* 4, 17-23 (1974).

59. Meany, J.E. & Pocker, Y. The dehydration of glyoxalate hydrate: general-acid, general-base, metal ion and enzymic catalysis. *Journal of the American Chemical Society* 113, 6155-6161 (1991).

60. Song, S. Can the glyoxylate pathway contribute to fat-induced hepatic insulin resistance? *Medical hypotheses* 54, 739-747 (2000).

61. Beeckmans, S., Khan, A.S., Van Driessche, E. & Kanarek, L. A specific association between the glyoxylic-acid-cycle enzymes isocitrate lyase and malate synthase. *European journal of biochemistry* 224, 197-201 (1994).

62. Douma, A.C.*, et al.* Permeability properties of peroxisomal membranes from yeasts. *Archives of Microbiology* 153, 490-495 (1990).

Chapter 5

General conclusions

Metabolic reprogramming occurs in cancer to accommodate the increased energy demand for sustained growth and proliferation. Although much of what we know about reprogramming of cancer cells has been derived from genetic and metabolomic analyses of tissue biopsies, the ultimate goal would be to perform *in vivo* real-time metabolic imaging of tumors to access tumor growth and response to treatment. In addition, *in vivo* imaging of changes in pH, redox state, reactive oxygen species, and biometal levels also can be a potential biomarker of metabolic changes. The development of efficient dissolution DNP of stable isotope-labeled substrates with commercially available hardware has opened up a new chapter for real-time noninvasive detection of several biochemical pathways by NMR *in vitro* and i*n vivo*. ^{13}C and ^{15}N DNP coupled with NMR spectroscopy provides an opportunity to non-invasively monitor metabolic flux or specific biological reactions from signals arising from the conversion of a ^{13}C or ^{15}N probe into a new product. The resolution of individual molecular species by high-resolution NMR spectroscopic readout allows the simultaneous detection of multiple sequential and parallel biochemical reactions. However, the decay of hyperpolarized signal due to T_1 relaxation and rf pulsing is a major limitation, which can partially be ameliorated by designing hyperpolarized probes with long T_1 values. Thus, there is a need for biocompatible and biorthogonal hyperpolarized probes that are rapidly incorporated into the biological pathway of interest within the lifetime of the hyperpolarized magnetization. In this dissertation, ^{13}C and ^{15}N DNP probes have been designed for imaging certain aspects of cancer metabolism.

The introductory chapter of this dissertation gives an overview of DNP applications and limitations. In particular, the basic principles of NMR, the use of ^{13}C tracers *in vivo*, the DNP mechanisms, and biological applications of d-DNP are described.

In the first project, ^{15}N-labeled tripodal ligands were developed as hyperpolarized ^{15}N NMR sensors of zinc ions to monitor alterations in Zn^{2+} levels, a unique biomarker of prostate malignancy. Specially, a cell permeable ^{15}N-labeled, deuterated tripodal ligand, tris(pyridylmethyl)amine-d_6 (^{15}N-TPA-d_6) was designed and synthesized as a hyperpolarized ^{15}N MR sensor for Zn^{2+} with the aim of detecting free Zn^{2+} in both intracellular and extracellular spaces. ^{15}N-TPA-d_6 was synthesized starting from $^{15}NH_4Cl$ and 1-(chloromethyl-d_2) pyridine using standard organic reactions and was hyperpolarized by microwave driven dynamic nuclear polarization (DNP). The ^{15}N longitudinal relaxation time (T_1) of ^{15}N-TPA-d_6 was found to be 89s at 3T. Chelation experiments with hyperpolarized ^{15}N-TPA-d_6 and Zn^{2+} ions revealed that the ^{15}N NMR signal of ^{15}N-TPA-d_6 shifted 20 ppm upfield upon complexation. The ^{15}N spectra also indicated that Zn^{2+} exchange between free ligand and TPA-d_6-Zn^{2+} complex is slow on the experimental NMR timescale. The Zn^{2+} detection limit of hyperpolarized ^{15}N-TPA-d_6 was found to be around 5 μM Zn^{2+}. Ligand protonation and Ca^{2+} binding did not interfere with the Zn^{2+} sensing. ^{15}N chemical shift images of phantoms containing HP ^{15}N-TPA-d_6 in the absence and presence of Zn^{2+} were collected to demonstrate the feasibility of *in vivo* imaging of Zn-distribution. These data show that ^{15}N-TPA-d_6 is a promising hyperpolarized Zn^{2+} sensor. However, albumin binding of the hyperpolarized ligand resulted in rapid loss of ^{15}N polarization within seconds. To address this problem, it was attempted to eliminate the binding by competitive inhibition with iophenoxic acid (IPA) as a displacer. Competitive displacement

experiments with IPA and HP-^{15}N-TPA-d_6 in the presence of albumin revealed that IPA nearly completely restored the hyperpolarized ^{15}N TPA signal in the presence of HSA. The development of hyperpolarized Zn^{2+} probes will enable the measurement of total cellular free Zn^{2+} which could be useful in early diagnosis of prostate malignancies.

The focus of the second project was the development of hyperpolarized [1-^{13}C] α-ketoisocaproate (KIC) as a HP-^{13}C imaging agent to measure altered branched-chain amino acid oxidation. HP [1-^{13}C] KIC was proposed as a metabolic probe for detecting and comparing branched-chain aminotransferase (BCAT) and alpha-keto acid dehydrogenase (BCKDH) activity in normal healthy brain *versus* F98 glioma. Injected hyperpolarized [1-^{13}C]KIC was found to be metabolized to its transamination product [1-^{13}C]leucine by BCATs or catabolized to $^{13}CO_2$/bicarbonate ($H^{13}CO_3^-$) by BCKDH. ^{13}C MR imaging results of hyperpolarized ^{13}C-leucine by BCAT was smaller in glioma as compared to the contralateral normal-appearing brain, NAB. It is possibly due to the predominant net conversion of leucine to KIC and associated depletion of leucine pool. On the other hand, more bicarbonate, a decarboxylation product of [1-^{13}C] KIC, was observed in glioma than normal brain, presumably due to higher activity of BCKDH in glioma, suggesting that BCKA catabolism by BCKDH in tumor was stimulated. This *in vivo* imaging study using hyperpolarized [1-^{13}C]α-ketoisocaproate in a rat glioma model (F98) suggested upregulated oxidation of BCAAs in glioma. To elucidate BCAA oxidation at steady state, *ex vivo* ^{13}C NMR isotopomer analysis following steady-state infusion of [U-^{13}C]leucine to glioma-bearing rats verified the increased oxidation of leucine in glioma tissue. Both the hyperpolarized ^{13}C-KIC imaging study and the ^{13}C-leucine infusion study demonstrated increased catabolism of BCKA in tumor compared to the contralateral NAB. To the best of my

knowledge, this is the first report of hyperpolarized [1-^{13}C] KIC *in vivo* imaging in rat glioma model. This finding provides strong evidence of diagnostic potential of altered BCAA metabolism in glioma.

In the third project, a ^{13}C metabolic probe was designed and tested to establish whether the glyoxylate cycle is active in mammalian cells. Even though glyoxylate cycle is thought to be absent in mammalian metabolism due lack of existence of the necessary enzymes, a few papers have found the glyoxylate cycle enzymes present in mammals tissues. In addition, it has been suggested that human metabolic diseases associated a high glucose demand, such as glycolytic cancer, may activate the glyoxylic cycle to compensate for these needs. [1-^{13}C] glyoxylate hydrate was synthesized and evaluated as a potential probe for malate synthase activity by the appearance of [1-^{13}C]malate. Although no evidence for glyoxyate cycle activity was evident in mouse embryonic fibroblasts, the study provided new insights into the possible reasons why intermediates such as glyoxyate may not enter into active metabolic pathways.

In summary, non-endogenous and endogenous ^{15}N and ^{13}C hyperpolarized NMR probes have been developed for detecting Zn^{2+}, imaging of glioma metabolism, and attempting to detect glyoxylate shunt pathways in tissues. These studies demonstrate that hyperpolarized ^{15}N and ^{13}C labeled NMR probes can be used for noninvasive monitoring of metabolic processes and physiochemical detection. The information provided by the chemical shifts enables the identification and real time quantification of downstream metabolites, thereby facilitating the determination of flux via specific enzyme catalyzed steps.

VITAE

Eul Hyun Suh (September 28th 1975-present) was born in Seoul to Yong Hee Suh and Okki Min. She grew up as a Christian in Seoul, and began to explore her interest in Chemistry from homeopathic medicines of natural products. She attained a Bachelor of Science degree in Chemistry at Seoul Women's University in 1998. Then, she continued her studies in the total synthesis of natural compounds, and earned a Master of Science degree in Organic Chemistry under the guidance of Dr. Mankil Jung at Yonsei University in 2001. Eul Hyun worked at the industrial research center (2001-2005) of Dowoo Fine Chem Co.Ltd at Korea and SUMITOMO chemical Co.Ltd at Japan. After she married her soulmate, Jiyong Lee, an alumnus of UT Southwestern Medical Center, they have beautiful daughter, Chloe Lee. Eul Hyun returned to academic research and worked at the Advanced Imaging Research Center of the UT Southwestern Medical Center under the supervision of Dr. Zoltan Kovacs as a research assistance (2006-2009). Then, she moved to the Scripps Research Institute and worked on synthetic chemistry projects at Dr. Jeffery W Kelly's lab (2010-2012). Applying her background in Chemistry and Biochemistry to metabolic study using DNP, she earned a Ph.D. degree in Biomedical Engineering under the guidance of Dr. A. Dean Sherry from the UT Southwestern Medical Center on February 28, 2019